Biomarker Assay Development and Sensing with Solid-State Nanopores

Eric Beamish

A thesis submitted in partial fulfillment of the requirements for the

Doctorate in Philosophy in Physics

Ottawa-Carleton Institute for Physics

Department of Physics
Faculty of Science
University of Ottawa

Contents

Abstract

Broadly speaking, the work herein discussed encompasses the development of biomolecular assays for biomarker detection. Specific to the assays in this thesis is the design of reaction schemes that consider the unique requirements of one class of single-molecule sensors in particular: solid-state nanopores formed using a novel fabrication and conditioning technique discovered during this research at the University of Ottawa.

We present three unique assays for the detection of different biomolecular targets. The first uses a class of DNA origami structures termed nanoswitches to translate the presence of a short segment of single-stranded DNA Zika virus biomarker to a large configurational change in a double-stranded DNA scaffold. The signal amplification inherent in this topological change allowed us to a achieve a high degree of specificity for detecting a small nucleic acid target by requiring two separate binding events. Furthermore, through careful design of the configurational change, the number of topological states that a solid-state nanopore can sense is limited, providing unambiguous signals in ionic current recordings. Quantification of the Zika gene was performed by sensing the relative amounts of nanoswitches in looped and linear configurations from only hundreds of individual molecules.

We then explored the sensitivity of solid-state nanopores for detecting small molecular features along short DNA scaffolds. Leveraging the ability of our nanopores to detect the presence of these protrusions, we present results in which ATP, a molecule significantly too small to be directly detected by the nanopore sensor, initiated an

aptamer-based DNA displacement reaction to form a protrusion along scaffolds, producing measurable changes in ionic current signatures in nanopore recordings.

Finally, we present an assay in which a microRNA, a biomarker linked to various cancers, was detected through the conjugation of two probes, each of which contained a binding site to different segments of the microRNA. In addition to examining different probe set structures for optimal performance, our two-probe design aimed to improve specificity over conventional single-probe-based assays which only require one recognition step, while still providing unambiguous signals due to the greater-than-doubling in molecular complex size upon conjugation. Furthermore, the use of two individual small probes, rather than one large nanoswitch, increased the resolution with which we could differentiate microRNA concentrations. The assay enabled the quantification of six concentrations of microRNA spanning a single order of magnitude, in only several hundred events, and allowed us to take advantage of the reduced cost, material and labour, as well as increased nanopore capture rates, associated with small assembled molecules.

Acknowledgements

While theses are undoubtedly collaborative works from start to finish, I feel like this particular instance merits special mention of the supervisorial contributions of Dr. Michel Godin. While his silver tongue earned him a relatively free student for the first several years of the work presented, I don't think he was counting on how much this particular student would cost him once grants ran out in Grades 26 through 28. While financial contributions were always committed with a genuine smile, I think that having to sit through weekly meetings with a Bruins fan for nine years is something that no one really signs up for when they accept a Professorship. That could not have been easy to get through in such an easy-going manner. Maybe it's something in the Bearbrook water, but I think that having an employee that continues to look up to you in all things work-, apparent personal values-, and professionalism-related is the most telling sign of the calibre of a supervisor that I can offer.

On a similar note, the contributions of Dr. Vincent Tabard-Cossa to this thesis are immeasurable. While by rights I could be *his* supervisor based on employment starting date, his dedication to his students is perhaps the most admirable quality that I've encountered in my time at the University of Ottawa, and his passion for science is second to none. He has also made my bucket list in that I *will* one day see DJ-VTC bring the House down.

I also owe thanks to Dr. Carlos Campana. While he may no longer remember who I am, I would be remiss in not acknowledging the fact that any professional success that I have ever achieved can be in part traced directly back to him. An all-around great human

being, it is my honour to mention him in this instance as someone that I look up to both professionally and personally who, maybe without even knowing it, has made such a positive impact in my life through his selfless contributions to our work together.

While my colleagues have all provided invaluable contributions to this work, among the most significant along this particular journey were those of: Ainara and Jon, who provided a home-away-from-home and made me realise that some people are just too humble to recognise the common factor when professional and personal success seems to come to you no matter where you go on the globe or what language you're trying to speak; Kyle, who has your back no matter what (and quite frankly is too good at his job, contributing far too much to this thesis); Waugh, who alongside making many of the pores used in this thesis, gives me ample opportunity to practice gracious losing, albeit unsuccessfully; and Radin, for reinventing the meaning of the words loyalty and friendship – no *taarof*.

No success I could ever achieve would be possible without the incomparable role models and personal motivators of Kayla, Scott, Granny, Stan and Carolyn. And Stephanie, who deserves much more credit and appreciation than this section could ever acknowledge. This thesis is dedicated to you guys.

Statement of Originality

The material herein presented is a direct result of my work as a Ph.D. student, containing adaptations of articles that have been either published by or submitted to peer-reviewed journals at the time of submission. In several places, cosmetic changes have been made to these works for the sake of consistency within this document.

While Chapter 1 contains instances of work published as parts of my Master's thesis at the University of Ottawa, it also contains extensions of that work which took place over the initial phase of my Doctoral research that were subsequently published as either a follow-up paper or patent. Chapters 2 and 3 are articles that have been peer-reviewed and published in *ACS Sensors*, and Chapter 4 is a version of an article submitted to *Nature Communications* at the time of submission of this thesis.

Chapters 2-4 consist of original work in which I performed all stages of experimental design and execution, data analysis, writing and article submission. In addition to the individual contributions mentioned in the Acknowledgement Sections of each Chapter, experiment conception and manuscript draft editing were aided by co-authors Drs. Godin and Tabard-Cossa. Chapter 5 contains elements of papers in which I was a co-first author or co-author, as indicated in the Statement of Contributions. In these instances, I contributed in varying degrees to experimental design, data analysis and writing of published or submitted peer-review articles and patents, with all experiments being executed by Dr. Radin Tahvildari or Dr. Ali Najafi Sohi, who also performed most tasks required to bring these bodies of work to fruition.

Statement of Contributions

Publications (Ph.D.)

1. **E. Beamish**, V. Tabard-Cossa, M. Godin. Digital counting of microRNA using solid-state nanopores. *Submitted: Nature Communications (2019).*
2. **E. Beamish**, V. Tabard-Cossa, M. Godin. Programmable DNA Nanoswitch Sensing with Solid-State Nanopores. *ACS Sensors,* 4 (**9**), pp. 2458-2464 (2019).
3. A.N. Sohi, **E. Beamish**, V. Tabard-Cossa, M. Godin. Effect of Flow on DNA Capture and Translocation through Nanopores – *Submitted: Small (2019).*
4. **E. Beamish**, V. Tabard-Cossa, M. Godin. Identifying Structure in Short DNA Scaffolds using Solid-State Nanopores. *ACS Sensors*, 2 (**12**), pp 1814–1820 (2017).
5. R. Tahvildari, **E. Beamish,** *et al.* Manipulating Electrical and Fluidic Access in Integrated Nanopore-Microfluidic Arrays Using Microvalves. *Small*, DOI: 10.1002/smll.201602601 (2016).
6. R. Tahvildari,*** E. Beamish,*** V. Tabard-Cossa, M. Godin. Integrating Nanopore Sensors within Microfluidic Channel Arrays. *Lab on a Chip* **15**, 1407-1411 (2015).
7. **E. Beamish**, W.H. Kwok, V. Tabard-Cossa, M. Godin. Fine-Tuning the Size and Minimizing the Noise of Solid-State Nanopores. *Journal of Visualized Experiments* **80**, e51081 (2013).

Publications (M.Sc.)

8. **E. Beamish**, W.H. Kwok, V. Tabard-Cossa, M. Godin. Precise Control of the Size and Noise of Solid-State Nanopores using High Electric Fields. *Nanotechnology* **23**, 405301 (2012).

Patents

9. R. Tahvildari,* **E. Beamish**,* V. Tabard-Cossa, M. Godin. Nanopore Fabrication within Microfluidic Channels. *PCT/IB2015/059799* (2015)
10. **E. Beamish**, W.H. Kwok, V. Tabard-Cossa, M. Godin. Method for Controlling the Size of Solid-State Nanopores. *PCT/IB2013/000884* (2013)

Conference Presentations

11. **E. Beamish**. *Talk*: "Identifying Structure in Molecular Complexes using Solid-State Nanopores." *Ottawa Carleton Institute of Physics Seminar* (Spring 2018).
12. **E. Beamish**, V. Tabard-Cossa, M. Godin. *Talk*: "Identifying Structure in Short DNA Scaffolds using Solid-State Nanopores." *WE-Hereaus Seminar, Bremen, Germany* (2017).
13. **E. Beamish**, V. Tabard-Cossa, M. Godin. *Poster*: "Identifying Structure in Short DNA Scaffolds using Solid-State Nanopores." *Biophysical Society of Canada Annual Conference, Montreal, Canada* (2017).

* These authors contributed equally to this work.

List of Figures

List of Tables

Chapter I.

Introduction

1.0 Foreword

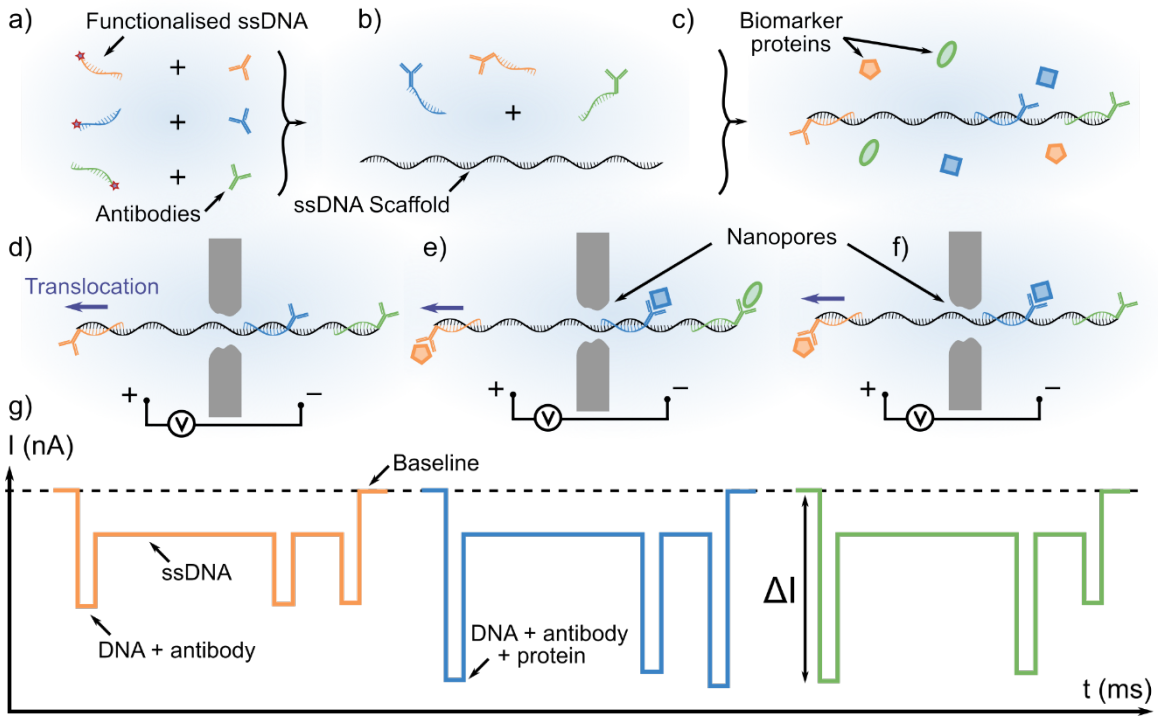

Figure 1.0 Schematic representation of multiplexed biomarker detection using nanopores.

a)-g) Incomprehensible images detailing what not to do to earn a PhD in Physics. Further detail on this Plan can be found in Section 1.3.

If the word thesis is defined as a statement that is put forward as a premise to be proven, I think there are few images that would better encapsulate the antithesis my graduate research than Figure 1.0. To no one's surprise, experimentation has demonstrated that Figure 1.0 fails Dr. Rutherford's test of comprehensibility to my

barperson (barpeople, actually), and Dr. Feynman would assure you that there is absolutely no risk of my nephew understanding it when he turns six years old. On the other hand, it pains me that I can't find the original version of this schematic which, believe it or not, was first hand-drawn for me by my one-time Electricity and Magnetism professor in his office on the corner of a piece of scrap paper as he tried to recruit a potential graduate student.

While Figure 1.0 is understandably ununderstandable at this point, the gist of the image is an assay in which, in reverse order, a purely electronic sensor (a nanopore) produces a readout to detect biomarkers such as proteins that are indicative of disease. Preassembled structures comprised of unique binding sites along a single-stranded DNA "scaffold" would allow for unique, differentiable current signatures depending on which disease biomarker(s) were present in a patient sample. I found it hard to imagine a research project more interdisciplinary, but what really inspired me was the cleverness of the scheme to detect a panel of disease biomarkers, and thus perform diagnoses, using a hand-held device, in a bedside manner, by measuring the properties of a single molecule.

Before we get our hopes up, I want to emphasise that while Figure 1.0 details to the *Plan* behind what we set out to achieve all the way back in 2010, the Escheresque path that we actually took resulted in substantially different outcomes. Nanopore-based sensing was always going to be in the picture, but it turns out that multiplexed protein detection with this platform is really, *really* challenging. And yet somehow, despite the many different avenues explored as the Plan evolved and we learned just how

complicated each element would be, that original hand-drawn image has many themes that recurred throughout our work over the past near-decade.

So, while Figure 1.0 will probably not be the final figure shown in this thesis, the aim of the following chapters is to unpack it, more or less, one piece at a time. The goal here is that a better understanding of why so many parts of that initial drawing were perhaps a little bit ambitious might also provide a better understanding of the fruit ultimately borne from it, and why we chose to tackle the problems that we did. While this is not to be a historical recount of our adventures in the world of nanopores, it is my hope to give an appreciation of how our work progressed along with an emerging field as we developed an understanding of just what sorts of experiments were possible, as the Plan became plans of action, and naïveté slowly ceded ground to wisdom.

1.1 Nanopore Sensing and Fabrication

Not unlike the origins of the Plan in Figure 1.0, the field of nanopore sensing was arguably born of a red pen and some notebook pages back in 1989.[1] The real workhorse behind all of the work presented in this thesis, these sensors were originally conceived as DNA sequencers. Following the Coulter principle, the idea was that if a single nanoscale aperture was the only conduit for electrical current between two electrolyte reservoirs under an applied potential bias, one of which contained DNA molecules, then ionic current measured through this nanopore would be disrupted as DNA was electrophoretically driven through due to its negative charge. This process is termed *translocation*. This concept is schematically illustrated in Figure 1.1a-b, where transient blockades are produced in the baseline ionic current measured as polymers translocate

through the nanopore.[2] This principle applies to just about all nanopore-based sensing: (bio)molecules such as nucleic acids (single- or double-stranded DNA or RNA), amino acids such as proteins or anti-bodies, or even small molecules, cause a blockage in ionic current during translocation, the depth of which is proportional to the volume occupied in the nanopore sensing region (often approximated as the cross-sectional area for longer polymers), and the duration of which can be used to infer biomolecular length. It was thought that this principle could be applied to determining the sequence of a single-stranded (ss) DNA segment, as shown in the original sketch of the sequencing concept in Figure 1.1c.[1] The idea was that as each base (A, G, C, T) would block an amount of ionic current proportional to its size, in order, during translocation. The characteristic signatures could then be used to infer the sequence.

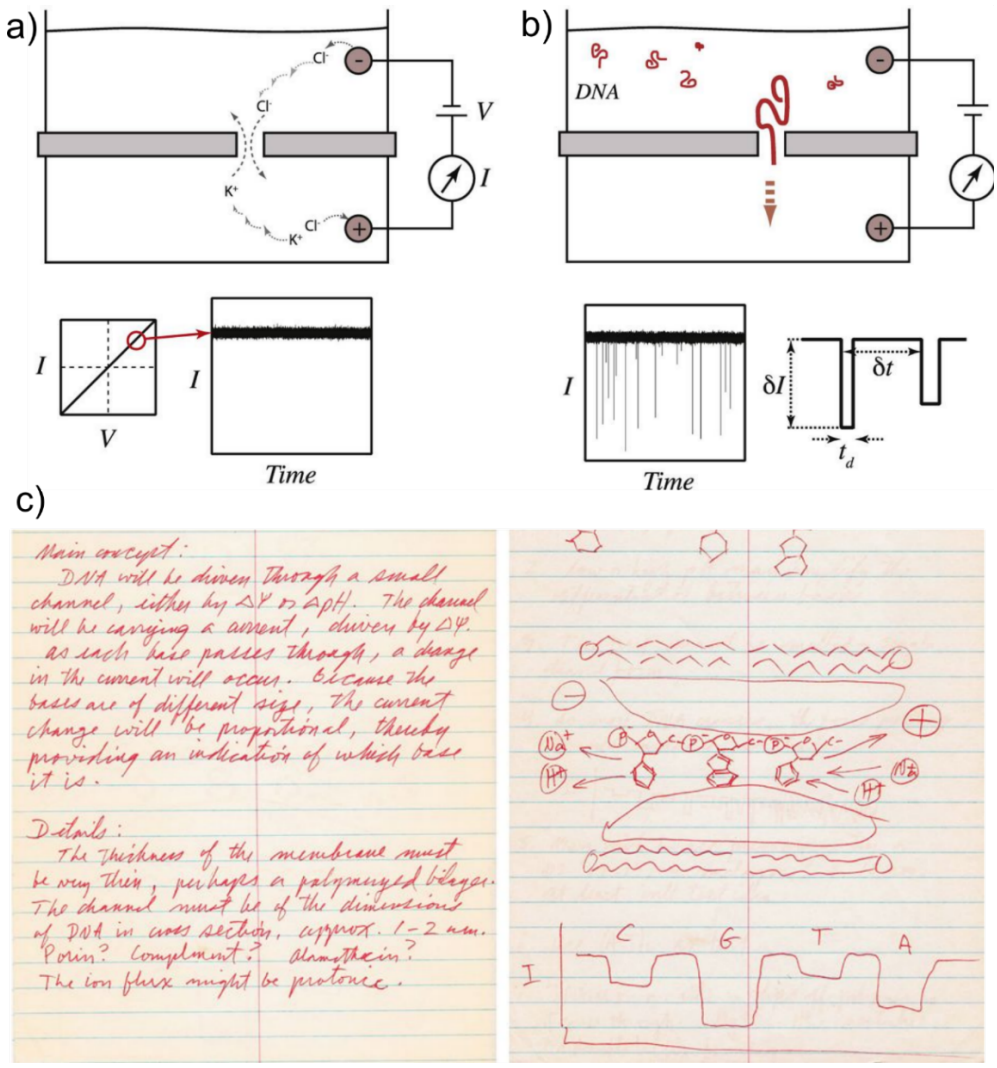

Figure 1.1 Conceptual drawings of nanopore sensing and DNA sequencing.

a) Ionic current is measured through a very thin constriction (a nanopore) whose diameter is comparable to that of the analyte under an applied voltage bias. b) As negatively charged polymers such as DNA are electrophoretically driven through, ionic current is reduced by an amount proportional to the size of the molecular segment in the nanopore. c) An early conceptual drawing depicting the use of nanopores for sequencing, whereby nucleic acid bases produce distinct blockage states based on their different sizes, which are identified, in order, to determine the sequence. Images adapted from references 2 (a-b) and 1 (c).

1.1.1 Biological nanopores

Early successful nanopore experiments used biologically inspired protein pores embedded in lipid bilayers.[3–7] Ubiquitous in cell membranes, these protein channels have naturally evolved for a wide range of purposes, from maintaining ion gradients to actively transporting nucleic acids during mitosis.[8] While it took decades of fine-tuning the properties of these repurposed biological nanopores, ultimately through their engineering with conjugated enzymes to ratchet DNA slowly enough to resolve sufficiently short segments for base identification,[9] long-read genome sequencing was finally achieved, perhaps most impressively on board the International Space Station in 2016.[10]

Figure 1.2 summarises several of the more common biological nanopores,[11] with α-hemolysin being among the first to be experimentally tested for single-molecule DNA sensing.[4] While biological nanopores have numerous desirable properties, including very low capacitance for low-noise electrical measurements and therefore excellent sensitivity, they have the drawback of being relatively fixed in size which limits the types of molecules that they can probe. Since the narrowest pore constriction roughly dictates the maximum size of a molecule that can translocate, only small molecules such as ssDNA can be studied in their native state, while bulkier molecules such as proteins and dsDNA must be denatured or unzipped to translocate. Additionally, as biological nanopores are embedded in lipid membranes, they can only be used under a limited range of experimental conditions due to their fragility and are not well suited to mass manufacturing as their assembly is not easily scalable.

Biological Nanopore	Structure		Critical Dimension	Types of Analytes
	Side View	Top View		
α-HL		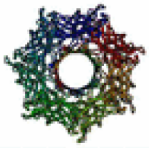	1.4 nm[108]	small molecules, RNA, ssDNA, dsDNA, proteins
OmpG			1.3 nm[118]	small molecules, proteins
MspA			1.2 nm[110]	ssDNA, dsDNA

Figure 1.2 Summary of common biological nanopores used in single-molecule sensing experiments.

Side and top views of three of the more common biological nanopores used in single-molecule studies. The narrowest constriction (critical dimension) of each nanopore dictates the types of analytes that can be probed. Small molecules and ssDNA are the only species that can translocate such narrow constrictions in their native states. Image adapted from reference 10.

1.1.2 Ion beam-drilled nanopores in solid-state membranes

Perhaps in an attempt to address some of the issues inherent in the biological variety, a synthetic approach to nanopore fabrication was developed in the early 2000s.[12] Initial embodiments of these inorganic pores replaced the fragile lipid bilayer of their predecessors with solid-state membranes, typically made of amorphous silicon nitride (SiN_x) that were less sensitive to environmental conditions. Figure 1.3 shows a schematic representation of the concept and apparatus used to fabricate some of the earliest solid-state nanopores. In this case, collimated beams of Ar^+ were used to ablate one side of

SiN_x membrane that were previously etched with cavities on the opposite side, ultimately exposing nanometer-sized apertures.

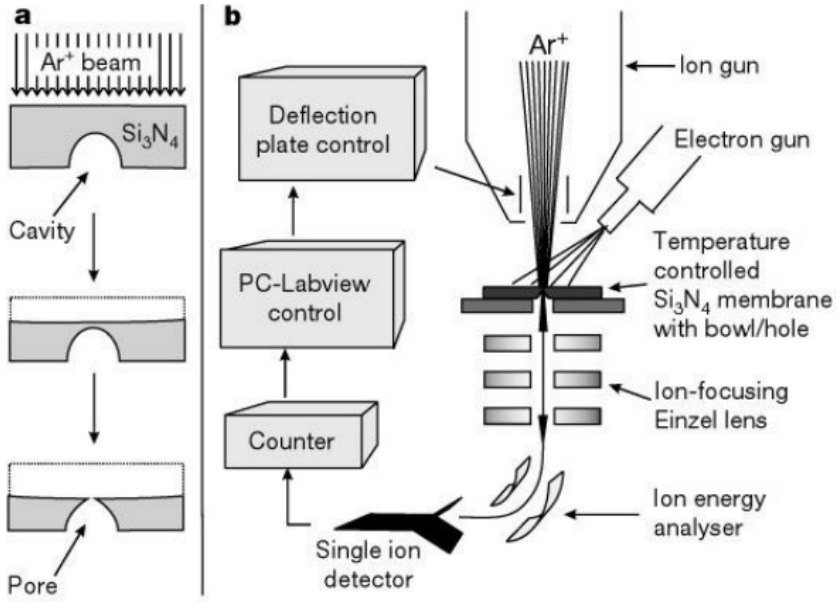

Figure 1.3 Schematic representation of nanopore fabrication using ion beam lithography.

a) A SiN_x membrane with a previously etched cavity is exposed to a collimated beam of Ar^+ ions. Membrane removal opposite the cavity results in a nanoscale opening (nanopore) at the cavity tip. b) A schematic representation of the fabrication setup. Image adapted from reference 11.

While the nanopores fabricated as shown in Figure 1.3 required relatively complex membrane preparation, it was quickly understood that a very similar approach could be used to fabricate nanopores directly using transmission electron microscopes (TEMs).[13] By tightly focusing a beam of electrons to an area nanometers in diameter, nanopores can be formed via sputtering of the SiN_x membrane and subsequently sculpting nanopores to the desired size. While membranes used in these early nanopore experiments were developed using combinations of wet and dry etching, this approach to nanopore formation has the advantage of commercially available membranes, as a variety

of suitably thin solid-state materials are manufactured as TEM sample holders. Unlike biological nanopores that have fixed diameters, the ability to sculpt solid-state materials with focused ion beams allows for the fabrication of nanopores with a much wider range of sizes, as shown in Figure 1.4 of some of the first nanopores ever fabricated at the University of Ottawa.[14]

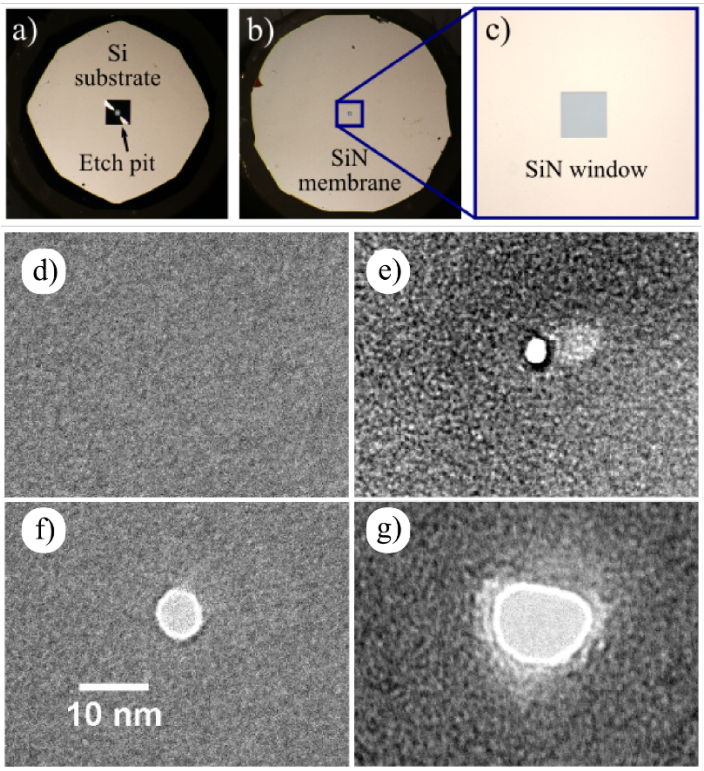

Figure 1.4 Nanopores drilled using a TEM.

(a-c) Various optical magnifications of commercially available TEM sample holders containing 30 nm thick SiN_x membrane windows (50 µm by 50 µm). TEM images show the membrane before (d) and after drilling nanopores of various sizes (e-g). Image adapted from reference 13.

The effects of using larger nanopores are immediately seen in Figure 1.5, where one of the earliest reported single-biomolecule experiments with solid-state nanopores show the translocation of dsDNA molecules through pores 10 nm in diameter.[13] While

translocation experiments with biological nanopores typically exhibit a single blockage state due to the limited number of configurations that molecules can assume during transit through very narrow constrictions, larger solid-state nanopores can allow the passage of molecules in various topological states. For instance, dsDNA has a persistent length of ~ 50 nm (~150 bp) and hydrodynamic diameter of ~2.2 nm. As such, long dsDNA molecules can enter pores 10 nm in diameter in either linear or folded states. This is shown in Figure 1.5a as density plots of the mean blockage depth ΔI versus event duration, typically referred to as translocation time τ, where two populations of single-level events are observed for the translocation of 10 kbp dsDNA. The first corresponds to the single-file translocation of polymers with relatively shallow depth and long duration. Folded molecules, on the other hand, exhibit twice the blockage depth and half of the total translocation time due the increase in occupied nanopore area of two dsDNA segments occupying the nanopore sensing volume and the corresponding reduction in effective length, respectively. Multi-level events in Figure 1.5b show that further resolution of molecular topology is also possible, as partially folded molecules exhibit both blockage states within a single event, given sufficient temporal resolution.

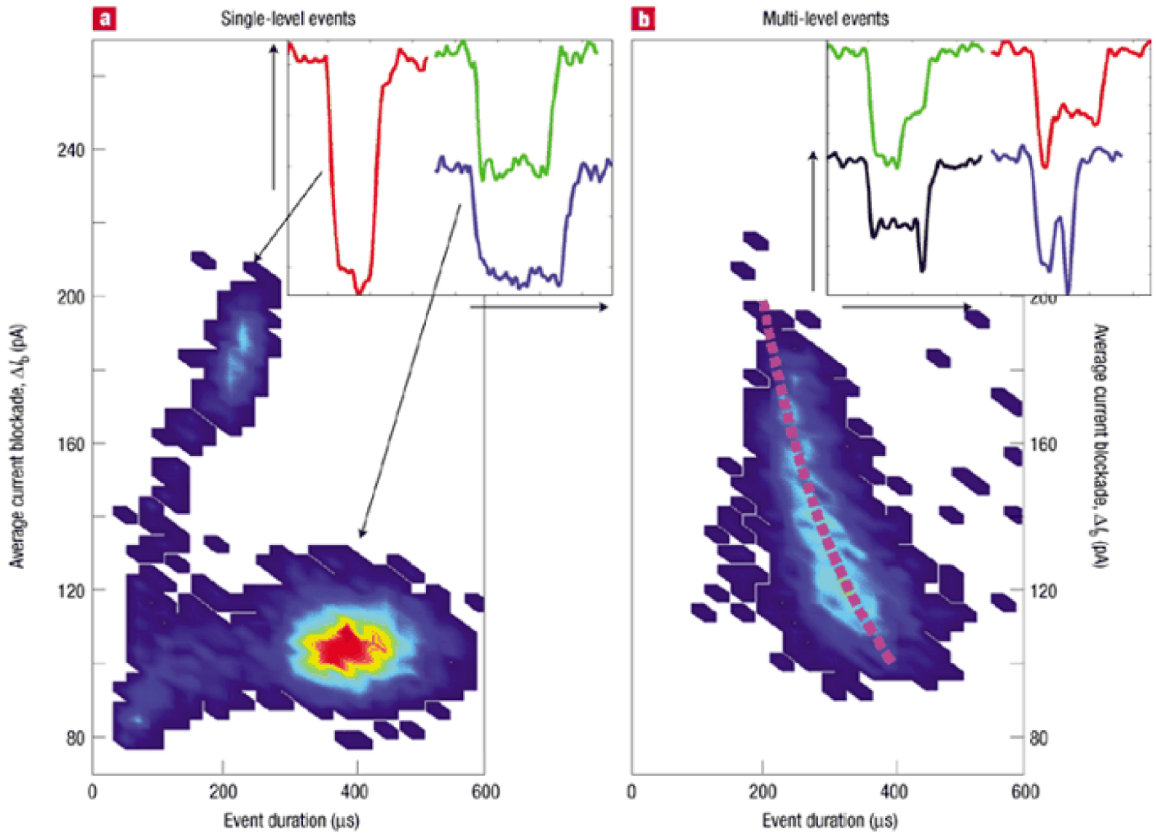

Figure 1.5 Translocation of dsDNA through a TEM-drilled solid-state nanopore.

Ionic current traces of 10 kbp dsDNA molecules through a nanopore 10 nm in diameter formed in a SiN_x membrane show a variety of translocation signatures. a) Single-level blockades show two clusters in density plots of the average blockage depth versus the event duration corresponding to linear and folded molecules. b) Depending on the conformation of the molecules when they are captured by the nanopore, a variety of current signatures can be observed as multi-level events. Image adapted from reference 12.

1.1.3 Glass nanopipettes

Somewhat unique among nanopore sensing platforms, nanopipettes lack a conventional membrane and are instead formed by standard pipette pulling techniques to form a nanoscale aperture, typically in glass or quartz. Often conical in geometry and shown in Figure 1.6, these pores behave somewhat differently from membrane-based systems in that they can be electrically rectifying and have longer sensing regions.[15,16]

While this reduces spatial resolution, the dielectric properties of glass provide very low capacitance and reduced high frequency noise as compared to nanopores formed in thin membranes.[17] Pipette size can be somewhat controlled with careful choice of pulling parameters during fabrication, or even reduced using electron beam irradiation,[18] but diameters are typically restricted to >10 nm.

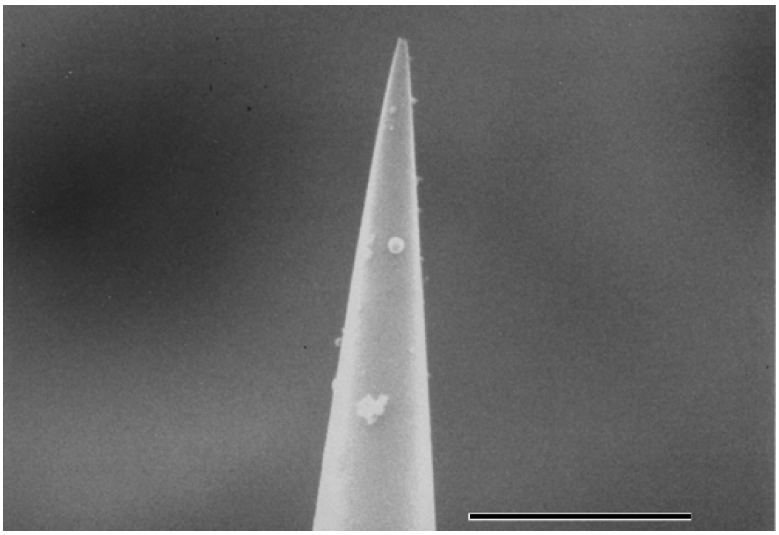

Figure 1.6 Glass nanopipette formed by laser pulling.

A scanning electron micrograph showing the conical tip of a glass nanopipette with a 2 μm scale bar. Image adapted from reference 14.

The relative ease of fabrication using commercially available pipette pullers allows for the generation of many nanopores in a very short amount of time, and even for the manufacture of devices containing tens of individual nanopores to ensure successful sensing experiments, as shown in Figure 1.7. The glass substrate is also amenable to functionalisation with materials such as gold[19] or antibodies,[20] with some systems even including smaller nanopores comprised of biological pores embedded in lipid bilayers[21]

or synthetic pores formed from DNA as a structural material at the tip of the nanopipette.[22]

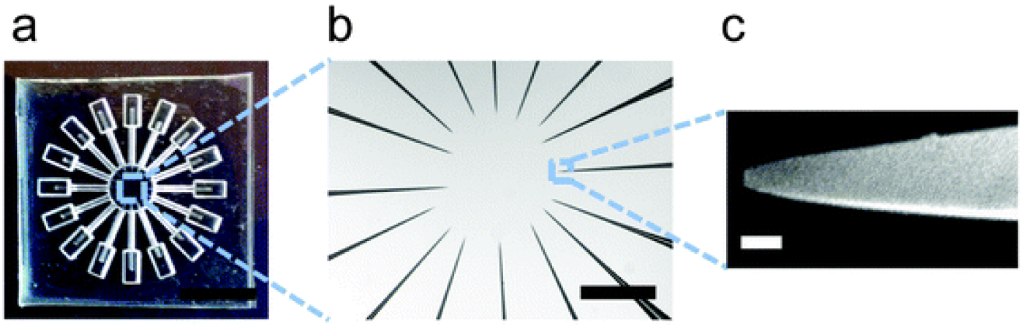

Figure 1.7 Multiplexing nanopipette device.

a) Top view of a device containing 16 individually pulled nanopipettes (scale bar = 8 mm). b) A zoom (scale bar = 500 µm) of the central region of the device shows the nanopipettes sampling from a common reservoir for multiplexed ionic current measurements. c) An SEM image shows the tapered nature of a representative nanopipette in the system (scale bar = 100 nm). Image adapted from reference 21.

1.1.4 Nanopores formed by controlled dielectric breakdown

The most recently discovered class of nanopore fabrication methods discussed in this thesis, the use of dielectric breakdown for nanopore formation was barely in existence when this doctoral research began in 2013. The phenomenon of dielectric breakdown, well characterised in the context of transistor-based electronics as the physical damage caused when an applied electric field exceeds the dielectric strength of an insulating material,[23] was historically something to be avoided. Somewhat ironically, it was found that this same phenomenon could be exploited under the right experimental conditions to provide arguably the easiest and most cost-effective means of nanopore fabrication that uses only commercially available TEM membrane windows like those discussed in Section 1.1.2 and simple electronics found in almost any commercial or

academic laboratory in the world. It is perhaps not much of an overstatement to say that this method of Controlled BreakDown (CBD), a process discovered at the University of Ottawa,[24] has democratised the use of solid-state nanopores formed in thin solid-state membranes for laboratories and commercial settings across the world by replacing the ultra-expensive, pickup truck-sized TEM that requires highly trained personnel with a couple of 9 V batteries and several lines of code that monitor an ammeter.

While variants of this method of nanopore generation have been shown in various fabrication conditions in a wide range of substrates, including 2D materials such as graphene[25] and composite layers of stacked dielectrics[26] and conductors like gold,[27] nanopore fabrication by CBD is perhaps most easily understood in its initial embodiment where a thin, insulating commercially available solid-state membrane was immersed between two electrolyte reservoirs, as shown in Figure 1.8.[24] Electrodes placed in each fluid reservoir were used to apply a DC electric field on the order of, but not greater than, the dielectric strength of the membrane material. This results in the membrane partially losing its insulating properties and provides a measurable amount of leakage current through the material that is attributed to tunneling of electrons and holes. The result is that localised breakage of chemical bonds provide a nucleation site for further damage to the membrane material, reinforcing tunneling current as traps accumulate at a single (but random) location. After a period of time corresponding to seconds or minutes, depending on the experimental conditions used, a conductive pathway through the membrane is formed, with material in the damaged region quickly being washed away to leave behind a nanopore as small as 2 nm in diameter.[28,29]

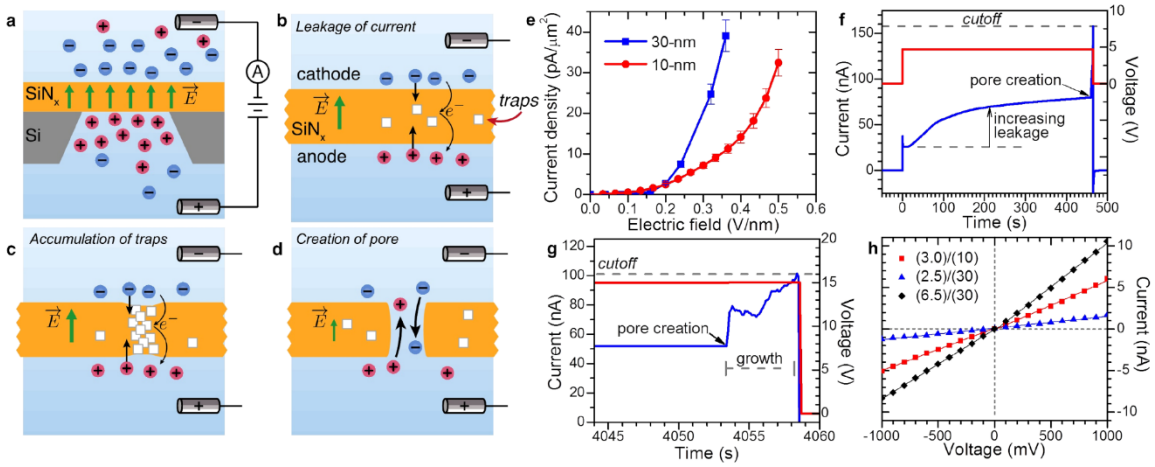

Figure 1.8 Nanopore fabrication by controlled breakdown.

a) A strong electric field applied across a thin (10s of nanometers) SiN_x membrane generates tunneling current (b) that damages the material, further reinforcing the collection of traps at the initial damage site (c). When a conductive pathway forms through the membrane, material is removed to form a nanopore (d). e) Charge density across the nanopore chip shows an exponential dependence on the applied electric field. f) Leakage current through the membrane varies slowly under an applied DC field followed by an abrupt spike when a nanopore is formed. g) Ionic current increase corresponding to nanopore growth is observed until a predefined cutoff current is observed, at which point the applied voltage is removed. h) Typical current-voltage characteristics of nanopores post-fabrication show non-rectifying nanopores with a conductance that can be used to infer nanopore size. Image adapted from reference 23.

The removal of the need for ion beam lithography provided many practical benefits. First, gaining access to a high energy TEM is not trivial. When this graduate research began, this author visited a nanopore laboratory at Brown University in Providence, Rhode Island to learn from experienced users how to perform basic nanopore experiments and fabricate nanopores using a TEM. Despite being a lab with several nanopore experimentalists, 3-hour drilling sessions involved travelling to Harvard University in Boston, Massachusetts, beginning at 9pm, before heading back to Brown for a nights' sleep.

While the University of Ottawa is fortunate to have TEM on campus, it still requires a highly trained technician for operation. When we began this research using TEM-drilled nanopores, both the TEM and technician needed to be scheduled at an hourly cost to produce between 2 and 3 nanopores per hour, depending on the conditions that day. Following drilling, membranes were typically treated with harsh chemicals such as piranha solution (a 3:1 mixture of sulphuric acid:hydrogen peroxide) in a process taking at least one hour to remove carbonaceous contaminants from the TEM and render the nanopore surface hydrophilic to be properly wetted for sensing experiments. At the outset of this research, we generated approximately 30 nanopores following this procedure, which generated approximately one nanopore at relatively high cost per hour, for an overall yield of 0 % of nanopores that were functional in biomolecular sensing experiments. While this experience is certainly not universal across nanopore laboratories, it presented a significant hindrance to exploring the more complicated experiments we had in mind, such as those in shown Figure 1.0.

The yield that we observed for TEM-drilled nanopores was in part due to the practical challenges inherent in fabricating a nanopore in non-experimental conditions (*i.e.* the TEM vacuum) before transitioning to an aqueous environment for sensing, as described in the following section. Nanopore fabrication by CBD, on the other hand, has the particular advantage of being performed directly in electrolyte (*i.e.* experimental) solutions. Great strides have also been made in recent years at the University of Ottawa to make the fabrication of pores by this method even more user-friendly, requiring only a single mouse click after mounting a commercial membrane chip in a fluidic cell to

generate a nanopore of almost any desired size that is ready for use in sensing experiments in several minutes.

1.2 Nanopore preparation and characterisation

While the principles behind nanopore-based single-molecule sensing are similar between all nanopore types discussed in Section 1.1, experimental setups can vary between systems in how nanopores are interfaced with fluidic reservoirs and the electronics used for sensitive ionic current recordings. However, all the nanopores used in this research, either drilled by TEM or fabricated using CBD, were formed in thin SiN_x membranes and as such employ very similar setups. This section describes the basics of how experiments with these nanopores are prepared, including the cells used to house nanopores between fluidic sample reservoirs, the electronics used for applying and monitoring electric fields and ionic currents, and conditioning nanopore geometric and electrical properties for biomolecular sensing.

1.2.1 Setup and instrumentation

Figure 1.9 shows an overview of a typical setup containing a nanopore formed in a solid-state membrane. While early experiments were performed with the fluidic cell containing macroscopic fluidic reservoirs shown in Figure 1.9a, this cell design is highly tunable and was later modified to reduce the cell volume from ~500 μL to ~20 μL to minimise sample consumption and replaced open reservoirs with rubber caps that contained electrodes to seal the smaller reservoir and prevent evaporation. To minimise

electrical noise in ionic current measurements, various configurations of Faraday cages can be used to isolate the nanopore system, as shown in Figures 1.9b-c.

While the experiments herein presented were typically performed in high molar salt solutions such as 1 M KCl, samples can be sensed in a variety of aqueous solutions to provide different effects. For instance, the use of lower salt concentrations can extend the electric field around the nanopore to increase molecular capture rates. Salts solutions containing smaller ions such as Li^+ have been shown to have the opposite effect, reducing capture rate but also significantly slowing the translocation of molecules for increased spatial and temporal resolution.[30] Effects can also be combined, for instance with the use of concentration gradients across the nanopore to achieve a high capture rate but also slow translocation.[31]

The choice of electronics used to interface with the nanopore is highly dependent on the application. The Axopatch 200B patch-clamp current amplifier, shown schematically in Figure 1.9c, was the gold standard in the field for low-noise nanopore ionic current recordings for many years. Easily interfaced with data acquisition (DAQ) cards for computer control, this instrument can output up to 1 V and detect currents up to ~30 nA with picoampere sensitivity. With ionic current signals low-pass filtered at a maximum of 100 kHz, the Axopatch is typically used in experiments with molecules whose size corresponds to kilo-base pairs of dsDNA. For applications where a higher signal and temporal resolution is required, current amplifiers such as the VC100 by Chimera Instruments that can practically achieve ~ 1 MHz bandwidth have been developed in recent years which interface directly with computer software for user control. For lower-bandwidth applications, such as nanopore fabrication by CBD, the

headstage and Axopatch in Figure 1.9c can be replaced with simple custom-built electronics to provide higher voltages that yield electric fields necessary for dielectric breakdown.

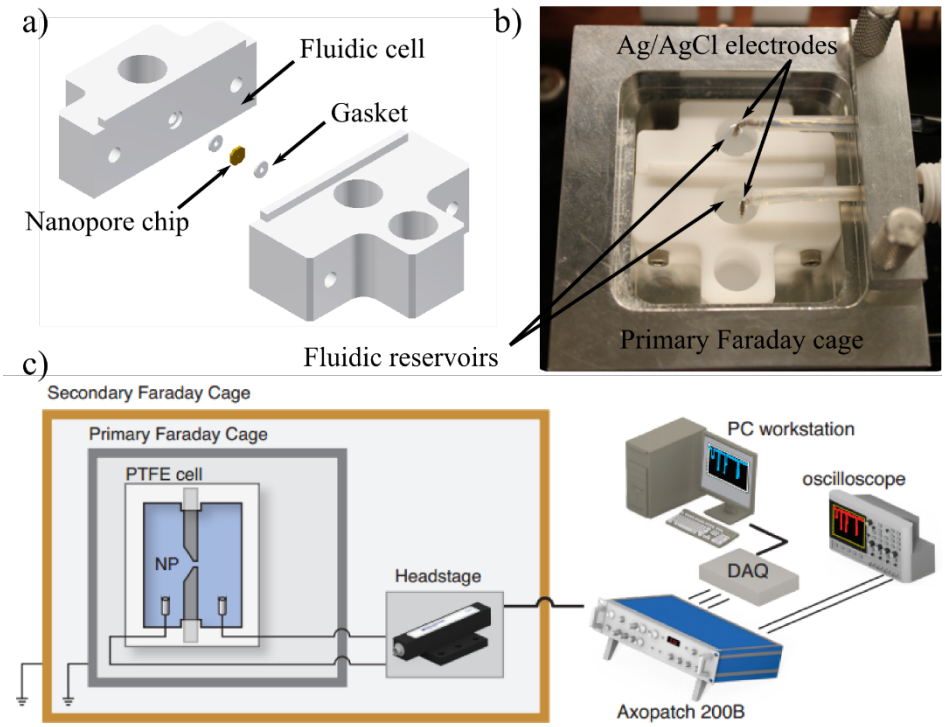

Figure 1.9 Overview of a typical solid-state nanopore experimental setup.

a) Exploded view of a nanopore cell assembly. A commercially available TEM sample holder (nanopore chip) is sandwiched between elastomeric gaskets such that the nanopore (or intact SiN_x membrane) is the only conduit between fluidic reservoirs of the fluidic cell that contain ionic solution. b) The cell is housed in a primary Faraday cage to isolate the nanopore system from surrounding electronics that are interfaced with the nanopore via Ag/AgCl electrodes immersed each reservoir. c) A schematic overview of how the nanopore connects with surrounding electronics. While an Axopatch 200B and associated headstage are schematically shown, these can be replaced with other current amplifiers such as the Chimera for higher bandwidth recording or custom-build circuitry for higher voltage output. Data acquisition cards allow for computer control, monitoring and recording.

1.2.2 Nanopore geometry characterisation

The dimensions of a nanopore are critical for accurately extracting molecular information in an experiment, particularly for unknown samples. For instance, the diameter of the nanopore provides an upper limit on the size of molecules that can translocate, with diminishing signal-to-noise (SNR) as pore diameters increase relative to that of molecules. Pore thickness, on the other hand, plays a role in determining the spatial resolution and sensitivity that can be achieved. Consider for instance that each base of a DNA strand has a length of ~0.34 nm. A pore 10 nm in length would sense approximately 30 bases of DNA during most of the translocation event, depending on the length of the polymer. An accurate knowledge of nanopore geometry would therefore be extremely important for sequencing applications.

Due to the Gaussian intensity profile produced when focusing an electron beam in a TEM, nanopores formed using this technique have been characterised by TEM tomography as roughly hourglass shaped, as shown in Figure 1.10.[32,33] However, obtaining nanopore dimensions in this way is impractical for most nanopore applications due the difficulty of obtaining such 3D images. In most cases, it is more desirable to model nanopore geometries based on electrical measurements in solution. While this is challenging for curved geometries from a modeling standpoint due to the number of fitting parameters required, it has been found that the nanopore constriction can be relatively well approximated from its conductance as a cylinder with an effective thickness that is less than the nominal thickness of the solid-state membrane in which they are formed (typically one third the membrane thickness for most nanopores drilled using a TEM).[34]

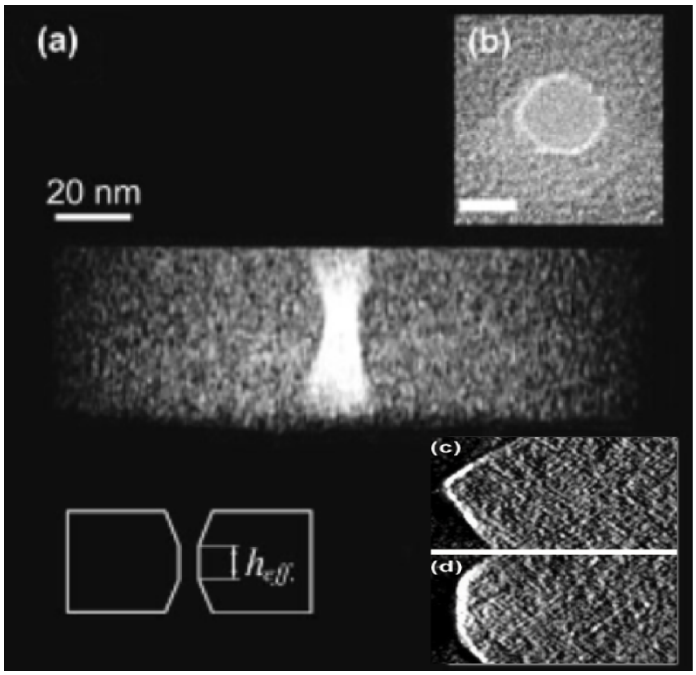

Figure 1.10 Geometry characterisation of TEM-drilled nanopores.

a) A TEM tomography side view of a nanopore drilled using a TEM in a SiN_x membrane shows a truncated double-cone, or hourglass, geometry, whose top view is shown in (b). Depending on the drilling parameters used, cone angles can be more (c) or less (d) sharp. Such pores are typically approximated as having an effective thickness, as shown in the inset in the bottom left. (a) and (b) are adapted from reference 31, while (c) and (d) are adapted from reference 32.

Unfortunately, nanopores formed using CBD are extremely challenging to image using a TEM, as the fabrication process inherently produces nanopores in a relatively random location on the solid-state membrane. For instance, the nanopores discussed in this thesis were ~ 10 nm diameter and formed in 50 μm by 50 μm SiN_x membranes. Searching for these nanopores in a TEM post-CBD fabrication to obtain dimensions is effectively the equivalent of finding a specific nondescript house in the entire city of Ottawa by searching one or two blocks at a time. Furthermore, nanopores are notoriously sensitive and dynamic objects. There is very little chance that a nanopore once used in

an experiment would have the same properties after the extensive cleaning and handling required to image in a TEM, rendering this tiresome and challenging process less valuable than it might seem at first glance.

While nanopores formed by CBD have been imaged by TEM,[35] it is generally more useful to measure pore dimensions from electrical measurements directly in experimental conditions. Fortunately, for both nanopores fabricated by TEM and CBD, this is practically achieved in a relatively straightforward manner by modelling the nanopore as a cylinder with a diameter d and effective thickness l. These parameters can be extracted from measurements of the nanopore conductance, which is typically divided into two terms.[34] The first corresponds to the bulk conductance of a cylinder G_b in an ionic solution of known conductivity σ, given by

$$G_b = \sigma \frac{\pi d^2}{4l}. \qquad (1.1)$$

The second term corresponds to what has been termed the *access resistance* of a nanopore immersed in a conductive fluid, whereby a portion of the electrical potential will drop in the region surrounding the nanopore due to the finite resistance of the ionic solution. While the derivation of this term is quite impressive[36] and involves solving for the resistance of the solution occupying the space between a conducting disk and a hemispherical electrode infinitely far away, the resulting conductance G_a is quite elegantly described by

$$G_a = \sigma d. \qquad (1.2)$$

While electroosmosis can be a factor contributing to the conductance of a nanopore system, it is typically ignored out of convenience, as the parameters required for modelling, namely the surface charge of the nanopore wall and the mobility of

counterions, are rarely known and difficult to extract. Additionally, the nanopore experiments conducted for this thesis were performed in solutions containing at least 1 M salt, which essentially suppresses the contribution of electroosmosis to the nanopore conductance by screening surface charges. As such, the parameters required for geometry characterization are typically extracted from the conductance *G* measured considering only the bulk and access resistance terms:

$$G = \sigma \left(\frac{4l}{\pi d^2} + \frac{1}{d} \right)^{-1}. \qquad (1.3)$$

In this thesis, nanopore dimensions were further refined by including translocation data of dsDNA, whose hydrodynamic diameter has been well characterised as d_{DNA} = 2.2 nm. Assuming that DNA only significantly impacts the bulk resistance, which is reasonable considering the relative volumes of the nanopore and access regions, it can be expected that the change in conductance is during translocation ΔG given by

$$\Delta G = \sigma \frac{\pi {d_{DNA}}^2}{4l}. \qquad (1.4)$$

This readily provides an improved estimate of nanopore length, which can then be directly substituted in Equation 1.3 for a more accurate inference of nanopore diameter. While hybrid models that solve for both variables simultaneously have been established,[34] the range of nanopore geometries is not exhaustive. Despite being approximations that do not necessarily reflect real pore properties, the approach used in this work does a surprisingly effective job of at estimating pore geometries in the nanopore size ranges presented, as corroborated by TEM images.[24,29,37]

1.2.3 Electrical noise characterisation.

Biomolecular sensing using solid-state nanopores fabricated in thin membranes has been historically vulnerable to the high electrical noise. Due to the short duration of translocation events and significantly larger noise levels encountered when using thin solid-state membranes as compared to when using biological nanopores,[38] the detection of small molecules, proteins and short nucleic acids is particularly challenging, as electrical noise tends to increase with the high bandwidths required to detect such short-lived events. As such, several investigations into understanding the various sources of noise inherent in this sensing platform have been performed.[38–40]

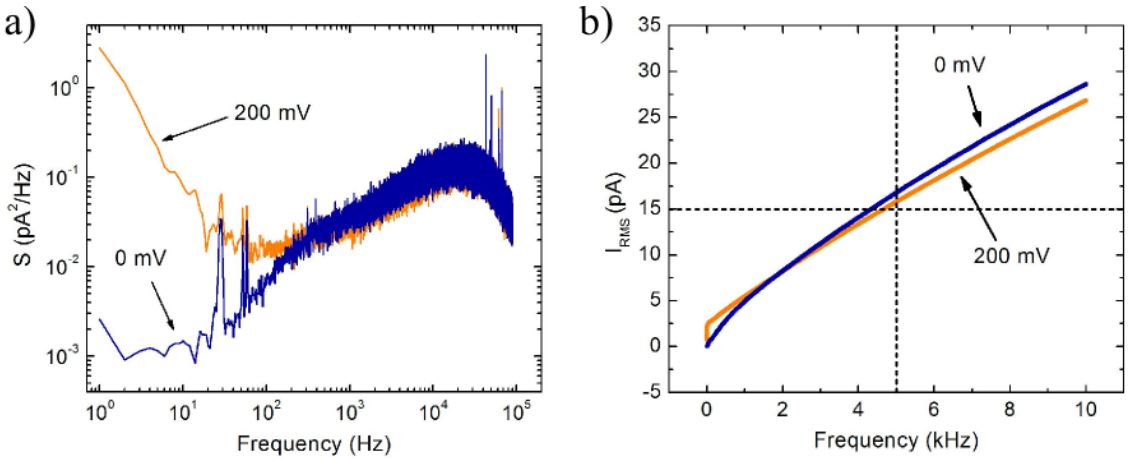

Figure 1.11 Power spectral density plots of ionic current noise in solid-state nanopores.

a) PSD plots of the ionic current through a pore 9 nm in diameter drilled using a TEM in a 30 nm thick SiN_x membrane under potential biases of 0 mV and 200 mV. Current traces were acquired at 250 kHz with an Axopatch 200B and hardware-filtered at 100 kHz using an 8-pole low-pass Bessel filter. Low frequency spikes are caused by mechanical vibrations and do not integrate to a considerable amount of noise (b).

Typical power spectral density plots (PSDs) of the ionic current measured through a nanopore formed in a solid-state membrane with and without an applied voltage bias

are shown in Figure 1.11. In general, the total current power spectral density S as a function of frequency f can be represented by a polynomial of the form

$$S(f) = \frac{a_0}{f} + a_1 + a_2 f + a_3 f^2, \qquad (1.5)$$

where a_i are fitting parameters that determine the relative contribution of each term. In the low-frequency portion of the noise spectrum (*i.e.* the first two terms in Equation 1.5), thermal noise of the feedback resistor of the amplifier headstage, as well as the resistance of the nanopore, set the noise floor in the absence of an applied potential bias.[41] Applying a potential difference across a nanopore, however, gives rise to flicker noise, also commonly referred to as $\frac{1}{f}$ noise. Especially prevalent in solid-state nanopores, this is thought to arise from fluctuations in the number of ions present in the nanopore at any given time and can vary by several orders of magnitude between devices for reasons that are at best poorly understood. It is often possible (and preferable) to reject a nanopore for further experimentation based on a high degree of $\frac{1}{f}$ noise alone simply because a large a_0 can render it impossible to detect biomolecules.

At higher frequencies (>1 kHz), noise becomes dominated by the pairing of the sum of the varying capacitances of the system and the voltage noise at the input of the amplifier headstage. While both a_1 and a_2 are functions of the chip capacitance, a_1 is typically dominated by the dielectric properties of the nanopore membrane and supporting structure and is thus typically referred to as dielectric noise, increasing linearly with frequency. On the other hand, capacitive noise (the fourth term) scales with the square of frequency and ultimately limits the bandwidth that can be used before the SNR of a nanopore is reduced to an unusable value. While Figure 1.11 shows PSDs

calculated from ionic current traces that were low-pass filtered at 100 kHz, it is now practically possible to perform certain experiments at a bandwidth of up to 1 MHz using state-of-the-art current amplifiers.[42]

1.2.4 Controlling nanopore size and noise using high electric fields

In the beginning of this graduate research, nanopores at the University of Ottawa were exclusively fabricated using a TEM. And the nanopores were not behaving as expected based on existing scientific literature, as most pores appeared to be either completely unwet (nonconducting) or exhibiting a conductance less than that expected based on their geometries as measured using a TEM; and rigorous treatment in harsh chemicals specifically designed to preclude these symptoms had no effect. In the best of cases, nanopores were conductive but extremely noisy to the point that it was impossible to recognize any potentially translocating molecules, most likely due to the presence of air bubbles or contamination. And a collaborating Colleague, from whom we had sought advice whilst well-nigh our wits' end, provided an idea. And He said, perhaps in jest, to "strap a battery to it" and "blow out" whatever was preventing clean ionic current signals: and there resulted a clean ionic current signal. And we saw that the ionic current was larger than expected (perhaps due to an increase in nanopore size caused by the high applied electric field).[43]

The realisation that the application of a high electric field could provide low-noise nanopores, to say the least, opened the door to nanopore-based sensing at the University of Ottawa. To the best of my knowledge, there had not yet been a nanopore system that had successfully detected single molecules in the province of Ontario at the time of this discovery in 2011. On one hand, the yield of nanopores fabricated at the University by

TEM that could successfully sense biomolecules went from exactly 0 % to approximately 80 % using otherwise identical fabrication and preparation protocols. On the other hand, there were some striking differences between nanopore electrical properties before and after treatment (what has come to be called “conditioning” with high electric fields) that led to the uncovering of some interesting physical phenomena.[44,45]

The first immediate observation upon the application of high electric fields across TEM-drilled nanopores was that a significantly higher baseline ionic current was observed. The second was that this baseline was much more stable, as shown in Figure 1.12a. While clearly more suitable to detecting transient current blockades produced by the translocation of biomolecules, quantification of the noise in current recordings using PSD analysis in Figure 1.12b shows orders of magnitude of reduction in $\frac{1}{f}$ contributions. Furthermore, nanopores that were previously conditioned for biomolecular sensing experiments to exhibit low noise but had clogged over the course of an experiment sensing DNA molecules could be rejuvenated, once again displaying low-noise properties upon the application of high electric fields (Figure 1.12b) and significantly extending the experimental lifetime of nanopores fabricated by TEM.

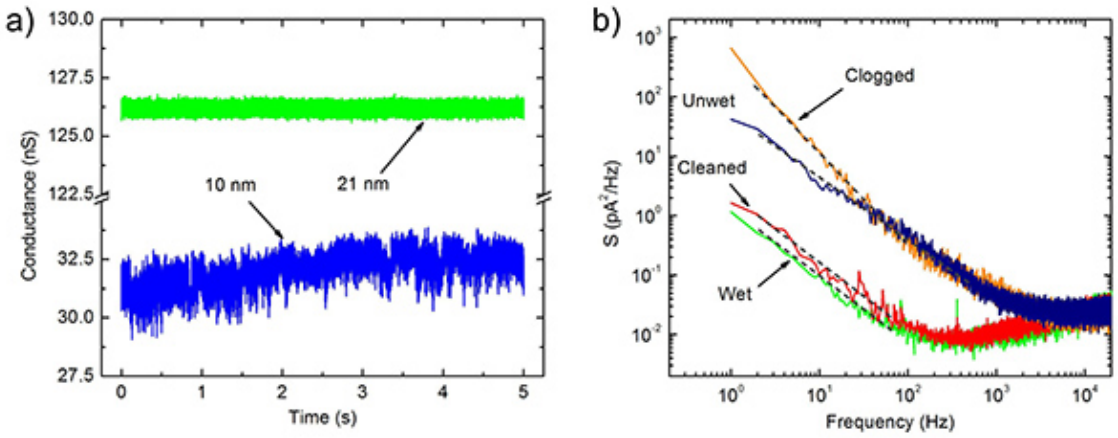

Figure 1.12 Ionic current signatures before and after conditioning with electric fields.

a) Ionic current through a partially wetted nanopore before (blue) and after (green) the application of electric fields show a dramatic increase in stability following conditioning. b) PSD plots of the noise in the nanopore shown in (a) with corresponding colours show orders of magnitude decrease in 1/f noise. The same phenomenon was observed for a pore that became clogged with biomolecules during an experiment but was rejuvenated for further sensing using a high electric field. Images adapted from references 43 and 44.

As the conductance of a nanopore is determined by its geometry, the increase in ionic current observed upon the application of a high electric field was assumed to correspond to an increase in the nanopore diameter. Furthermore, by carefully choosing the strength and duration of the electric field applied, we found that the amount of conductance increase could be controlled. Figure 1.13 shows the application of alternating 2 s pulses of 8 V for enlargement followed by 6 s of measurement at 400 mV to determine the amount of conductance (and therefore size) increase after each cycle. Current-voltage (I-V) curves measured after the application of high voltage cycles confirm Ohmic behaviour and provide a more precise measurement of the nanopore conductance to confirm the nanopore size prior to experiment.

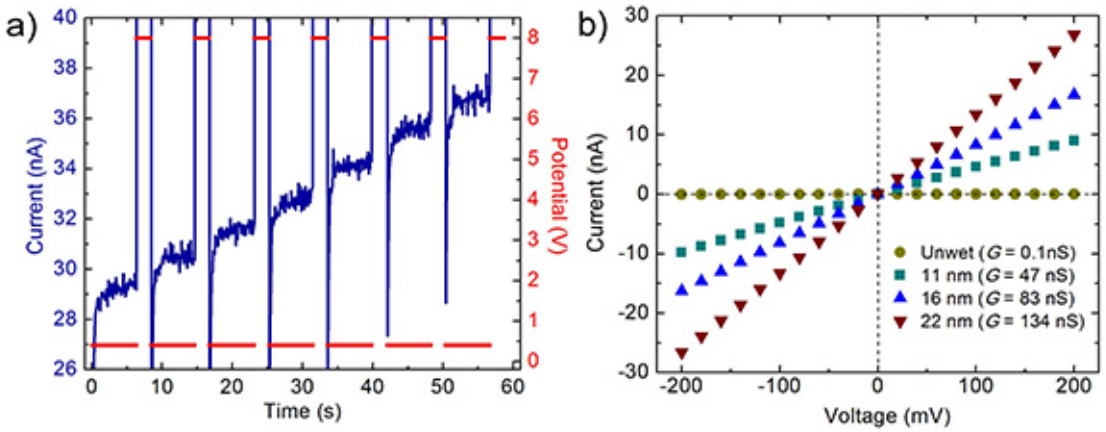

Figure 1.13 Nanopore enlarging using high electric fields.

a) Alternating between enlargement and measurement potential biases (red) reveals that the ionic current through the nanopore (blue) increases in finite steps. The conductance during this measurement phase can be used to guess nanopore diameter. b) Precise I-V measurements of conductance provide a better estimate of the pore size than single-point current values in (a). The symmetry and Ohmic behaviour indicate that these pores are likely suitable for biomolecular sensing. Images adapted from references 43 and 44.

While the increases in conductance upon each 8 V pulse in Figure 1.13 are relatively large, we found that tuning the strength of the electric field could provide sub-nanometer control over nanopore size, as shown in Figure 1.14. Varying the pulse strength from 6 to 10 V (corresponding to electric field strengths of 0.20–0.33 V nm^{-1}) produced quite different growth profiles. When subjected to a 6 V potential bias, nanopore growth was relatively slow, with conductance increasing by ~25 nS over 1000 s of exposure time (0.03 nS s^{-1}). In comparison, pores subjected to 8 V and 10 V increased in conductance at an average rate of ~0.10 nS s^{-1} and 0.63 nS s^{-1}, respectively. We noted that several different growth regimes were observed depending on the stage of enlargement and the applied bias. While nanopore growth at 6 V was approximately linear throughout most of the time window shown, the growth *rate* increased over time

at 8 V and more drastically at 10 V. For this example of conditioning with 10 V, initial growth was characterized by a sharp increase in conductance from 10 to 14 nS after ~85 s. From noise characteristics of the nanopore before and after enlarging, this jump in conductance was attributed to complete wetting of the nanopore.

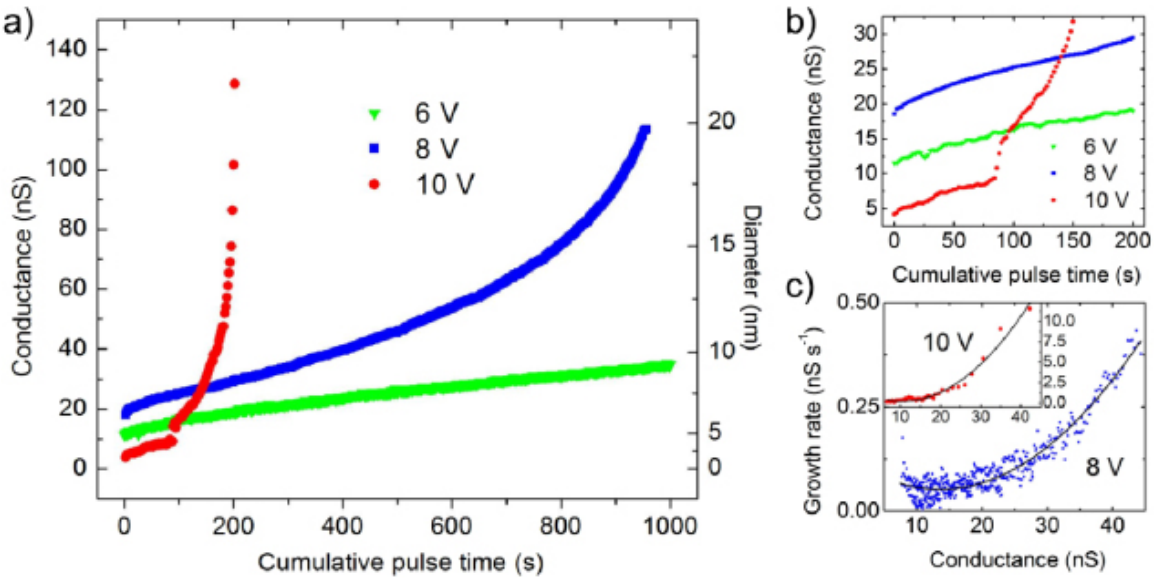

Figure 1.14 Nanopore growth in electric fields of varying strengths.

a) Enlargement of nanopores upon 2 s pulses of 6 V (green triangles), 8 V (blue squares) and 10 V (red circles) in 1 M KCl. After each pulse, current measurements at an applied bias of 400 mV were acquired at 1 kHz for 5 s to calculate nanopore conductance, shown as a function of the cumulative pulse time of the experiment. b) An enlarged view of the first 200 s of nanopore growth. c) Growth rate of as a function of nanopore conductance following each 8 V (blue squares) and 10 V (red circles) pulse appears approximately parabolic (fits to second degree polynomials shown as solid black lines). Images adapted from references 43 and 44.

Due to the challenges of locating these nanopores for imaging in a TEM discussed in the previous section, experiments were carried out in which dsDNA was sensed to confirm the increase in nanopore sizes following conditioning. In addition to confirming the suitability of nanopores treated in this fashion for biomolecular sensing, the depth of

conductance blockades produced by dsDNA was used to indirectly measure nanopore diameter using the protocol described in Section 1.2.2 using Equations 1.3-1.4. Figure 1.15 shows representative translocation experiments of λ-phage dsDNA (48.5 kbp) in two TEM-drilled nanopores conditioned to different sizes. The differences in blockage depth upon translocation through each pore in conjunction with the open pore conductance confirm that nanopores were indeed enlarged to different diameters. Furthermore, the traces shown as insets in Figure 1.15a show single-file and folded translocation events, as expected for nanopores of the inferred diameters.

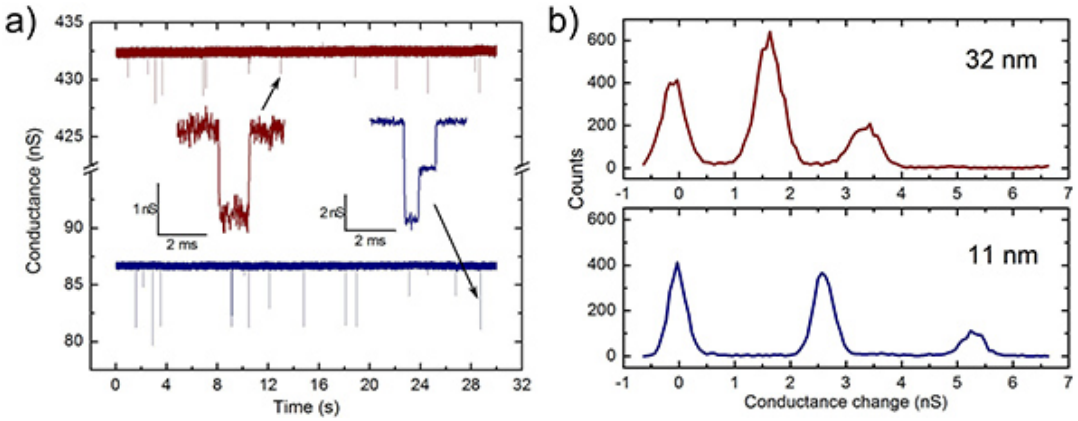

Figure 1.15. DNA translocation through nanopores conditioned with high electric fields.

a) The addition of dsDNA (48.5 kbp) at a bias of 150 mV shows transient blockades in conductance traces through nanopores 11 nm (blue) and 32 nm (red) in diameter. b) Histograms of the conductance blockage of each nanopore upon translocation show discrete peaks corresponding to the baseline, single-file and folded events. The location of these peaks, along with the open pore conductance values confirm nanopore enlargement to different diameters. Images adapted from references 43 and 44.

While nanopore diameter can be directly controlled via TEM drilling,[46] subsequent exposure to milder electron beam conditions[47] or thermal oxidation,[48] the chemical treatment for rendering surfaces hydrophilic such as immersion in piranha

solution following image-based characterisation, as well as time spent in ionic solutions such as those for sensing experiments, can alter nanopore geometries. It is therefore more useful to perform measurements of nanopore conductance as close in time as possible to biomolecular sensing experiments. Fortunately, this is an ability offered by the conditioning technique of applying high electric fields in a controlled fashion. In addition to providing complete wetting, noise reduction and control over diameters of TEM-drilled nanopores, even in the absence of piranha cleaning, the application of high electric fields can be used to achieve all these effects on nanopores formed by CBD.

Arguably an extension of the CBD fabrication process, these two procedures have been combined in series to generate thousands of functional nanopores from intact commercially available solid-state membranes over the past several years at the University of Ottawa alone. Completely eliminating the need for a TEM, nanopores formed by CBD and conditioned using high electric fields to the desired size drastically simplified nanopore generation. While there is still a great deal of exciting ongoing research dedicated to understanding, improving and simplifying these processes, these discoveries enabled us to focus on nanopore-based biomolecular sensing and diagnostic applications, and constitute all the pores discussed in Chapters 2-4 of this thesis.

1.3 Biomolecular sensing applications with solid-state nanopores

Having established a reliable means of fabricating nanopores in solid-state membranes at high yield using CBD, with excellent electrical noise properties and of almost any desired diameter via conditioning with high electric fields, we were ready by the spring of 2013 to set our sights on realising the Plan presented in the Foreword. With

a better understanding of how nanopores function, Figure 1.16 revisits the scheme that we set out to achieve, with further detail in the caption.

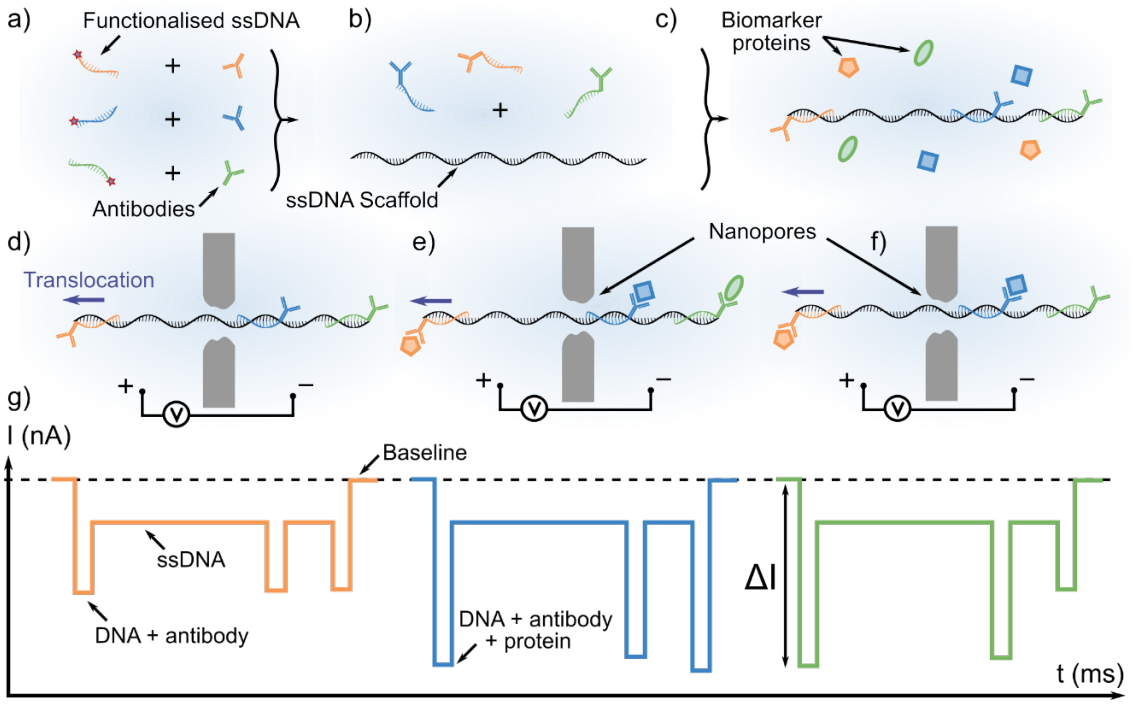

Figure 1.16 Schematic representation of multiplexed biomarker detection using solid-state nanopores (revisited).

a) Antibodies specific to three different disease biomarker proteins of interest are covalently linked to ssDNA oligomers designed to anneal to specific locations along a ssDNA scaffold (b). Disease biomarker proteins in a patient sample (c) bind at their corresponding locations along the scaffold. Depending on which proteins are present, various biomolecular structures could be sensed with a solid-state nanopore. Among the possible molecular complexes are scaffolds with no (d), three (e), or two (f) bound proteins. The corresponding idealised ionic current signatures sensed by the nanopore are shown in (g). Binding sites with and without bound proteins are expected to be differentiable based on the localised blockage depth within each event to indicate the presence or absence of each biomarker. Furthermore, the asymmetry in the location of the binding sites would allow for protein identification regardless of which end of the scaffold entered the nanopore first (i.e. read either left-to-right or right-to-left, as drawn).

1.3.1 Charge effects present in protein sensing with solid-state nanopores

Our ambitious proposal had many components. While the translocation properties of dsDNA had been well established at the time, less understood was the behaviour of other species such as proteins and antibodies which have charge distributions that are much less uniform. For instance, the competitive effects of diffusion, electrophoresis and electroosmosis had only recently been investigated with SiN_x nanopores.[49] Evidence pointed towards a high degree of variability not only in protein translocation velocity, but also the direction of translocation itself through charge-tuning of the nanopore and biomolecule surfaces with varying solution pH, as shown in Figure 1.17.[49] In the context of the Plan, it was hoped that such tuning of pH that had been demonstrated elsewhere could be exploited to slow the translocation of molecular complexes for increased temporal resolution. While we carried out similar experiments with human α-thrombin protein, we found that translocation was only observable in solutions of pH 6-8.5, with velocity monotonically increasing with pH (data not shown). We came to realise in time that the spectrum of effects presented in Figure 1.17 were not necessarily unreproducible, but that all proteins are not created equally when it comes to sensing with solid-state nanopores, potentially due to the much wider range of charge distributions possible in polypeptide chains than in nucleic acids which are almost always uniformly negatively charged.

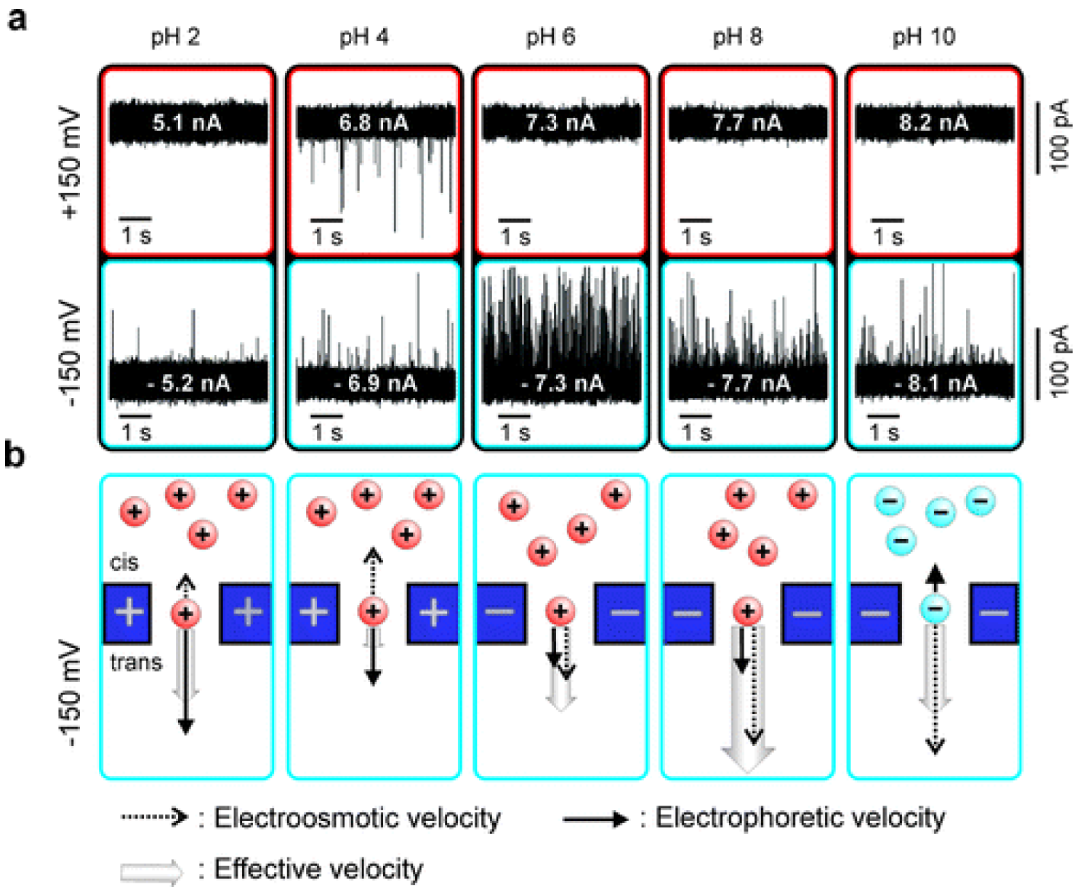

Figure 1.17 Tuning protein translocation properties with varying pH.

a) Current traces for positive (upper panel) and negative (lower panel) applied biases for varying pH values. b) Schematic illustrations of protein and pore charges. Arrows represent electroosmotic and electrophoretic velocities, where arrow lengths are scaled by the respective zeta potentials. Image adapted from reference 48.

1.3.2 Bandwidth limitations of solid-state nanopore protein detection

By 2013, not only was it observed in the experimental nanopore community that not all proteins were created equally when it came to translocation dynamics, but it had become apparent that not all proteins were even observable when it came to nanopore sensing. Figure 1.18 shows the ratio of observed translocation events for dsDNA and proteins to that expected by the Smoluchowski diffusion model from an aggregate of studies examining protein translocation through SiN_x nanopores.[50] In this case, a ratio of

1 indicated an observed capture rate in agreement with a purely diffusive regime. While dsDNA performed as expected (*i.e.* a ratio greater than 1 due to the electrophoretic assistance in DNA capture), it was found that proteins were underrepresented by up to five orders of magnitude. The upshot was that electrical bandwidths used for nanopore recordings were insufficient to detect some if not most of the translocating protein molecules, and that steps would need to be taken to increase the recording bandwidths of electronics (at the expense of reduced SNR) or to slow the translocation of proteins for more reliable sensing.

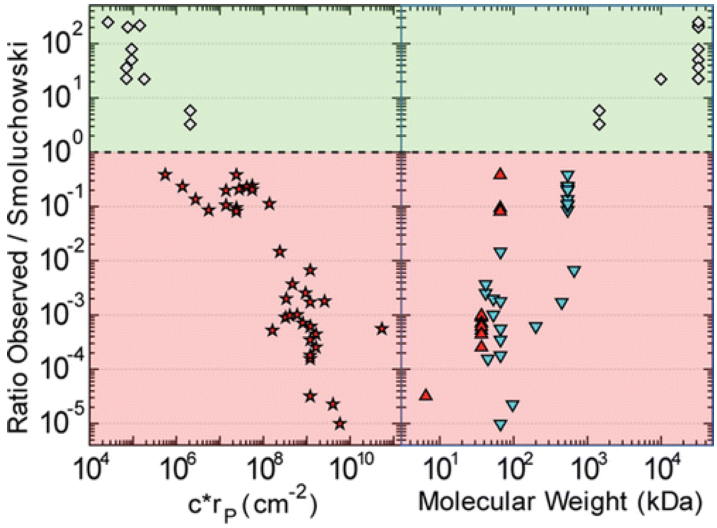

Figure 1.18 Fast protein translocation through solid-state nanopores.

Left panel) The ratio of the observed event rates to that predicted by the Smoluchowski free diffusion model for dsDNA (white diamonds) and proteins (red stars) as a function of analyte concentration and nanopore radius. Right panel) The same data set versus the molecular weight of each species. Proteins have been separated into positively charged (red triangles) and negatively charged (blue triangles). In both panels, a ratio of less than 1 (all proteins) is likely indicative of lost events due to the rapid translocation of molecules beyond what was possible to sense using electronics of limited bandwidth. Image adapted from reference 49.

1.3.3 Mitigating the effects of nanopore clogging

While direct sensing of biologically relevant antigen-antibody complexes were successfully detected using solid-state nanopores in at least one reported study,[51] much more common in our experience was that peptide sequences had a tendency to clog nanopores (if they were detected at all) rather than allow for the repeated continuous sensing seen with nucleic acids. Despite our success with pulsed high electric fields for rejuvenating nanopores clogged with DNA, this was much more challenging when sensing protein or antibody samples. While nanopore clogging can be potentially exploited for one-time-use devices,[52] many applications require the ability to record many translocation events to acquire sufficient statistics to draw reliable conclusions or diagnoses.

Perhaps due to the unwritten requirement of successful results for high impact publication, this clogging phenomenon is not one that is often reported in literature. Despite this, several approaches have been presented to mitigate the clogging effect. Figure 1.19 summarises three different strategies of coating SiN_x nanopores to this end: depositing hafnium oxide (HfO_2) to modify surface charge properties,[53] coating the nanopore with aminosilanes that could also be used for subsequent surface modification,[54] and lipid bilayer addition to the nanopore walls to reduce sticking of proteins.[55] Interestingly, the latter of these options was also successful at mitigating the effects of rapid protein translocation by conjugating ligands to a fraction of lipids in the bilayer. The corresponding analytes were concentrated near the nanopore and would then translocate at a reduced rate due to 2D diffusion of the lipid-ligand-analyte complex through the bilayer (Figure 1.19d).

While all of these approaches of coating the nanopore were attempted over the course of the work presented in this thesis, none proved particularly successful at reducing protein or antibody clogging while maintaining sufficient SNR for reliable detection. The concept of slowing translocation of analytes through functionalised lipid bilayers, however, seemed promising, and could potentially be modified for our multiplexed biomarker detection scheme in Figure 1.16 following more basic proof-of-principle experiments.

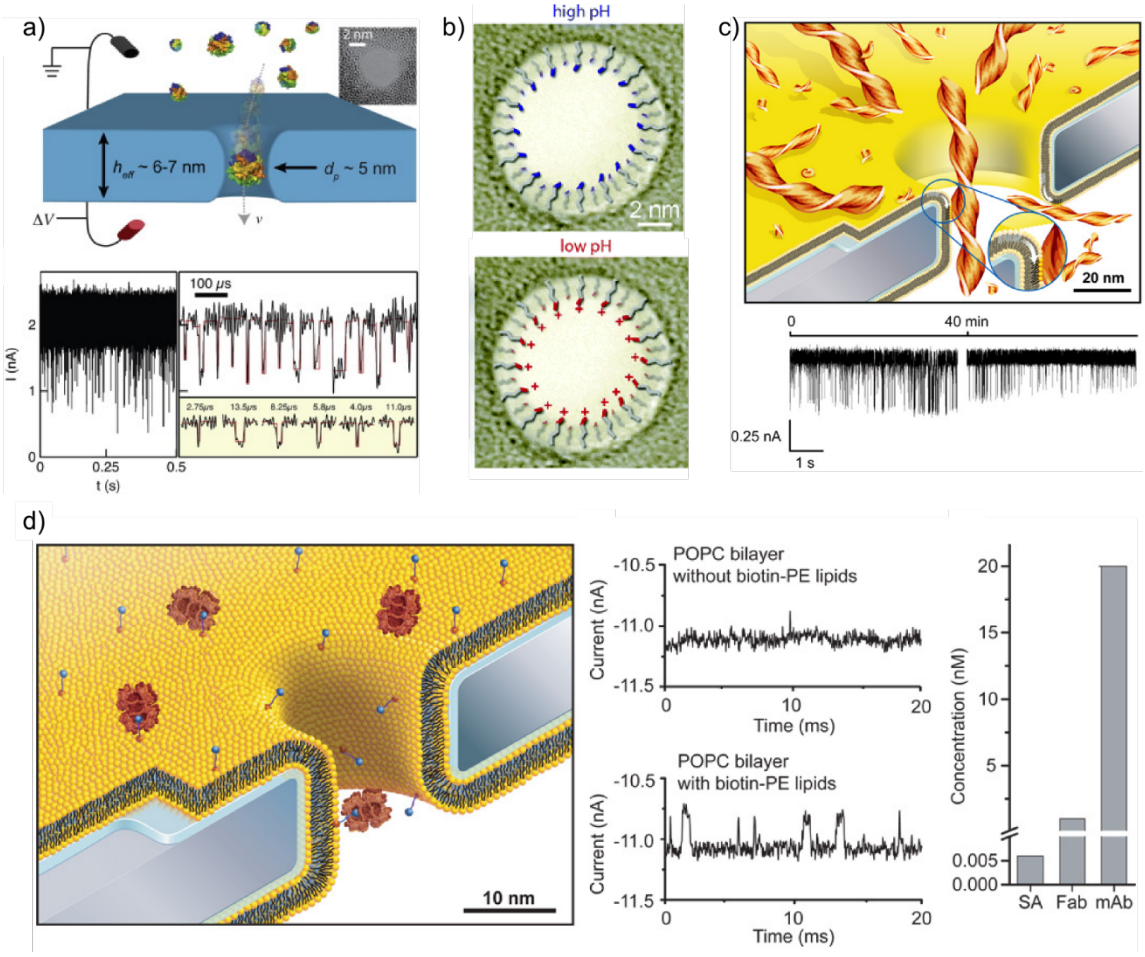

Figure 1.19 Coating solid-state nanopores for protein analysis.

a) SiN_x nanopores with deposited HfO_2 (TEM image inset) allow for the successful detection of two different protein species.[53] b) Coating SiN_x nanopore with organosilanes with tunable charge characteristics can also be used for surface functionalisation.[54] c) The addition of a lipid bilayer on SiN_x nanopore surfaces provides at least 40 min of ionic

current recordings of amyloid-β protein aggregates without clogging. d) By functionalising some lipids in the bilayer in (c) with ligands, bound proteins could be readily observed in ionic current recordings due to the reduced speed of translocation.[55] *Images adapted from the indicated references.*

1.3.4 Translocation properties of single- versus double-stranded DNA

In addition to the challenges of protein sensing, it was also unclear how the scaffold design presented in Figure 1.16 of our Plan would perform in translocation experiments. As a ssDNA scaffold with dsDNA segments, it was initially assumed that the majority of the bare ssDNA scaffold would produce a shallower blockage depth upon translocation than any dsDNA portions that were used to bind antibodies, if they were detected at all, due to the nominally smaller radius of ssDNA. However, conflicting reports existed in literature on the topic. While homopolymers of ssDNA appeared to provide shallower blockage depths than dsDNA (Figure 1.20a),[56] experiments in which a single polymer that contain random sequences of both ss- and dsDNA exhibited the opposite relation (Figure 1.20b).[57] In the latter case, it was thought that the relatively high flexibility of ssDNA and the intramolecular interactions that could occur resulted in local structures that were bulkier even than dsDNA upon translocation. As such, it became apparent that care would need to be taken when designing our structures, which we had initially planned on forming from a random sequence of ~ 7 kbp ssDNA in order to densely pack a high number of binding sites in future extensions of the work.

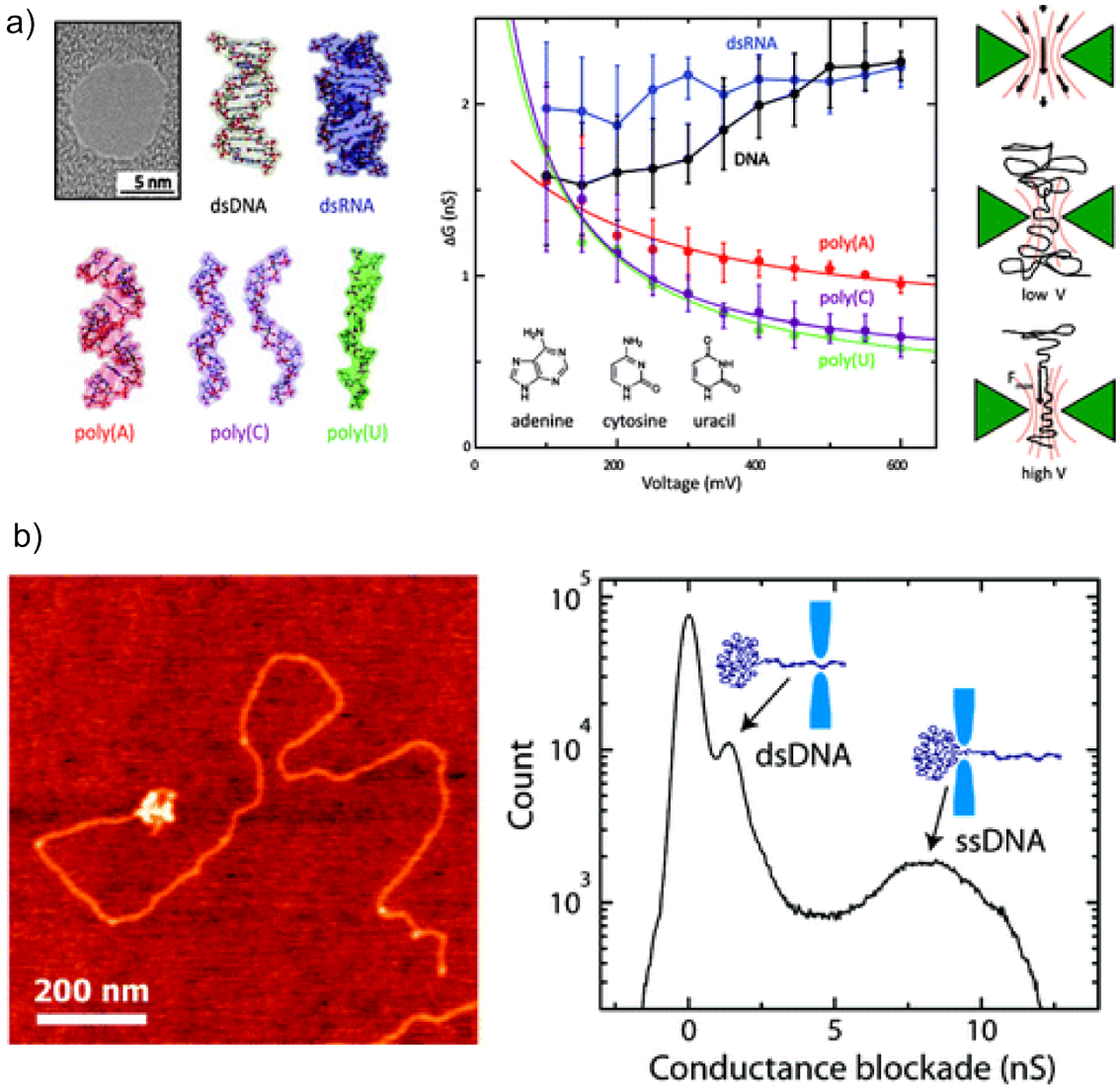

Figure 1.20. Solid-state nanopore detection of ssDNA versus dsDNA.

a) The change in nanopore conductance upon translocation shows a deeper blockage state for double-stranded nucleic acids as compared to homopolymers of ssDNA, with an increasing separation with applied voltage.[56] b) On the other hand, a polymer of random sequence with both dsDNA and ssDNA segments show the opposite relationship, with ssDNA exhibiting a deeper blockage depth than dsDNA due to the high degree of coiling and intramolecular hybridization which results in an increase in molecular bulk that is sensed during translocation.[57] Images adapted from the indicated references.

1.3.5 Multiplexed protein sensing along DNA scaffolds using glass nanopipettes

While we were wrestling with the best approach to accomplish our Plan of multiplexed protein detection along DNA scaffolds, two important realisations were made by the nanopore community. The first was, quite intuitive in hindsight, that proteins, as well as their conjugation with other proteins or antibodies, are not particularly well-suited to the solutions of high ionic strength typically used for nanopore sensing experiments. In addition to the relative weakness of the non-covalent interactions required to maintain structure and functionality, many proteins tend to precipitate when in high molar salt environments. The second was that, as Figure 1.19 indicates, ssDNA structures are somewhat unpredictable in their translocation properties. In addition to the high degree of intramolecular interactions resulting in secondary, tertiary and even quaternary structure, the persistence length of ssDNA is on the order of a single nanometre (~100x less than that of dsDNA), which meant that it was very unlikely that a ssDNA scaffold would translocate in a linear fashion through a nanopore large enough to accommodate protein-antibody complexes. The solutions to these issues were, quite naturally, to perform nanopore experiments in conditions that were closer to physiological, and to ensure that any DNA molecules used as scaffolds were double-stranded.

The mid-2010s brought on a flurry of extremely high impact publications that exploited these ideas. The Keyser group from the University of Cambridge in particular were not only able to produce yes-or-no signals out of antibodies bound to DNA scaffolds,[58] but to introduce a barcode-like sequence of molecular features on one half of a scaffold to uniquely identify which of a panel of biomarkers was bound on the other

half.[59] This proof-of-principle multiplexed protein detection that had eluded the field for so long was made possible by a molecular assembly strategy that was loosely based on the principles of DNA origami.[60] Rather than binding oligonucleotide sequences at only specific locations as we had originally envisioned in the Plan, the entire ~7 kbp ssDNA scaffold was annealed with hundreds of shorter, complementary sequences. While the sole purpose of many of these "tiling" strands was to render the scaffold double-stranded for improved behaviour during nanopore sensing, some were designed to provide a sequence of hairpin structures that served as either bits to be read like a barcode using the nanopore or as functional sites for protein or antibody binding.

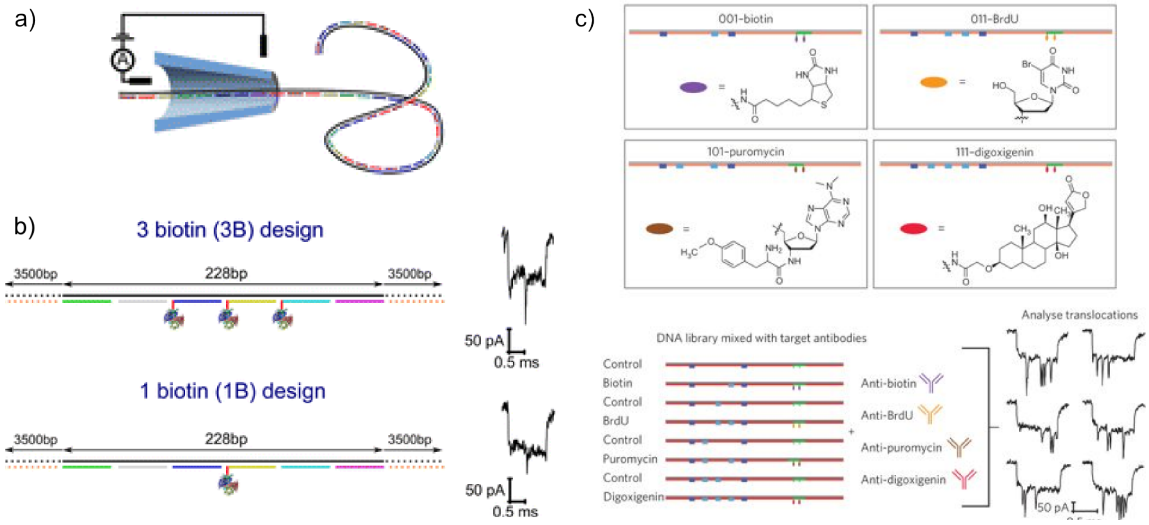

Figure 1.21 Multiplexed protein detection with glass nanopipettes.

a) Schematic of a ssDNA scaffold fully hybridized with short oligonucleotides translocating through a glass nanopipette. b) Specific oligonucleotides functionalised with biotin allow for binding different numbers of avidin proteins. Corresponding ionic current traces show a sublevel within events corresponding to the bound proteins.[58] c) An extension of the work in (a) dedicates one region of the scaffold to sequences of DNA hairpins that serve as a molecular barcode, and another region to the binding an antibody of interest. Nanopore analysis of barcode regions identify to which antibody a scaffold corresponds, and the presence of that antibody is determined by the detection of an additional sublevel in the sensing portion of translocation events.[59] Images adapted from the indicated references.

Variations of this scheme have since been used for a wide range of biomarker detection applications by the Keyser group alone, including the quantification of nanomolar protein concentrations,[61] the detection of single-nucleotide differences in DNA sequences via strand displacement reactions,[62] and genome profiling using a base-modifying enzyme that recognised specific motifs in DNA sequences.[63] Particularly advantageous for this approach was the use of glass nanopipettes which provided both an ease of fabrication for the generation of devices containing many pores for a high sensing yield and a geometry that produced extended electrical fields that pre-stretched molecules for sensing.

Another reported example of multiplexed protein detection using glass nanopipettes is shown in Figure 1.22, where the ssDNA scaffold and hundreds of tiling oligonucleotide sequences in Figure 1.21 were substituted with λ-phage dsDNA 48.5 kbp in length containing ssDNA overhangs at each end for functionalisation.[64] This example was particularly impressive because it replaced the well-characterised and high-binding affinity sites for conjugating proof-of-concept proteins with aptamers (ssDNA sequences that interact with a high degree of specificity with analytes in a manner similar to antibodies) that bound biologically relevant targets (thrombin and an acetylcholine regulator enzyme) in human serum. This work also profited from an approach presented in all subsequent chapters of this thesis in which short ssDNA segments can be extended by hybridising a complementary oligonucleotide that, itself, has a free ssDNA overhang for subsequent extension or functionalisation.

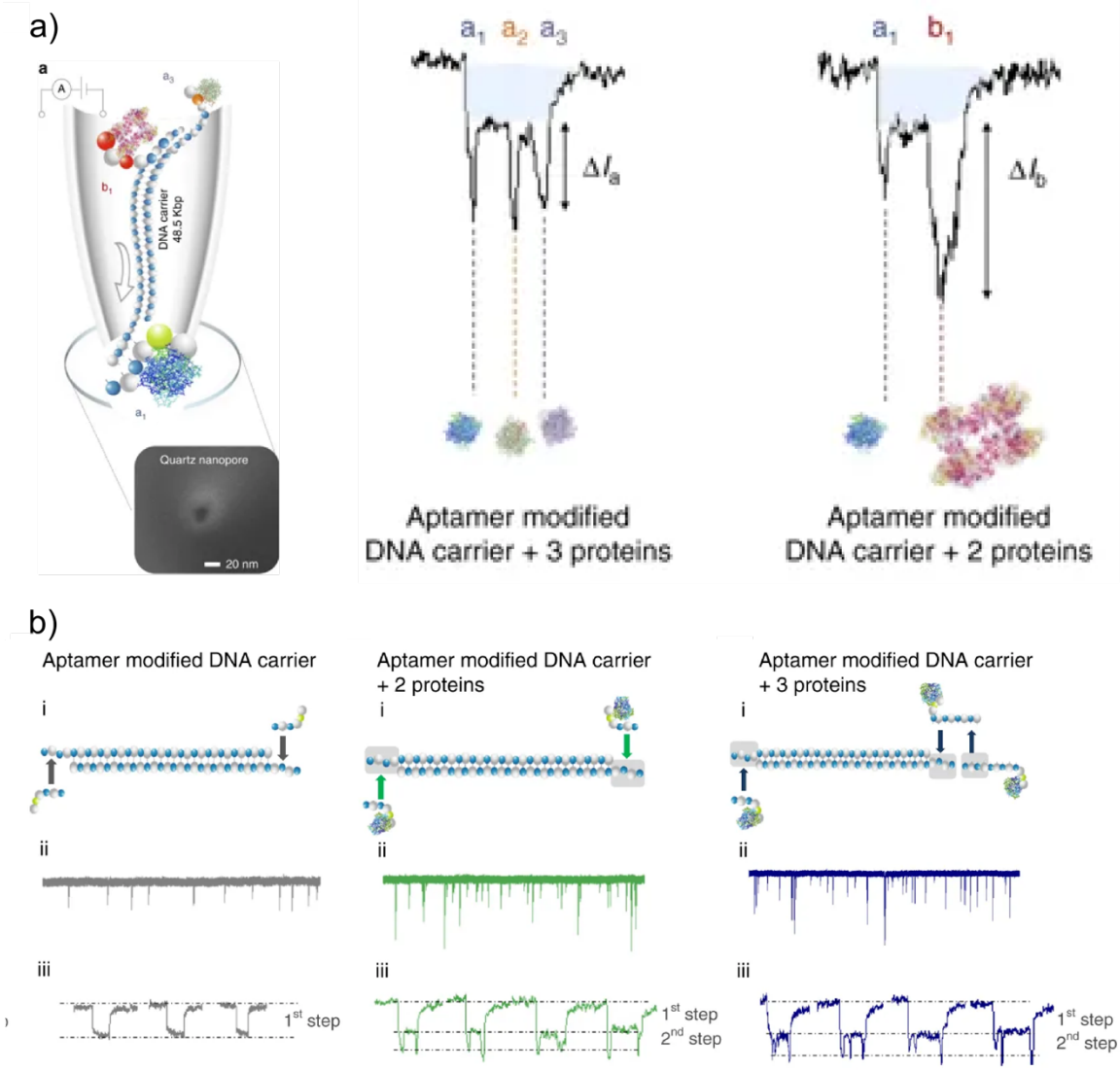

Figure 1.22 Aptamer-based multiplexed protein detection with glass nanopipettes.

a) Schematic of λ-phage DNA modified to incorporate three aptamer sequences for protein binding, with associated ionic current traces used for multiplexed detection using glass nanopipettes. b) Schematic illustrations of molecular assembly and associated ionic current recordings show various opportunities for functionalisation, including further extension of a free ssDNA overhang with additional functional oligonucleotides (right). Image adapted from reference 63.

The relatively reduced sensitivity of glass nanopipettes compared to ultra-thin membranes may at first glance seem to be a drawback for reading spatially dense information stored along a single molecule. It is possible, however, that this same

property minimised the problematic effects of clogging and allowed for the detection of only pertinent molecular information, rather than producing overly complicated ionic current signatures that would hinder analysis. Due to a combination of the potential for this being an issue for our highly sensitive nanopores fabricated by CBD in thin solid-state membranes and the fact that proof-of-principle experiments with very similar schemes to ours had been reported, our work shifted focus in 2015 from the Plan presented in Figure 1.16.

1.4 Thesis overview

Broadly speaking, the work presented in the next three chapters have two major themes in common: the design of nanopore-based sensing assays that consist of ionic current signals produced exclusively from the translocation of nucleic acids, and the amplification of signals produced by small targets to those that are readily measured by a solid-state nanopore. The former element effectively precluded the issues of nanopore clogging and overly complicated signatures for analysis caused by sticky and sensitive proteins, while still providing useful information. This also allowed us to operate in high salt regimes that provided optimal nanopore performance. On one hand, this involved significantly revising our schemes for analyte detection. On the other hand, this must be, by far, the most fun aspect of graduate research.

Of the next three chapters, Chapter 2 presents work that most closely resembles the Plan that we had set out to achieve in that it involves sensing a long ssDNA scaffold to which binding sites are added via hybridisation of complementary sequences. It is also reflective of the pseudo-DNA origami approach presented in Section 1.3.5 where

hundreds of ssDNA oligomers were used to pacify the scaffold for nanopore sensing while still maintaining functional binding sites. Rather than directly detecting protein analytes, however, our target of choice was a segment of ssDNA whose sequence has been demonstrated to be a biomarker for detecting the presence of the Zika virus. While this biomarker was too small to be specifically detected given current state of solid-state of nanopore sensing technologies, our approach was to translate the presence of this relatively short molecule to a large configurational change in scaffold topology from linear to looped. This *DNA nanoswitch* approach not only allowed us to detect the presence of the Zika gene segment, but also to quantify its concentration through measurement of the relative ratio of looped to linear scaffold molecules.

Despite nanoswitches being ideally suited to relatively low-bandwidth ionic current recordings due their inherent signal amplification, the underlying premise behind the change in topology presented limitations in terms of a biosensing assay. While the dynamic range spanned orders of magnitude in target concentration, there was a ceiling of reactant concentrations that could be practically studied due to the kinetics of intramolecular binding. Additionally, the high molar mass of the scaffold corresponding to over 7 kbp of dsDNA limited experiments to relatively low molar concentrations and large nanopores. Chapter 3, on the other hand, presents work in which significantly smaller scaffolds (~150-250 bp) were generated from overlapping, complementary sequences of ssDNA. Branching points along the scaffolds were optionally designed to produce zero, one or two dsDNA protrusions which were distinguishable with our sensing platform. We then performed an assay in which, only in the presence of ATP, a DNA displacement reaction occurred in which an ATP-binding aptamer would undergo

a configurational change to expose a ssDNA region and allow for the formation of a protrusion along a short scaffold. This provided indirect detection of ATP, a molecule that was otherwise considerably too small to be sensed directly by a solid-state nanopore.

In addition to the labour- and cost-efficiency of synthesising shorter scaffolds, higher capture rates are also typically observed for smaller molecules, which accelerates the acquisition of statistics from nanopore measurements. The tradeoff, however, is that small molecules are less reliably detected due to short translocation times and electronic bandwidth limitations. This was observed in measurements of protrusions along scaffolds in Chapter 3, where only the presence of ATP, rather than its actual concentration, was determinable as a yes-or-no statistical response following a high number of translocation events. More desirable would be the ability to provide an unambiguous measurement of every single-molecule translocation event to directly measure, for instance, the concentration of a target analyte.

Chapter 4 presents work in which the ability of large nanoswitches to be definitively assigned on a per-event basis was combined with the advantages of sensing short scaffolds. Rather than relying on the notoriously challenging detection of small features along individual scaffolds, this assay relied on the conjugation of two separate DNA structures via a target molecule of interest. In these experiments, three sets of molecular probes were designed, each consisting of two structurally equivalent molecules such that each set would appear as a single population of event signatures upon nanopore sensing in the absence of the target. For each target ssDNA molecule added to a sample, two probes would be consumed, yielding a reduction in counts of ionic current signatures associated with probes and a correlated increase in those corresponding to branched

complexes containing a target. Each probe set contained binding sites complementary to one half of a specific sequence of circulating microRNA (miRNA) of which elevated serum concentrations have been linked to the presence of various cancers in humans. In this study, we examined the dose response of our assay for determining the concentration of miRNA-155 using linear 98 bp probe sets, ultimately distinguishing six gradations of miRNA concentration within a single order of magnitude in minutes using solid-state nanopores.

Chapter II.

Programmable DNA Nanoswitch Sensing with Solid-State Nanopores

2.0 Abstract

Current techniques for determining molecular topology require sophisticated experimental setups or a large amount of sample together with the surrounding equipment necessary for optical measurements. In this work, we explore the performance of solid-state nanopores for sensing the conformational states of molecular nanoswitches assembled using the principles of DNA origami. These programmable single-molecule switches show great potential in molecular diagnostics and long-term information storage. We investigate the translocation properties of linear and looped nanoswitch topologies using nanopores fabricated in thin mem-branes, ultimately comparing the performance of our nanopore platform for detecting the presence of a Zika virus gene with that of conventional gel electrophoresis. We found that our system provides a high-throughput method for quantifying several target concentrations within an order of magnitude by sensing only several hundred molecules using electronics of moderate bandwidth that are conventionally used in nanopore sensing systems

2.1 Main

2.1.1 Introduction

The ability of DNA to self-assemble in specifically designed structures[60] has made it increasingly popular as a nanomaterial used in a host of biosensor,[65] nanoelectronic[66] and drug delivery systems.[67] DNA nanoswitches in particular have shown tremendous promise as a means of long-lasting,[68] highly dense[69] information storage, even exhibiting rewritable memory[70] and encryption capabilities.[71] Utilizing programmable, interaction-triggered changes in molecular conformation, DNA nanoswitches also offer a means of precisely quantifying a variety of molecular biomarkers[72,73] through measurement of the relative stoichiometries of different molecular topologies. A major advantage of this approach is the ability to translate the input of a relatively small target such as a short sequence of single-stranded (ss) DNA to a large output corresponding to the reconfiguration of a molecule that is hundreds of times longer than the target.

As such, a variety of molecular conformation readout methods have been explored in recent years, including surface-enhanced Raman spectroscopy (SERS), electrochemical signalling and atomic force microscopy (AFM).[74] Among fluorescence-based techniques for determining molecular conformation, gel electrophoresis provides a low-cost, simple approach that is readily accessible to many laboratory and commercial settings.[72,75] While sensitive to biologically relevant (pico- to nanomolar) analyte concentrations, such systems arguably require a high degree of user experience for

reproducibility and require sufficient sample material (tens of ng) and surrounding equipment for bulk optical measurements.

Nanopore sensors provide an attractive alternative to fluorescence-based methods for high-throughput readouts of DNA conformation.[13] Relying on the Coulter principle, ionic current blockades produced as biomolecules such as DNA and proteins translocate through these nanoscale apertures provide highly precise measurements of location-specific molecular size.[58,76] Nanopore platforms presents several advantages, including ready integration in lab-on-a-chip systems[77,78] and the ability to perform readouts of molecular topology on a single-molecule basis. In fact, nanopore sensors have emerged as one of the most promising tools for next-generation molecular diagnostic and analytic applications.[2,11,79]

The concurrent rise in popularity of DNA origami-based nanostructures and nanopore sensing has led to some very exciting experimental research marrying both platforms in recent years. For instance, DNA barcodes with customizable binding sites have provided nanopore-based multiplexed detection of a variety of biomolecular targets.[58,62,64] In part due to the relative ease of fabrication, the majority of such studies have utilized glass nanopipettes as the means of providing electrical readouts. Nanopores fabricated in thin membranes, on the other hand have only recently been democratized for widespread use through fabrication and conditioning methods of controlled breakdown (CBD) with high electric fields.[24,44] The performance of these nanopores for sensing DNA origami structures is thus less understood.

In this work, we explore the performance of nanopores fabricated in thin (~10 nm thick) silicon nitride (SiN) membranes using CBD for the analysis of DNA origami-based

nanoswitch structures. In particular, we investigate the translocation properties of nanoswitches in "on" (looped) and "off" (linear) states using a ssDNA target whose sequence has shown promise as a biomarker to detect the presence of Zika virus in biological samples.[80] We additionally explore the ability of our system to quantify the Zika gene biomarker over a range of experimental concentrations, finding that our nanopore system provides comparable results with state-of-the-art gel electrophoresis, but with significantly fewer molecules required for quantification.

2.1.2 Results and Discussion

The principle behind the nanoswitch assay is schematically shown in Figure 2.1. As is common with most DNA origami applications, linearized single-stranded (ss) M13mp18 phage DNA was incubated with short (39-base) complementary oligonucleotides (tiles). For the purposes of this assay, tile sequences were such that they produced a fully hybridized double-stranded (ds) DNA scaffold ~7.2 kbp in length (Figure 2.1a), with two of the tiles providing free ssDNA overhangs (binding sites) approximately one third of the total length away from each end of the scaffold. Binding sites were designed to be complementary to two different ends of a ssDNA target of interest, in this case a 50-base portion of the NS5 gene of the Zika virus. When fully hybridized with the NS5 gene target, the scaffold underwent a topological transformation from linear to looped, as shown in Figure 2.1b. Gel characterization of this conformational change is shown in Figure 2.1c, where looped scaffolds exhibit a lower degree of electrophoretic mobility in agarose gels than linear molecules of the same total fragment length.

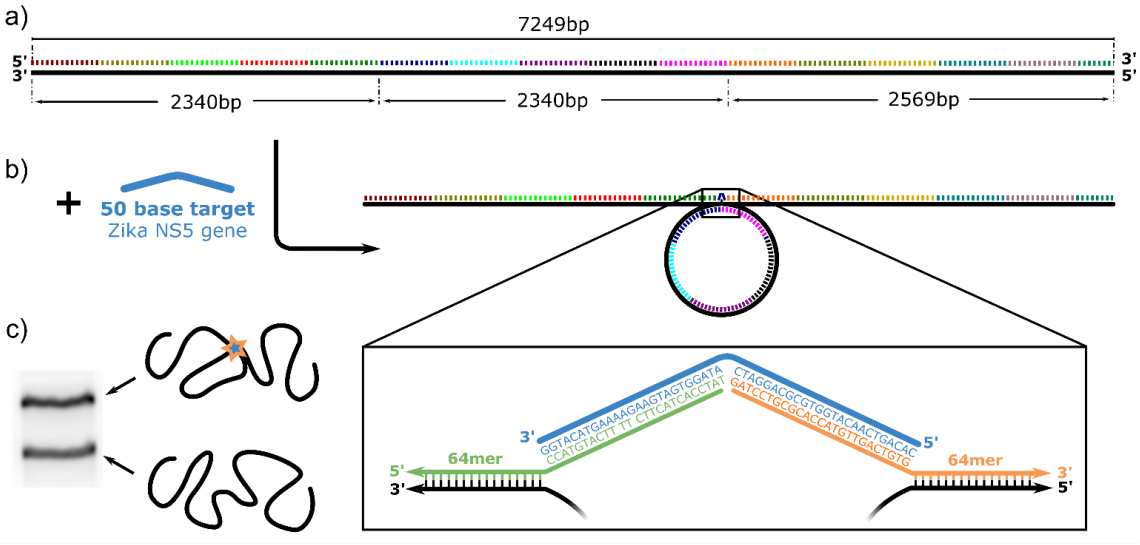

Figure 2.1. Schematic representation of nanoswitch assembly.

a) Linearized single-stranded M13mp18 phage DNA scaffold is hybridized with 186 complementary oligonucleotide tile strands 39 bases in length. Two of the tile strands located at one third intervals along the scaffold contain overhanging sequences (orange and green) complementary to a portion of the Zika NS5 gene (blue). b) Hybridization with the target sequence results in reconfiguration of the scaffold from a linear to looped configuration. c) 1 % agarose gel characterization of a sample mixture containing 40 ng of 2 nM scaffold incubated with 10 nM Zika gene target shows two bands corresponding to looped (top) and linear (bottom) molecular configurations.

In order to develop a nanopore-based assay for counting stoichiometric ratios of switches in the on- and off-states, and thus quantify the concentration of the NS5 Zika gene biomarker, nanoswitch structures required careful design such that ionic current signatures of looped molecules would be differentiable from linear scaffolds that can translocate in linear or folded states. This was achieved by positioning the binding sites at one third intervals along the scaffold. Any translocating looped molecule would thus, at some point during translocation, have at least three segments of dsDNA ~1.1 kbp in length in the nanopore sensing volume. With an observed translocation rate of ~ 40 μs/kbp (Section 2.3.4), this corresponds to a transit time that is within the bandwidth of

the electronics used in this study (500 kHz sampling rate low-pass Bessel filtered at 100 kHz). Such ionic current signatures should be readily differentiable from those corresponding to linear molecules which have been well characterized as fully translocating, in the vast majority of cases, in either a single-file or folded fashion where a maximum of two double helices (d_{dsDNA} = 2.2 nm) occupy the nanopore sensing volume at any given time.

Figure 2.2 highlights the effectiveness of this molecular design for distinguishing linear scaffolds from nanoswitches looped via the NS5 biomarker. The first 50 translocation events from an experiment in which the assembled dsDNA scaffold in the absence of the target gene are concatenated in Figure 2.2a. As expected for a linear polymer of this length, the majority of events exhibit ionic current blockages that fall within two blockage states corresponding to translocation in either a linear unfolded (ΔI_1) or single-fold (ΔI_2) conformations. Indeed, the histogram in Figure 2.2a of the deepest blockage state within each event fit with our analysis algorithm (ΔI_{max}) over the entire experimental recording time shows that ~90 % of events fall within two populations that are < 3.5 nA of blocked ionic current (red and yellow bands *1* and *2*, respectively, in Figure 2.2). The sample in Figure 2.1c containing excess NS5 gene, on the other hand, show a majority of events with a blockage state $\Delta I_{n>2}$ corresponding to at least three molecular segments of dsDNA occupying the pore at some point during translocation (Figure 2.2b). In other words, the fitted level that deviated the furthest from baseline in these events was greater than that corresponding to the translocation of folded but unlooped dsDNA.

Event types were assigned based on the sequence of ionic current blockage states detected by our analysis algorithm, as previously described.[81] Numbers within an event type indicate the number of dsDNA segments detected within the pore as unique blockage states are detected during a translocation event (*i.e.* type *21* means two segments were detected in the pore at the beginning of an event followed by a single segment at the end of the event). Representative ionic current traces are shown in Figure 2.2c alongside the interpreted molecular configuration upon translocation, where green traces corresponding to single-file and folded scaffold signatures (types *1* and *21*, respectively) of the unlooped nanoswitch from Figure 2.2a are shown in comparison to those corresponding to looped nanoswitches (blue). Among the latter event types, those of type *131*, where a single end of the scaffold enters the nanopore in a linear fashion followed by the loop and elongated trailing end of the nanoswitch, were the most frequently observed at ~18 % of blockage states $\Delta I_{n>2}$.

As might be expected for polymers of this length, looped topologies were more often observed as entering the nanopore folded somewhere along one linear extremity of the nanoswitch (*i.e.* in a folded fashion from one of the nanoswitch ends). Depending on where an extremity is first captured by the nanopore and how much the folded segment overlapped with the rest of the nanoswitch structure, various event types were observed. The three such translocation signatures (event types *2131*, *2431* and *2421*) are shown in Figure 2.2c account for ~19% of all events with $\Delta I_{n>2}$. For a complete breakdown of event type statistics, please refer to Section 2.3.5.

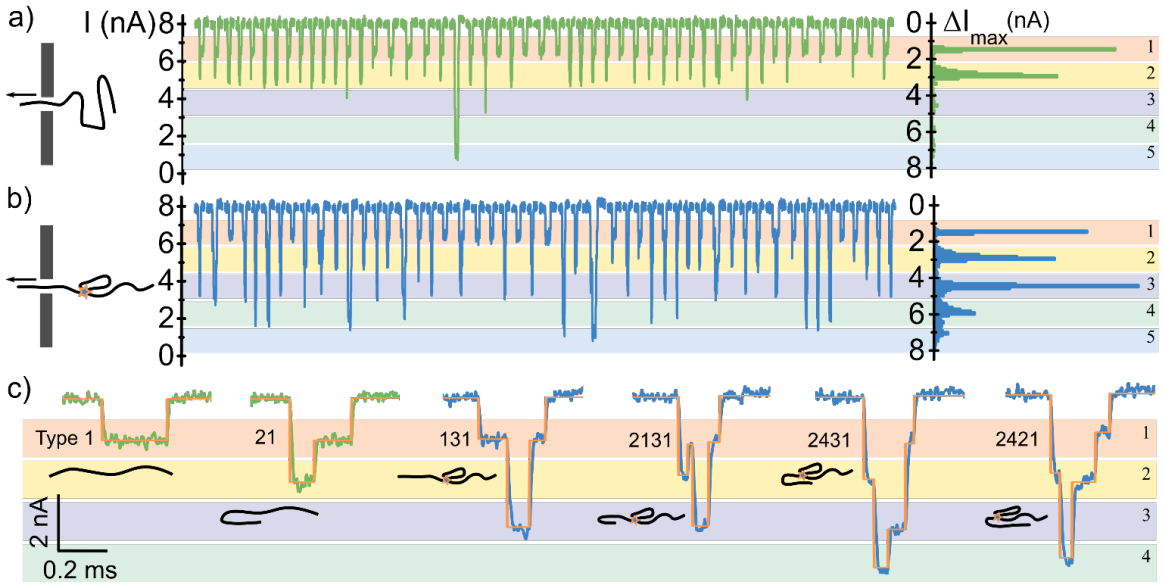

Figure 2.2. Translocation properties of linear and looped nanoswitches.

a) Concatenated ionic current traces of the first 50 events detected as linear scaffolds were sensed using a nanopore. A histogram of the fitted ionic current level that deviated the most from baseline within each event over the entire experiment shows two populations for linear scaffolds (ΔI_{max} in state 1 or 2). b) Looped nanoswitches show a significantly higher number of events with a blockage state greater than 2 due to the presence of at least three dsDNA strands in the nanopore sensing volume at some point during translocation. c) The order of blockage states (event types) observed within each event indicate how many strands of dsDNA occupy the nanopore volume at any time during translocation, allowing for interpretation of molecular configuration. Representative traces with the interpreted molecular configuration of scaffolds in the absence of target (green) show linear (type 1) and folded (type 21) translocation events. Blue traces show the most common event types observed for looped nanoswitches, where a maximum blockage depth corresponding to states 3 or 4 were observed depending on where the molecule was first captured by the nanopore. Samples are those presented in Figure 2.1c diluted 1:1 in 3.6 M LiCl buffered with HEPES to pH 8.0 and subjected to a 200 mV bias across a 6.5 nm pore with an effective thickness of 7.4 nm. Ionic current traces were acquired with a sampling rate of 500 kHz low-pass Bessel filtered at 100 kHz.

Having established a basis for identifying looped nanoswitch structures (*i.e.* exhibiting a blockage state of $\Delta I_{n>2}$ when scaffolds were intramolecularly hybridized with an ssDNA target), we then set out to assess the ability of our solid-state nanopores for quantifying the concentration of NS5 biomarker in a sample mixture. Figure 2.3a

illustrates a typical agarose gel electrophoresis experiment in which nanoswitch scaffolds were incubated with an increasing amount of the ssDNA target from left to right. As expected, a band of lower mobility molecules corresponding to looped nanoswitches increased in intensity relative to the one associated with linear scaffolds (40 ng, 2 nM) as the molar concentration of target was increased from 0 nM (the control case) to 10 nM. While higher concentrations of target were incubated with the scaffold concentration presented, saturation of binding sites inhibited loop formation at target concentrations > 10 nM (Section 2.2.3).

These samples were then sensed using our nanopore platform, with histograms of ΔI_{max} for each sample translocating through the same nanopore shown in Figure 2.3b. As expected from gel characterization of these samples in Figure 2.3a, populations corresponding to looped molecules with blockage states $\Delta I_{n>2}$ appear in increasing number as the concentration of the NS5 target is increased. In order to account for small variations in peak depths due to slight differences in ionic strength and open pore baselines between samples, here we define $\Delta I_{n>2}$ events as those with ΔI_{max} at least 4σ greater than the center of the ΔI_2 peak, where σ ~ 0.1 nA for the peaks in Figure 2.3b.

The percentage of $\Delta I_{n>2}$ is shown in Figure 2.3c for three different nanopores ranging in size from 6.5 nm to 7.7 nm that sensed the reaction mixtures shown in Figure 2.3a, with blue data points corresponding to the data shown in Figure 2.3b (from the same nanopore identified as NP23). While different nanopores show a small amount of variability in sensitivity for loop detection, the overall dose-response as determined by gel characterization was well captured in nanopore sensing experiments.

In addition to the concentration of target molecules, the amount of looped nanoswitches formed in a reaction depends on several factors, including the initial scaffold concentration and the concentration of scaffolds relative to targets.[72] To compare the performance our nanopore platform with that of gel electrophoresis between reactions with a variable amount of loop formation in different reaction conditions, Figure 2.3d shows the percentage of translocation events with $\Delta I_{n>2}$ from nanopore recordings versus the relative intensity of looped structures in gels I_{gel} for all samples studied. We found that nanopore results generally agreed with gel measurements, with the dashed line in Figure 2.3d indicating perfect 1:1 agreement between the two methods. We found that while nanopore measurements tended to provide fewer relative counts of looped nanoswitches compared to a gel in samples with a high degree of loop formation, they also showed approximately 5 to 15 % more of such events than a gel for samples containing low loop fractions.

To investigate the source of this variation, we studied in more detail the translocation characteristics of assembled nanoswitches without the presence of the target. We found that assembled scaffold molecules, which contain hundreds of nicks in the helical structure and a high likelihood of one or more gaps due to missing tiles, provided a higher rate of $\Delta I_{n>2}$ events than unnicked dsDNA fragments of comparable length when translocating through the same nanopore (Section 2.2.4). Therefore, the higher rate of false positives detected by the nanopore in Figure 2.3d might then be explained by a higher sensitivity to molecular flexibility compared to gel electrophoresis, which showed fewer non-linear scaffold topologies (or none) at very low target concentrations.

In order to understand why nanopores exhibited fewer counts of looped molecules than gels at high loop fractions, we also explored other metrics of nanopore analysis. One example is the maximum deviation in ionic current from baseline (the single ionic current data point that differed the most from the open pore value),[82] rather than simply the deepest fitted level, which could have underestimated looped counts if our system was bandwidth-limited. However, we found that the results presented in Figure 2.3 were relatively unaffected (typically < 3 % difference) using this criterion (Section 2.2.4). This highlights the advantage of the signal amplification characteristic of nanoswitch-based target detection. While small targets bound to DNA scaffolds can result in ionic current signatures too short to be sensed using conventional nanopore systems, the topological change of the large scaffold resulting from a nanoswitch association reaction is detectable at even at moderate sampling rates without being bandwidth-limited. Discrepancies in Figure 2.3d are thus more likely due to error in gel quantification which, in addition to requiring several nanograms of DNA for detection and potentially skewing the relative ratios of different species, can be prone to a high degree of variability from different imaging conditions and algorithms used in fluorescence analysis.

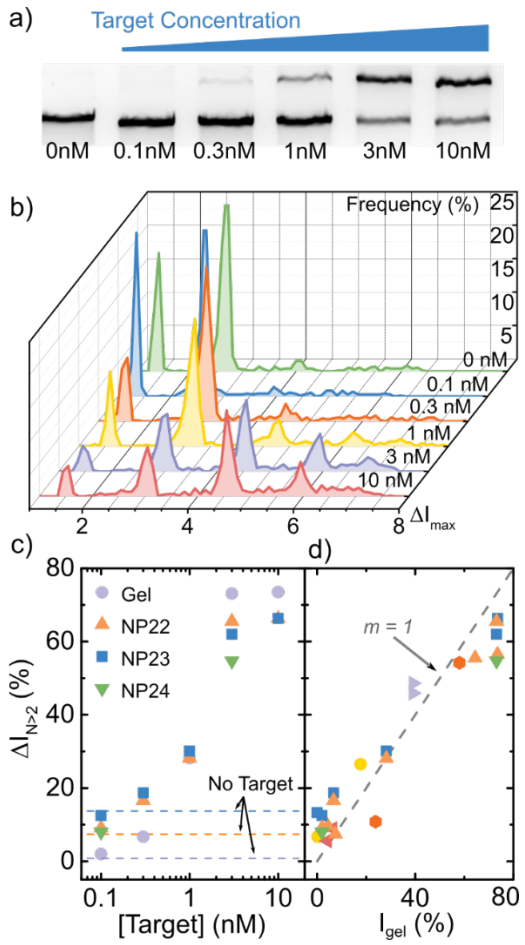

Figure 2.3. Dose response of nanoswitch formation in gels and nanopore measurements.

a) 1 % agarose gel characterization in which 2 nM scaffold molecules (40 ng) were incubated with increasing amounts of the Zika gene target, from left to right. A band corresponding to lower-mobility looped molecules became increasingly pronounced as the target concentration was increased. b) Nanopore characterization of the maximum blockage state fitted within each event for each sample presented in a) shows increasing populations of events with $\Delta I_{n>2}$*. c) The percentage of events with* $\Delta I_{max} > \Delta I_{n>2} = \Delta I_2 + 4\sigma$ *for three different nanopores that sensed the samples from a) show a sigmoidal increase in detected looped topologies alongside the number of looped configurations quantified by gel electrophoresis. Dashed lines indicate* $\Delta I_{n>2}$ *fractions when no target was added. d) A comparison of the percentage of looped topologies as determined by nanopore (y-axis) versus gel (x-axis) for all sample reactions performed under various experimental conditions show a good agreement of between both platforms. Scatter plot symbols correspond to the nanopore on which a particular sample was sensed, with orange, blue and green symbols corresponding to the samples and nanopores presented in c).*

Our digital approach for reading nanoswitch topology was further characterized in Figure 2.4, where the mean amount N^*/N of translocation events exhibiting $\Delta I_{n>2}$ during an experiment for selected samples from Figure 2.3b is shown as a function of the running total number of events detected N. Confidence intervals corresponding to a p-value of 0.05 are shown as coloured regions around each mean.[83] While the 0.1 nM target sample was not statistically different from the 0 nM, nor 3 nM from the 10 nM sample, the vertical dashed line at $N = 500$ indicates the approximate location where all samples in the range of 0.3 nM to 3 nM were distinguishable with 95 % confidence both from each other and from the control case where no target was added.

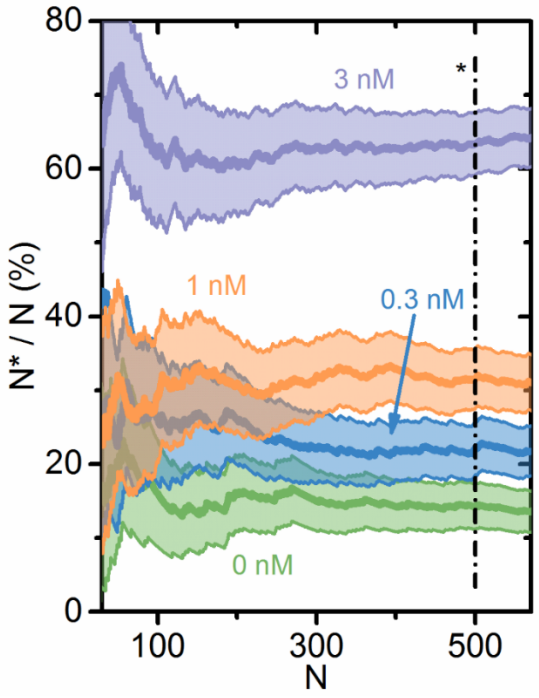

Figure 2.4. Statistical analysis of nanoswitch quantification.

The percentage of translocation events exhibiting $\Delta I_{n>2}$, with confidence intervals associated with $p = 0.05$ (shaded colours surrounding the mean), show that < 500 events (dashed line) are required before selected samples from Figure 2.3 can be distinguished using a nanopore with 95 % confidence.

2.1.3 Conclusions

The signal amplification inherent in fluorescence quantification of DNA nanoswitches, enables state-of-the art gel analysis to detect as few as attomoles of molecules (~10^6 nanoswitches corresponding to ~ 1 picogram of 7.2 kbp dsDNA). Our nanopore platform, on the other hand, was able to distinguish four different samples spanning an order of magnitude of target concentration in counting fewer than 500 individual molecules. For the experiments shown in Figures 2.3 and 2.4, the dynamic range of the assay was limited by the initial scaffold concentration (2 nM) as well as the inherent ~ 30 nM ceiling for assay components above which saturation of binding sites and inter-scaffold hybridization impede loop formation.[72] However, this range could be broadened using lower scaffold concentrations. While this would result in longer experiment times to acquire sufficient statistics, the use of higher voltages and different ionic solutions such as KCl in conjunction with higher bandwidth electronics, as well as recently investigated techniques such as control of electro-osmotic[84] and fluid flow in confined device geometries[85] with asymmetric salt gradients,[31] could provide a combined ~10^2 to 10^3-fold capture rate enhancement. This would allow for nanopore sensing of low picomolar nanoswitch concentrations in minutes using our sensing scheme, ultimately providing ~1-10 pM target detection as a lower bound based on the specificity of our sensor (requiring ~ 20 % loop formation) and a comparison with gel intensities in previous work.[72,75] In addition to a providing means of reading molecularly encoded information at low copy numbers, this nanopore-based approach to nanoswitch topology detection could also be extended to quantifying other diagnostically relevant biomarkers such as proteins, antibodies and circulating microRNA.

2.2 Experimental Methods

2.2.1 Sample preparation

All nucleotide sequences were purchased from Integrated DNA Technologies (IDT) and shipped in Matrix well plates at 100 μM in TE buffered to pH 8.0, with sequences in Section 2.2.1. Scaffolds were prepared by first linearizing circular M13mp18 ssDNA (New England Biolabs N4040). Briefly, 10-20x excess of a 40-base oligonucleotide sequence complementary to the to the restriction site was annealed with the circular scaffold by heating to 70 ºC and cooling to 37 ºC at -0.5 ºC/min in the manufacturer recommended reaction conditions for HincII restriction (New England Biolabs R0103). HincII was then added to the sample mixture and incubated at 37 ºC for 1 hr before heat inactivation at 65 ºC for 20 minutes.

A typical reaction linearized ~ 10 μg of M13mp18 in a total volume of 80 μL (including 10 μL of HincII enzyme) in 1x NEBuffer 3.1 (supplied with the enzyme). Linearized scaffolds were then annealed with 3x excess of all tiles and binding site strands (premixed at ~ 540 nM each) by cooling from 75 ºC to 5 ºC at -0.2 ºC/min in a thermocycler. Scaffolds were purified and buffer-exchanged to IDT's Duplex Buffer (30 mM HEPES, pH 7.5; 100 mM potassium acetate) using Amicon Ultra-0.5 mL 100 kDa molecular weight purification filters (Sigma-Aldrich UFC510096). Scaffolds concentrations were determined with a spectrophotometer (Bioteck Epoch 2, 260 nm absorption) prior to incubation with the Zika gene target sequence (at least 2 hr at room temperature) at the concentrations indicated in Section 2.2.2. Following scaffold purification, all sample solutions were supplemented with 5 mM Mg^{2+} for dsDNA

stabilization and stored at 4 ºC for up to several days without any noticeable change in nanoswitch yield. All samples were mixed with equal parts 3.6 M LiCl HEPES-buffered to pH 8.0 immediately prior to being sensed using a nanopore.

2.2.2 Gel characterization.

Nanoswitch yield was first characterized using 0.7 % - 1 % agarose gel electrophoresis in 1x TAE. Typical experiments consisted of 20 ng - 40 ng of total DNA with 1x DNA Loading Dye (Thermo Scientific R0611) and 1x GelRed (Biotium 41003) for a total sample volume of 15 µL. Gels were run on an ice bath for ~ 2 hr at 70 V prior to visualization using a FluorChem Q (Alpha Innotech) imager and quantification using GelBandFitter[86] as described in Section 2.2.3.

2.2.3 Nanopore fabrication.

Solid-state nanopores were fabricated in 10 nm thick (50 µm by 50 µm) SiN membrane windows (Norcada, part number NT005Z) using the CBD method.[24] 3D-printed cells housed intact membrane windows which separated 20 uL reservoir channels both fluidically and electrically. A voltage bias between reservoirs containing 1 M KCl pH 8.0 was ramped from 0 V – 12 V using Ag/AgCl electrodes while the leakage current through the membrane was monitored at 10 Hz using custom-written LabVIEW software. An abrupt increase in current exceeding 15 nA above the median value detected during the prior 5 s of recording indicated the presence of a nanopore and triggered automatic removal of the applied bias. Nanopores were typically formed at ~ 9 V and were < 3 nm in diameter under these conditions. Nanopore size was then tuned using alternating pulses of ± 4 V until the desired diameter was achieved.[44,45] The ionic solution was then

exchanged for 3.6 M LiCl and allowed to equilibrate for a minimum of 1 hour to allow for stabilization of the nanopore conductance. All solutions for nanopore fabrication, conditioning and stabilization were buffered at pH 8.0 using HEPES. A summary of nanopore geometries can be found in Section 2.2.2.

2.2.4 Data acquisition and analysis.

Ionic current traces for nanoswitch sensing experiments were acquired with an Axopatch 200B (Molecular Devices) interfaced with custom-written LabVIEW software. Molecular translocation experiments were performed at a sampling rate of 500 kHz and low-pass filtered at 100 kHz. Translocation events were analyzed without additional filtering using an adapted version of the CUSUM+ algorithm,[87,88] as described in Section 2.2.4.

2.3 Supporting Information

2.3.1 Molecular assembly.

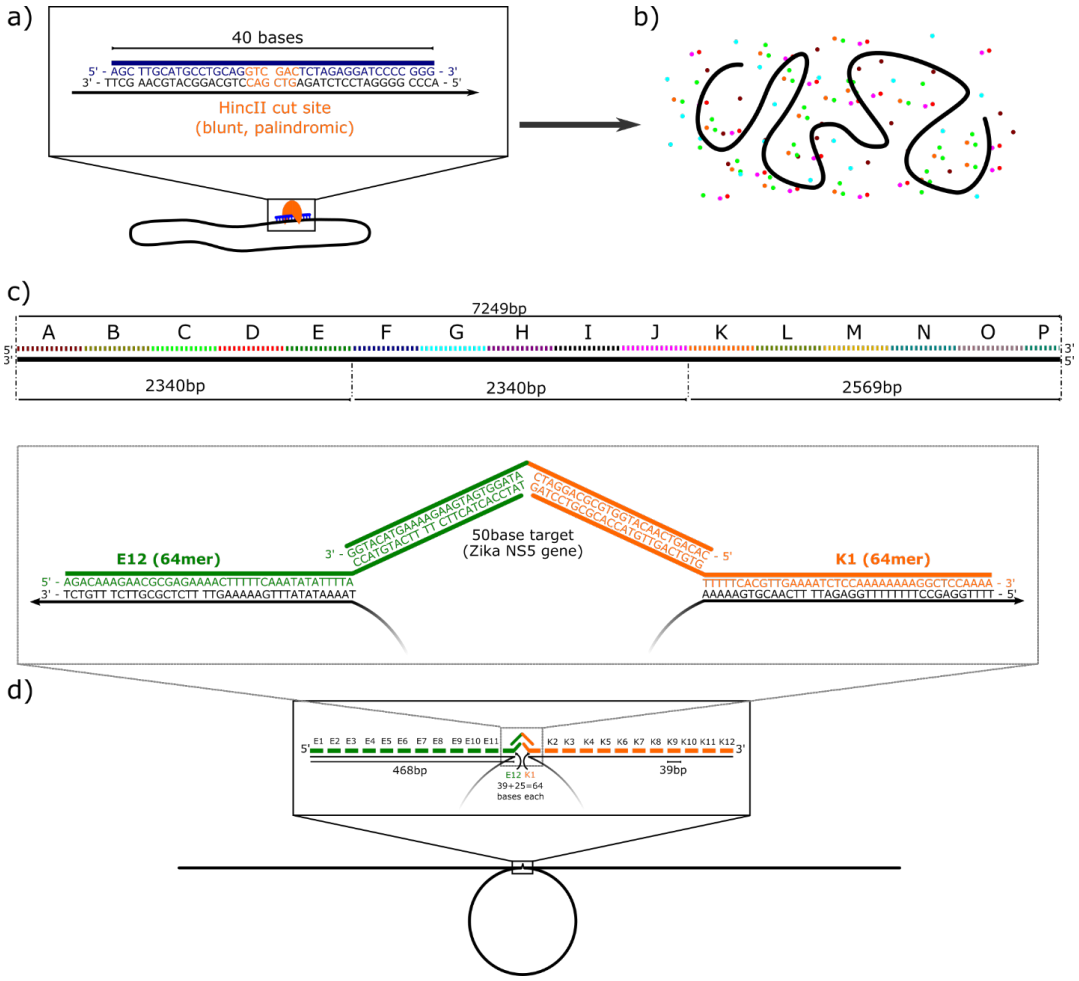

Figure 2.5. Schematic overview of nanoswitch assembly.

a) Circular M13mp18 ssDNA is linearized by first annealing a 40-base cutting primer (blue) complementary to the HincII restriction site. Following restriction, tile and binding site oligos were added to the single-stranded linear scaffold (b) to form a fully double-stranded DNA with binding sites extending the E12 and K1 tile strands (c). Following buffer exchange and purification (not shown), the 50-base segment of the NS5 gene of the Zika virus (bases 10254-10304)[80] was added, hybridizing to the 25-base ssDNA overhangs and causing a topological change in the nanoswitch from linear to looped (d). All tiles are 39 bases long with the exception of P5 (second from the right in (c), 34 bases), and the binding site strands which were 64 bases in length. All sequences are shown in Table 2.1.

Table 2.1. Oligonucleotide sequences used to form nanoswitches.

Name	Sequence (5'-3')	Length
Cutting primer	AGCTTGCATGCCTGCAGGTCGACTCTAGAGGATCCCCGGG	**40**
NS5 target	CACAGTCAACATGGTGCGCAGGATCATAGGTGATGAAGAAAAGT ACATGG	**50**
E12-BS	AGACAAAGAACGCGAGAAAACTTTTTCAAATATATTTTACCATGTAC TTTTCTTCATCACCTAT	**64**
K1-BS	GATCCTGCGCACCATGTTGACTGTGTTTTTCACGTTGAAAATCTCC AAAAAAAAGGCTCCAAAA	**64**
A1	GACTCTAGAGGATCCCCGGGTACCGAGCTCGAATTCGTA	39
A2	ATCATGGTCATAGCTGTTTCCTGTGTGAAATTGTTATCC	39
A3	GCTCACAATTCCACACAACATACGAGCCGGAAGCATAAA	39
A4	GTGTAAAGCCTGGGGTGCCTAATGAGTGAGCTAACTCAC	39
A5	ATTAATTGCGTTGCGCTCACTGCCCGCTTTCCAGTCGGG	39
A6	AAACCTGTCGTGCCAGCTGCATTAATGAATCGGCCAACG	39
A7	CGCGGGGAGAGGCGGTTTGCGTATTGGGCGCCAGGGTGG	39
A8	TTTTTCTTTTCACCAGTGAGACGGGCAACAGCTGATTGC	39
A9	CCTTCACCGCCTGGCCCTGAGAGAGTTGCAGCAAGCGGT	39
A10	CCACGCTGGTTTGCCCCAGCAGGCGAAAATCCTGTTTGA	39
A11	TGGTGGTTCCGAAATCGGCAAAATCCCTTATAAATCAAA	39
A12	AGAATAGCCCGAGATAGGGTTGAGTGTTGTTCCAGTTTG	39
B1	GAACAAGAGTCCACTATTAAAGAACGTGGACTCCAACGT	39
B2	CAAAGGGCGAAAAACCGTCTATCAGGGCGATGGCCCACT	39
B3	ACGTGAACCATCACCCAAATCAAGTTTTTTGGGGTCGAG	39
B4	GTGCCGTAAAGCACTAAATCGGAACCCTAAAGGGAGCCC	39
B5	CCGATTTAGAGCTTGACGGGGAAAGCCGGCGAACGTGGC	39
B6	GAGAAAGGAAGGGAAGAAAGCGAAAGGAGCGGGCGCTAG	39
B7	GGCGCTGGCAAGTGTAGCGGTCACGCTGCGCGTAACCAC	39
B8	CACACCCGCCGCGCTTAATGCGCCGCTACAGGGCGCGTA	39
B9	CTATGGTTGCTTTGACGAGCACGTATAACGTGCTTTCCT	39
B10	CGTTAGAATCAGAGCGGGAGCTAAACAGGAGGCCGATTA	39
B11	AAGGGATTTTAGACAGGAACGGTACGCCAGAATCCTGAG	39
B12	AAGTGTTTTTATAATCAGTGAGGCCACCGAGTAAAAGAG	39
C1	TCTGTCCATCACGCAAATTAACCGTTGTAGCAATACTTC	39
C2	TTTGATTAGTAATAACATCACTTGCCTGAGTAGAAGAAC	39
C3	TCAAACTATCGGCCTTGCTGGTAATATCCAGAACAATAT	39
C4	TACCGCCAGCCATTGCAACAGGAAAAACGCTCATGGAAA	39
C5	TACCTACATTTTGACGCTCAATCGTCTGAAATGGATTAT	39
C6	TTACATTGGCAGATTCACCAGTCACACGACCAGTAATAA	39
C7	AAGGGACATTCTGGCCAACAGAGATAGAACCCTTCTGAC	39
C8	CTGAAAGCGTAAGAATACGTGGCACAGACAATATTTTTG	39
C9	AATGGCTATTAGTCTTTAATGCGCGAACTGATAGCCCTA	39
C10	AAACATCGCCATTAAAAATACCGAACGAACCACCAGCAG	39
C11	AAGATAAAACAGAGGTGAGGCGGTCAGTATTAACACCGC	39
C12	CTGCAACAGTGCCACGCTGAGAGCCAGCAGCAAATGAAA	39
D1	AATCTAAAGCATCACCTTGCTGAACCTCAAATATCAAAC	39
D2	CCTCAATCAATATCTGGTCAGTTGGCAAATCAACAGTTG	39
D3	AAAGGAATTGAGGAAGGTTATCTAAAATATCTTTAGGAG	39
D4	CACTAACAACTAATAGATTAGAGCCGTCAATAGATAATA	39
D5	CATTTGAGGATTTAGAAGTATTAGACTTTACAAACAATT	39
D6	CGACAACTCGTATTAAATCCTTTGCCCGAACGTTATTAA	39
D7	TTTTAAAAGTTTGAGTAACATTATCATTTTGCGGAACAA	39

D8	AGAAACCACCAGAAGGAGCGGAATTATCATCATATTCCT	39
D9	GATTATCAGATGATGGCAATTCATCAATATAATCCTGAT	39
D10	TGTTTGGATTATACTTCTGAATAATGGAAGGGTTAGAAC	39
D11	CTACCATATCAAAATTATTTGCACGTAAAACAGAAATAA	39
D12	AGAAATTGCGTAGATTTTCAGGTTTAACGTCAGATGAAT	39
E1	ATACAGTAACAGTACCTTTTACATCGGGAGAAACAATAA	39
E2	CGGATTCGCCTGATTGCTTTGAATACCAAGTTACAAAAT	39
E3	CGCGCAGAGGCGAATTATTCATTTCAATTACCTGAGCAA	39
E4	AAGAAGATGATGAAACAAACATCAAGAAAACAAAATTAA	39
E5	TTACATTTAACAATTTCATTTGAATTACCTTTTTTAATG	39
E6	GAAACAGTACATAAATCAATATATGTGAGTGAATAACCT	39
E7	TGCTTCTGTAAATCGTCGCTATTAATTAATTTTCCCTTA	39
E8	GAATCCTTGAAAACATAGCGATAGCTTAGATTAAGACGC	39
E9	TGAGAAGAGTCAATAGTGAATTTATCAAAATCATAGGTC	39
E10	TGAGAGACTACCTTTTTAACCTCCGGCTTAGGTTGGGTT	39
E11	ATATAACTATATGTAAATGCTGATGCAAATCCAATCGCA	39
E12	AGACAAAGAACGCGAGAAAACTTTTTCAAATATATTTTA	39
F1	GTTAATTTCATCTTCTGACCTAAATTTAATGGTTTGAAA	39
F2	TACCGACCGTGTGATAAATAAGGCGTTAAATAAGAATAA	39
F3	ACACCGGAATCATAATTACTAGAAAAAGCCTGTTTAGTA	39
F4	TCATATGCGTTATACAAATTCTTACCAGTATAAAGCCAA	39
F5	CGCTCAACAGTAGGGCTTAATTGAGAATCGCCATATTTA	39
F6	ACAACGCCAACATGTAATTTAGGCAGAGGCATTTTCGAG	39
F7	CCAGTAATAAGAGAATATAAAGTACCGACAAAAGGTAAA	39
F8	GTAATTCTGTCCAGACGACGACAATAAACAACATGTTCA	39
F9	GCTAATGCAGAACGCGCCTGTTTATCAACAATAGATAAG	39
F10	TCCTGAACAAGAAAAATAATATCCCATCCTAATTTACGA	39
F11	GCATGTAGAAACCAATCAATAATCGGCTGTCTTTCCTTA	39
F12	TCATTCCAAGAACGGGTATTAAACCAAGTACCGCACTCA	39
G1	TCGAGAACAAGCAAGCCGTTTTTATTTTCATCGTAGGAA	39
G2	TCATTACCGCGCCCAATAGCAAGCAAATCAGATATAGAA	39
G3	GGCTTATCCGGTATTCTAAGAACGCGAGGCGTTTTAGCG	39
G4	AACCTCCCGACTTGCGGGAGGTTTTGAAGCCTTAAATCA	39
G5	AGATTAGTTGCTATTTTGCACCCAGCTACAATTTTATCC	39
G6	TGAATCTTACCAACGCTAACGAGCGTCTTTCCAGAGCCT	39
G7	AATTTGCCAGTTACAAAATAAACAGCCATATTATTTATC	39
G8	CCAATCCAAATAAGAAACGATTTTTTGTTTAACGTCAAA	39
G9	AATGAAAATAGCAGCCTTTACAGAGAGAATAACATAAAA	39
G10	ACAGGGAAGCGCATTAGACGGGAGAATTAACTGAACACC	39
G11	CTGAACAAAGTCAGAGGGTAATTGAGCGCTAATATCAGA	39
G12	GAGATAACCCACAAGAATTGAGTTAAGCCCAATAATAAG	39
H1	AGCAAGAAACAATGAAATAGCAATAGCTATCTTACCGAA	39
H2	GCCCTTTTTAAGAAAAGTAAGCAGATAGCCGAACAAAGT	39
H3	TACCAGAAGGAAACCGAGGAAACGCAATAATAACGGAAT	39
H4	ACCCAAAAGAACTGGCATGATTAAGACTCCTTATTACGC	39
H5	AGTATGTTAGCAAACGTAGAAAATACATACATAAAGGTG	39
H6	GCAACATATAAAAGAAACGCAAAGACACCACGGAATAAG	39
H7	TTTATTTTGTCACAATCAATAGAAAATTCATATGGTTTA	39
H8	CCAGCGCCAAAGACAAAAGGGCGACATTCAACCGATTGA	39
H9	GGGAGGGAAGGTAAATATTGACGGAAATTATTCATTAAA	39
H10	GGTGAATTATCACCGTCACCGACTTGAGCCATTTGGGAA	39
H11	TTAGAGCCAGCAAAATCACCAGTAGCACCATTACCATTA	39
H12	GCAAGGCCGGAAACGTCACCAATGAAACCATCGATAGCA	39

I1	GCACCGTAATCAGTAGCGACAGAATCAAGTTTGCCTTTA	39
I2	GCGTCAGACTGTAGCGCGTTTTCATCGGCATTTTCGGTC	39
I3	ATAGCCCCCTTATTAGCGTTTGCCATCTTTTCATAATCA	39
I4	AAATCACCGGAACCAGAGCCACCACCGGAACCGCCTCCC	39
I5	TCAGAGCCGCCACCCTCAGAACCGCCACCCTCAGAGCCA	39
I6	CCACCCTCAGAGCCGCCACCAGAACCACCACCAGAGCCG	39
I7	CCGCCAGCATTGACAGGAGGTTGAGGCAGGTCAGACGAT	39
I8	TGGCCTTGATATTCACAAACAAATAAATCCTCATTAAAG	39
I9	CCAGAATGGAAAGCGCAGTCTCTGAATTTACCGTTCCAG	39
I10	TAAGCGTCATACATGGCTTTTGATGATACAGGAGTGTAC	39
I11	TGGTAATAAGTTTTAACGGGGTCAGTGCCTTGAGTAACA	39
I12	GTGCCCGTATAAACAGTTAATGCCCCCTGCCTATTTCGG	39
J1	AACCTATTATTCTGAAACATGAAAGTATTAAGAGGCTGA	39
J2	GACTCCTCAAGAGAAGGATTAGGATTAGCGGGGTTTTGC	39
J3	TCAGTACCAGGCGGATAAGTGCCGTCGAGAGGGTTGATA	39
J4	TAAGTATAGCCCGGAATAGGTGTATCACCGTACTCAGGA	39
J5	GGTTTAGTACCGCCACCCTCAGAACCGCCACCCTCAGAA	39
J6	CCGCCACCCTCAGAGCCACCACCCTCATTTTCAGGGATA	39
J7	GCAAGCCCAATAGGAACCCATGTACCGTAACACTGAGTT	39
J8	TCGTCACCAGTACAAACTACAACGCCTGTAGCATTCCAC	39
J9	AGACAGCCCTCATAGTTAGCGTAACGATCTAAAGTTTTG	39
J10	TCGTCTTTCCAGACGTTAGTAAATGAATTTTCTGTATGG	39
J11	GATTTTGCTAAACAACTTTCAACAGTTTCAGCGGAGTGA	39
J12	GAATAGAAAGGAACAACTAAAGGAATTGCGAATAATAAT	39
K1	TTTTTCACGTTGAAAATCTCCAAAAAAAAGGCTCCAAAA	39
K2	GGAGCCTTTAATTGTATCGGTTTATCAGCTTGCTTTCGA	39
K3	GGTGAATTTCTTAAACAGCTTGATACCGATAGTTGCGCC	39
K4	GACAATGACAACAACCATCGCCCACGCATAACCGATATA	39
K5	TTCGGTCGCTGAGGCTTGCAGGGAGTTAAAGGCCGCTTT	39
K6	TGCGGGATCGTCACCCTCAGCAGCGAAAGACAGCATCGG	39
K7	AACGAGGGTAGCAACGGCTACAGAGGCTTTGAGGACTAA	39
K8	AGACTTTTTCATGAGGAAGTTTCCATTAAACGGGTAAAA	39
K9	TACGTAATGCCACTACGAAGGCACCAACCTAAAACGAAA	39
K10	GAGGCAAAAGAATACACTAAAACACTCATCTTTGACCCC	39
K11	CAGCGATTATACCAAGCGCGAAACAAAGTACAACGGAGA	39
K12	TTTGTATCATCGCCTGATAAATTGTGTCGAAATCCGCGA	39
L1	CCTGCTCCATGTTACTTAGCCGGAACGAGGCGCAGACGG	39
L2	TCAATCATAAGGGAACCGAACTGACCAACTTTGAAAGAG	39
L3	GACAGATGAACGGTGTACAGACCAGGCGCATAGGCTGGC	39
L4	TGACCTTCATCAAGAGTAATCTTGACAAGAACCGGATAT	39
L5	TCATTACCCAAATCAACGTAACAAAGCTGCTCATTCAGT	39
L6	GAATAAGGCTTGCCCTGACGAGAAACACCAGAACGAGTA	39
L7	GTAAATTGGGCTTGAGATGGTTTAATTTCAACTTTAATC	39
L8	ATTGTGAATTACCTTATGCGATTTTAAGAACTGGCTCAT	39
L9	TATACCAGTCAGGACGTTGGGAAGAAAAATCTACGTTAA	39
L10	TAAAACGAACTAACGGAACAACATTATTACAGGTAGAAA	39
L11	GATTCATCAGTTGAGATTTAGGAATACCACATTCAACTA	39
L12	ATGCAGATACATAACGCCAAAAGGAATTACGAGGCATAG	39
M1	TAAGAGCAACACTATCATAACCCTCGTTTACCAGACGAC	39
M2	GATAAAAACCAAAATAGCGAGAGGCTTTTGCAAAAGAAG	39
M3	TTTTGCCAGAGGGGGTAATAGTAAAATGTTTAGACTGGA	39
M4	TAGCGTCCAATACTGCGGAATCGTCATAAATATTCATTG	39
M5	AATCCCCCTCAAATGCTTTAAACAGTTCAGAAAACGAGA	39

M6	ATGACCATAAATCAAAAATCAGGTCTTTACCCTGACTAT	39
M7	TATAGTCAGAAGCAAAGCGGATTGCATCAAAAAGATTAA	39
M8	GAGGAAGCCCGAAAGACTTCAAATATCGCGTTTTAATTC	39
M9	GAGCTTCAAAGCGAACCAGACCGGAAGCAAACTCCAACA	39
M10	GGTCAGGATTAGAGAGTACCTTTAATTGCTCCTTTTGAT	39
M11	AAGAGGTCATTTTTGCGGATGGCTTAGAGCTTAATTGCT	39
M12	GAATATAATGCTGTAGCTCAACATGTTTTAAATATGCAA	39
N1	CTAAAGTACGGTGTCTGGAAGTTTCATTCCATATAACAG	39
N2	TTGATTCCCAATTCTGCGAACGAGTAGATTTAGTTTGAC	39
N3	CATTAGATACATTTCGCAAATGGTCAATAACCTGTTTAG	39
N4	CTATATTTTCATTTGGGGCGCGAGCTGAAAAGGTGGCAT	39
N5	CAATTCTACTAATAGTAGTAGCATTAACATCCAATAAAT	39
N6	CATACAGGCAAGGCAAAGAATTAGCAAAATTAAGCAATA	39
N7	AAGCCTCAGAGCATAAAGCTAAATCGGTTGTACCAAAAA	39
N8	CATTATGACCCTGTAATACTTTTGCGGGAGAAGCCTTTA	39
N9	TTTCAACGCAAGGATAAAAATTTTTAGAACCCTCATATA	39
N10	TTTTAAATGCAATGCCTGAGTAATGTGTAGGTAAAGATT	39
N11	CAAAAGGGTGAGAAAGGCCGGAGACAGTCAAATCACCAT	39
N12	CAATATGATATTCAACCGTTCTAGCTGATAAATTAATGC	39
O1	CGGAGAGGGTAGCTATTTTTGAGAGATCTACAAAGGCTA	39
O2	TCAGGTCATTGCCTGAGAGTCTGGAGCAAACAAGAGAAT	39
O3	CGATGAACGGTAATCGTAAAACTAGCATGTCAATCATAT	39
O4	GTACCCCGGTTGATAATCAGAAAAGCCCCAAAAACAGGA	39
O5	AGATTGTATAAGCAAATATTTAAATTGTAAACGTTAATA	39
O6	TTTTGTTAAAATTCGCATTAAATTTTTGTTAAATCAGCT	39
O7	CATTTTTTAACCAATAGGAACGCCATCAAAAATAATTCG	39
O8	CGTCTGGCCTTCCTGTAGCCAGCTTTCATCAACATTAAA	39
O9	TGTGAGCGAGTAACAACCCGTCGGATTCTCCGTGGGAAC	39
O10	AAACGGCGGATTGACCGTAATGGGATAGGTCACGTTGGT	39
O11	GTAGATGGGCGCATCGTAACCGTGCATCTGCCAGTTTGA	39
O12	GGGGACGACGACAGTATCGGCCTCAGGAAGATCGCACTC	39
P1	CAGCCAGCTTTCCGGCACCGCTTCTGGTGCCGGAAACCA	39
P2	GGCAAAGCGCCATTCGCCATTCAGGCTGCGCAACTGTTG	39
P3	GGAAGGGCGATCGGTGCGGGCCTCTTCGCTATTACGCCA	39
P4	GCTGGCGAAAGGGGGATGTGCTGCAAGGCGATTAAGTTG	39
P5	GGTAACGCCAGGGTTTTCCCAGTCACGACGTTGT	34
P6	AAAACGACGGCCAGTGCCAAGCTTGCATGCCTGCAGGTC	39

2.3.2 Summary of nanopore properties and nanoswitch quantification.

Table 2.2 summarizes the nanopore geometries and results discussed in Section 2.1. Nanopore effective thicknesses l_{eff} and diameters d were calculated using dsDNA fragments as a molecular ruler (d_{dsDNA} = 2.2 nm) as described elsewhere.[44,81] Briefly, l_{eff} was extracted using Equation 2.1, where ΔG is the change in conductance of the nanopore upon translocation of the linear dsDNA fragments (such as that corresponding to linear

translocation events in Figure 2.7a) and σ_s is the conductivity of the electrolyte solution (16.2 Sm^{-1} for 3.6 M LiCl pH 8). The diameter of the nanopore d was then calculated using Equation 2.2 which accounts for access resistance of the nanopore, where the open nanopore conductance G_0 was obtained by monitoring the ionic current as an applied voltage was swept from -200 mV to +200 mV.[34]

$$l_{eff} = \frac{\sigma_s \pi d_{DNA}^2}{4\Delta G} \qquad (2.1)$$

$$d = \frac{G_0 + \sqrt{{G_0}^2 - \frac{16\sigma_s G_0 \, l_{eff}}{\pi}}}{2\sigma} \qquad (2.2)$$

In Table 2.2, samples listed are (1) dsDNA fragments, (2) scaffolds, or (3) ratios of the concentrations in nM during incubation of Zika gene target molecules to scaffolds. Nanopore experiments in which samples contained target were performed by diluting the concentrations listed in Table 2.2 with equal parts 3.6 M LiCl buffered to pH 8. Non-linear molecules determined from gel intensity measurements include both looped nanoswitches and concatamers, as described above in Section 2.3.2. Where indicated, some samples contained scaffold molecules that were incubated with T4 ligase in an attempt to remove nicks and encourage fully double-stranded scaffolds, but this did not significantly change nanopore readouts of nanoswitch formation. Data from NP22 is shown in Figure 2.2, while that of NP23 is shown in Figure 2.3b and Figure 2.4. For detailed statistics of event types for each sample and nanopore, please refer to the Table in Section 2.3.5.

Table 2.2. Summary of nanopore specifications and experimental content.

Pore ID	l_{eff} (nm)	d (nm)	Sample [targ]:[scaf] (nM)	Conditions	Non-linear (gel - %)	$\Delta I_{n>2}$ (%)
NP04	13.7	19.3	10kbp	400mV - 3.6MLiCl	0	5.1
			5:5	400mV - 1.8MLiCl	39.1	48.6
			5:5	200mV - 1.8MLiCl	39.1	45.9
NP06	17.6	10.8	10kbp	200mV - 3.6MLiCl	0	4.1
			Scaffold	200mV - 1.8MLiCl	0.2	6.7
			50:5	200mV - 2.3MLiCl	17.7	26.5
NP17	10.0	6.9	7kbp	200mV - 3.1MLiCl	0	0
			10:2 (T4-ligated)	200mV - 1.8MLiCl	58	54.2
			T4-ligated scaffold	200mV - 3.6MLiCl	23.8	10.8
NP20	9.6	8.1	7kbp-Mg	200mV - 1.8MLiCl	0	1.8
NP21	14.2	8.0	7kbp	200mV – 3.6MLiCl	0	0.9
			Scaffold	200mV-1.8MLiCl–No Mg^{2+}	4.2	5.6
			10:2	200mV-1.8MLiCl–No Mg^{2+}	4.4	19
			Scaffold	200mV - 1.8MLiCl	6.4	8.9
NP22	7.4	6.5	7kbp	200mV - 1.8MLiCl	0	2.8
			Scaffold	200mV - 1.8MLiCl	7.5	7.4
			10:2	200mV - 1.8MLiCl	64.4	55.5
			10:2 (T4-ligated)	200mV - 1.8MLiCl	73.5	56.5
			T4-ligated scaffold	200mV - 1.8MLiCl	4.3	9.7
NP23	8.1	6.5	7kbp	200mV - 1.8MLiCl	0	5.5
			3:2	200mV - 1.8MLiCl	73.1	62
			0.3:2	200mV - 1.8MLiCl	6.7	18.7
			1:2	200mV - 1.8MLiCl	28.2	30.1
			10:2	200mV - 2.3MLiCl	73.5	66.3
			0.1:2	200mV - 1.8MLiCl	2	12.5
			Scaffold	200mV - 1.8MLiCl	0	13.3
NP24	9.0	7.7	7kbp	200mV - 1.8MLiCl	0	2.9
			0.1:2	200mV - 1.8MLiCl	2	8
			3:2	200mV - 1.8MLiCl	73.1	54.7
NP25	8.8	6.6	7kbp	200mV - 3.6MLiCl	0	6.5
			1:2	200mV - 1.8MLiCl	28.2	28.1
			0.1:2	200mV - 1.8MLiCl	2	9.1
			3:2	200mV - 1.8MLiCl	73.1	65.5
			0.3:2	200mV - 1.8MLiCl	6.7	16.6
NP26	6.9	5.1	7kbp	200mV – 1.8MLiCl	0	NA
			Scaffold	200mV – pore too small	0	NA

2.3.3 Gel characterization of nanoswitches.

While several nanoswitch reactions were performed under various experimental conditions, the approach used to characterize all reactions is summarized in Figure 2.6.

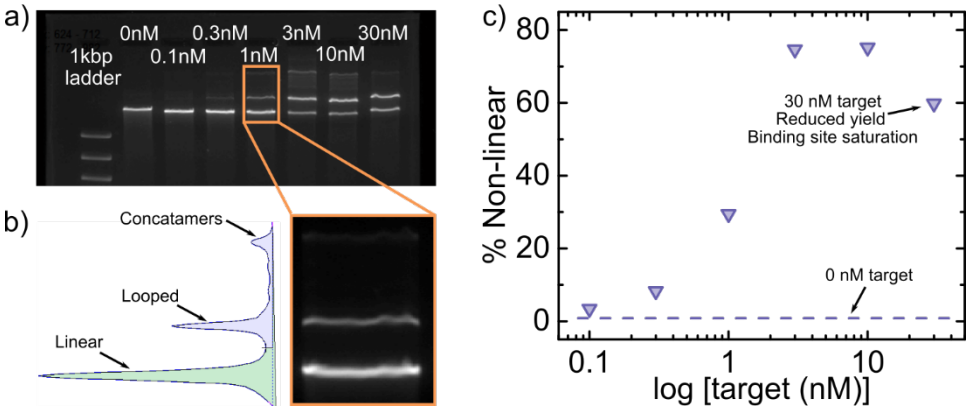

Figure 2.6. Gel Quantification.

a) Fluorescence image of the 1 % agarose gel used for quantifying loop formation as a function of target concentration from Figures 2.3 and 2.4 of Section 2.1. The first lane contained a dsDNA ladder (Thermo Scientific GeneRuler Express SM1553), while the remaining lanes consisted of 4 uL of samples containing 2 nM scaffold with varying amount (0nM to 30 nM) of the Zika target gene. b) Lanes contained bands corresponding to linear scaffolds, looped nanoswitches, and lower mobility molecules that were likely concatamers formed through inter-scaffold hybridization. Integration of fluorescence intensity of all non-linear bands (violet) relative to the total fluorescence intensity using GelBandFitter[86] provided a reaction yield to which nanopore experiments could be later compared (c). As expected, too much target (> 3 nM for these reaction conditions) reduced the amount of loop formation, as binding sites became saturated.

2.3.4 Translocation analysis

Raw ionic current traces for all experiments were analyzed using custom written analysis software[88,89] based on a CUSUM algorithm,[87] as described elsewhere.[81] Briefly, translocation events were detected as deviations of 6x the standard deviation σ of the open pore ionic current baseline. In order to minimize DNA fragments and impurities from further analysis, only events lasting >100 µs were considered. Changes of blockage

states within events were also triggered with a 6σ threshold, requiring a minimum of 3σ and duration of at least 12 µs to be considered a unique blockage state after fitting. Blockades lasting longer than 1 s were discarded as clogging events. Figures 2.7 and 2.8 show representative scatterplots and histograms summarizing the approach to nanoswitch characterization following analysis.

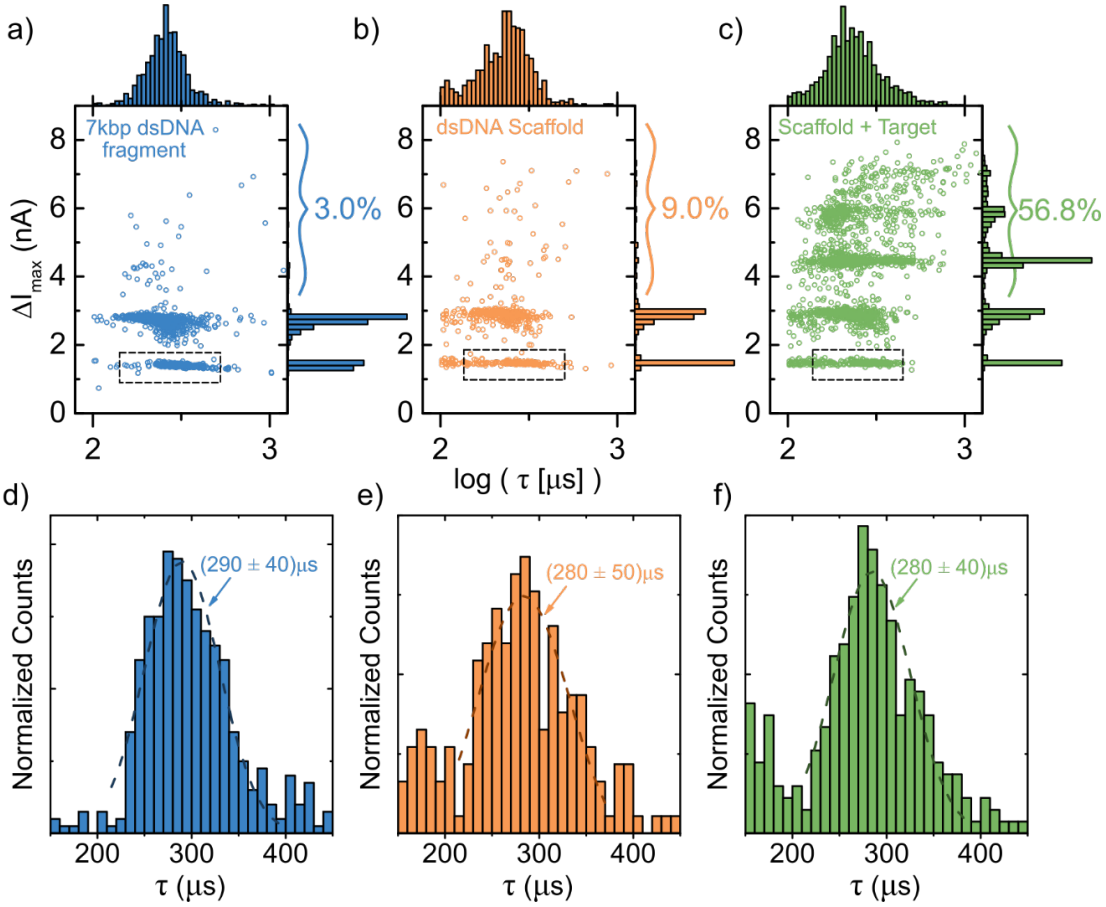

Figure 2.7. Translocation event analysis.

Scatter plots of ΔI_{max} vs. log(τ) for a) 7 kbp dsDNA fragments, b) scaffolds assembled from linearized M13mp18, tiles and binding site oligonucleotides, and c) nanoswitches formed through incubation of scaffolds with the target. Histograms of ΔI_{max} to the right of each scatter plot show varying amounts of higher order ($\Delta I_{n>2}$) translocation events, even between 7kbp dsDNA fragments and the assembled scaffold in the absence of target (unlooped scaffolds). Histograms of τ in (d)-(f) from the indicated regions in (a)-(c) for linear translocation events provide consistent translocation times between all species, showing that unfolded molecules translocate at a rate of approximately 40 µs/kbp, based on Gaussian fits of over the range indicated by the dashed lines.

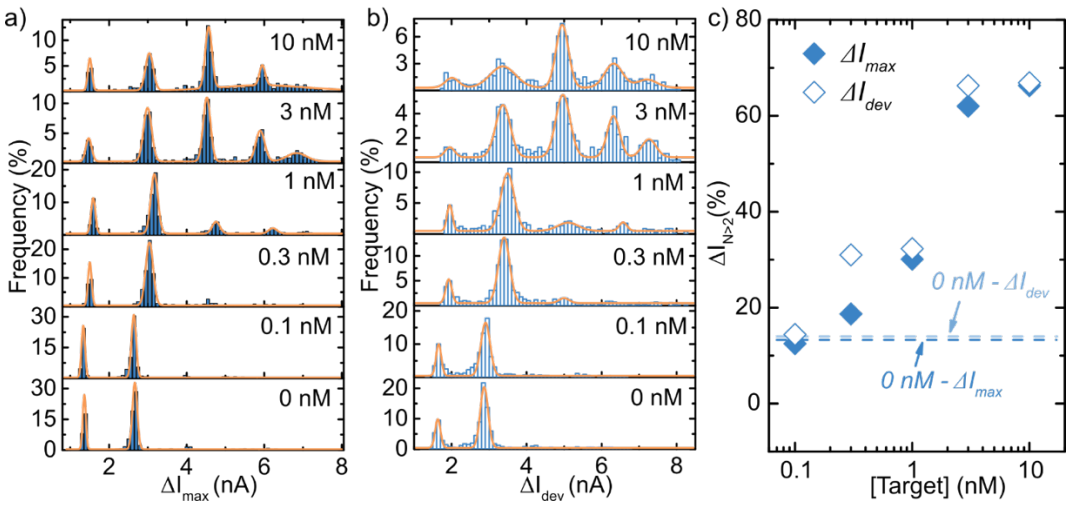

Figure 2.8. Nanopore quantification of nanoswitch formation.

Histograms of the ΔI_{max} (a) and the single ionic current data point that deviated the most from baseline ΔI_{dev} within each event (b) show peaks corresponding to a maximum of n = 1, 2, 3, 4 or 5 dsDNA segments in the nanopore during translocation. Gaussian fits allow peak location ΔI_n and standard deviation σ extraction. The fraction of events with $\Delta I_2 + 4\sigma$ for each sample (with the exception of the 10 nM sample in (b) which used the criterion $\Delta I_2 + 3\sigma$) is shown in (c), where most samples exhibit <3 % different between analysis metrics.

2.3.5 Event type analysis

Upon publication, a spreadsheet will be available on the ACS website containing event type data for all experiments presented in this chapter.

2.4 Acknowledgements

This work was supported by funding from the NSERC, the Ontario Early Research Award program, and CFI. The authors would also like to recognize Dr. Wesley Wong of the Wyss Institute at Harvard University for helpful discussions regarding nanoswitch design and characterization.

Chapter III.

Identifying structure in short DNA scaffolds using solid-state nanopores

3.0 Abstract

The identification of molecular tags along nucleic acid sequences has many potential applications in bionanotechnology, disease biomarker detection and DNA sequencing. An attractive approach to this end is the use of solid-state nanopores, which can electrically detect molecular substructure and can be integrated into portable lab-on-a-chip sensors. We present here a DNA origami-based approach of molecular assembly in which solid-state nanopores can differentiate 165 bp scaffolds containing zero, one and two dsDNA protrusions. This highly scalable technique requires minimal sample preparation and is customizable for a wide range of targets and applications. As a proof-of-concept, an aptamer-based DNA displacement reaction is performed in which a dsDNA protrusion is formed along a 255 bp scaffold in the presence of ATP. While ATP is too small to be directly sensed using conventional nanopore methods, our approach allows us to detect ATP by identifying molecular substructure along the DNA scaffold.

3.1 Main

3.1.1 Introduction

Nanopore sensors have recently attracted a great deal of attention due to their potential use in a wide range of applications from DNA sequencing[2] to disease biomarker detection.[2,55] Relying on the electrophoretic transport of charged species through a nano-scale aperture embedded in a thin insulating membrane, transient ionic current blockades produced as molecules displace ions from the sensing region of a nanopore yield information about the molecule's length, size and structure. Due to their controllable size[44,45] and ability to rapidly detect sub-nanomolar numbers of a biomolecular target in a label-free manner, solid-state nanopores are an attractive platform for sensing molecules with complex structure, such as DNA knots,[90] genetic modifications and defects,[91] Holliday junctions[92] and bound proteins.[93] The robust nature of the solid-state membrane and its flexible form factor also readily allow for integration within microfluidic devices with enhanced sample control for lab-on-a-chip functionality.[94,95]

While solid-state nanopores have been successfully used to detect complex molecular substructure and identify biomolecular species bound to linear DNA scaffolds at the single-molecule level,[61,83,93,96] achieving the resolution required to distinguish multiple targets has been challenging. Since the nanopore must be able to accommodate the molecule of interest, large molecules like proteins or antibodies require relatively large pores. This results in rapid translocation, as there is very little molecular interaction between the nanopore and the molecular complex. For applications such as molecular barcoding,[97,98] where a biomolecular target is specifically bound to a DNA backbone

containing a unique sequence of features for identification, rapid translocations impose the need to use large spacings (hundreds of base pairs) between identifying features which may in turn be made of up to tens of repeating subunits.[98] Also, generating double-stranded DNA (dsDNA) scaffolds of sufficient length can be costly and necessitates careful quality control, as existing schemes, such as those demonstrated using linearized M13 DNA (> 7 kbp in length), require hundreds of custom oligonucleotide sequences to anneal to a long single-stranded DNA (ssDNA) scaffold.[61,76,98–100]

In this work, we investigate the ability of nanopores made in thin solid-state membranes (< 10 nm) to distinguish small DNA tags (protrusions) along short dsDNA scaffolds. By scaling down the size of the scaffold, molecular tags, and thus the nanopore, we show that it is possible to detect the presence of a single 15 bp protrusion along a scaffold only 165 base pairs (bp) in total length. Additionally, we are able to distinguish the presence of zero, one and two small protrusions along such dsDNA scaffolds. Using DNA origami-inspired self-assembly of short (30-50 base) oligonucleotides, scaffold and protrusion generation can be scaled to the desired molecular length while keeping cost low and sample preparation to a minimum for greater simplicity and flexibility. In addition to confirming the ability of solid-state nanopores to distinguish populations of molecules containing short protrusions, we validate our molecular design scheme with a proof-of-concept DNA displacement reaction in which the presence of a small molecule (ATP) triggers the formation of a structural change in the molecule complex. Otherwise undetectable using standard translocation experiments due to its small size, ATP initiates a DNA displacement reaction which results in the formation of a dsDNA protrusion along a 255 bp scaffold, which is then sensed using a solid-state nanopore.

3.1.2 Results and Discussion

Nanopore detection of structural features of different sizes and number along a dsDNA scaffold molecule was first tested by generating DNA-origami scaffolds containing zero, one or two hybridized oligonucleotide protrusions. Utilizing the specificity of DNA hybridization, short oligonucleotide sequences were annealed to form dsDNA scaffolds 165 base pairs in length. By engineering the sequences used in assembly, DNA protrusions can be specifically placed at desired locations along the scaffold, as shown in Figure 3.1. We present the detection of four distinct molecular arrangements: bare scaffolds (P_0) containing no protrusions, scaffolds with one protrusion at the 105th base position (P_1, at ~ 2/3rd of the scaffold length), others with one protrusion at the 15th base position (P_2, at ~1/10th of the scaffold length), and some with two protrusions at both specified positions (P_{12}). Each protrusion is 15 bp in length, corresponding to a dsDNA segment of ~ 5 nm (half of the nominal 10 nm thickness of the SiN_x membranes used in this study). While the protrusion in P_1 is located relatively far away from the ends of the scaffold, the protrusion in P_2 is located such that one end of the scaffold contains a fork of two equal-length arms.

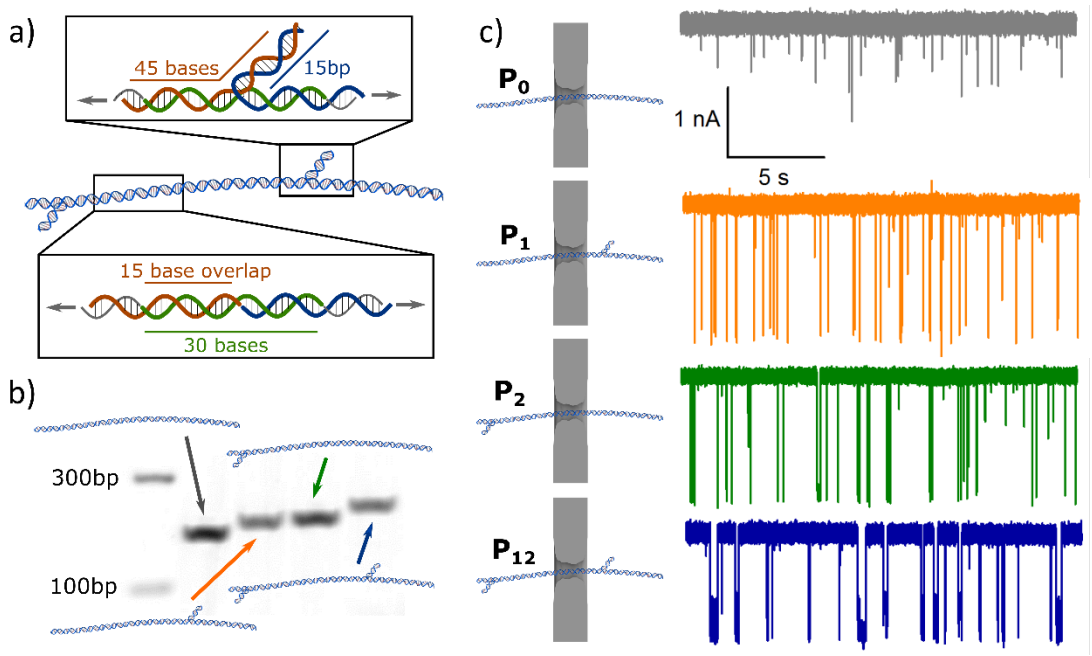

Figure 3.1. a) Overview of molecular assembly and nanopore sensing.

a) Schematic representation of the assembly of molecular complexes from short oligonucleotides with overlapping complementary sequences. (b) 165 bp scaffolds containing zero, one and two 15 bp protrusions are formed using the appropriate oligonucleotide sequences and characterized by 2 % agarose gel electrophoresis. (c) Representative ionic current traces while each molecule is analyzed using a single pore 3.6 nm in diameter in 3.6 M LiCl pH 8 at an applied bias of 150 mV. The open pore ionic current over the duration of the experiment was 1.95 ± 0.06 nA. Current traces were acquired at a sample rate of 500 kHz. Under these experimental conditions, bare scaffold molecules often translocate too quickly to be fully resolved and can be missed or attenuated due to the 100 kHz low-pass Bessel filter used.

Each sample was independently added to the *cis* reservoir of the fluidic cell at a final concentration of ~ 20 nM (assuming complete annealing of oligomer sequences). Translocation properties through a 3.8 nm diameter pore in a 10 nm thick membrane were then determined by extracting ionic current blockage levels and the corresponding dwell times within each translocation event under an applied potential difference (Figure 3.2a).[88,89] We note that as the translocation speed of observed events increases with increasing electrophoretic force (voltage), we confirm that these events are indeed due to

full translocation of molecules rather than collisions with the nanopore (Section 3.3.3). Due to the presence of multiple blockage states of widely varying duration within a single event, we have found that the maximum ionic current blockade ΔI_{max} (the sublevel with the deepest ionic current blockage within an event) provides a better metric for interpreting translocation events than the average ionic current blockade or event charge deficit. Histograms of the log-dwell time τ of the entire event and ΔI_{max} produced within each translocation event (Figure 3.2b-c) for bare scaffold molecules P_0 contain a single peak, as expected for dsDNA translocating unfolded through the nanopore. Molecules containing one or more protrusions produce a subpopulation of translocation events that is up to three orders of magnitude slower and exhibit a deeper blockage state during translocation through pores 3.5 ± 0.5 nm in diameter. For the experiment presented in Figure 3.2, <1% of bare scaffold translocation events resulted in both τ and ΔI_{max} longer than 750 μs and deeper than 1250 pA, respectively. On the other hand, 30 % and 34 % of detected P_1 and P_2 translocation events, respectively, exhibit deep blockage states and long translocation times. This ratio exceeds 80 % for P_{12} molecules containing two protrusions. While one might expect only one peak in the histogram of ΔI_{max} for molecules containing a protrusion, we have found that in many cases the molecules translocated too quickly for a deeper blockage state to be identified by our fitting algorithm at the bandwidth of recording. For an acquisition rate of 500 kHz, low-pass filtered at 100 kHz, the detection of a sublevel typically required that a change in ionic current be at least 6 times the RMS noise of the signal and last > 20 μs. While we were not able to observe a statistically significant difference in the translocation properties of P_1 and P_2 molecules, the presence of a protrusion was readily discernible in comparison

to bare scaffolds due to the significant population of long events containing deep blockage states. In addition to the histograms presented in Figure 3.2, a scatter plot of ΔI_{max} versus τ for all molecular species can be found in Figure 3.3.4.

It is important to note that P_1, P_2 and P_{12} molecules containing one and two protrusions are not always easily distinguished based on translocation time alone. As the presence of a protrusion contributes a significant amount of spread in the distribution of translocation times, neither the location of a single protrusion along the scaffold nor the addition of a second protrusion results in a significant shift in histograms of the log-translocation time, as shown in Figure 3.2b. In addition, there can be pore-to-pore variability in the sensitivity of a nanopore for detecting protrusions along dsDNA scaffolds. While nanopore size plays a large role in determining nanopore sensitivity, the ratio of translocation events that exhibit deep and long ionic current blockades for the same molecule can vary even between nanopores of similar diameter. While the average translocation times do not differ dramatically, a significant increase in the number of slower events for P_{12} molecules was observed compared to data acquired from molecules that have a single protrusion, as in Figure 3.2b.

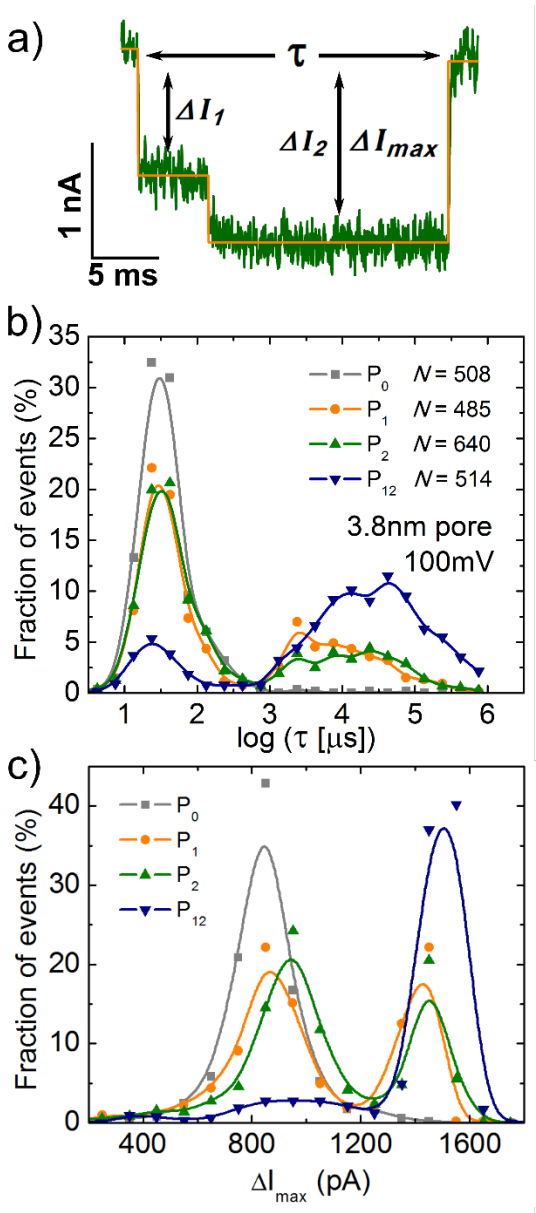

Figure 3.2. Translocation properties of scaffolds with varying number of protrustions.

(a) Raw ionic current trace (green) and fitted sublevels (orange) of a translocating P_2 molecule containing one protrusion. The protrusion along the scaffold is indicated by an increase in the change in ionic current from baseline (~1.8 nA at 100 mV) from ΔI_1 (corresponding to dsDNA) to ΔI_2 (dsDNA and a protrusion), which is the maximum blockage level ΔI_{max} for this translocation event. Histograms of the log-dwell time (b) and maximum ionic current blockage within each event (c) show an increasing fraction of events at long dwell times and deeper blockage as one and two protrusions are added to the scaffold. B-splines are shown in (b) and (c) as guides to the eye.

Molecular translocation events can be further distinguished by their specific structure within each ionic current signature. Figure 3.3a shows traces of translocation events in which different distinct ionic current sublevels were identified using our fitting algorithm. For the green trace in Figure 3.3a, we infer that the molecule first entered the nanopore producing a blockade corresponding to dsDNA occupying the nanopore sensing volume (ΔI_1), followed by a deeper blockage state (ΔI_2) corresponding to the translocation of the protrusion alongside the scaffold. We thus assign an event type of *12* for this event. Due to minimal interaction of the bare scaffold portions of molecules with the nanopore, ΔI_1 blockage states are short-lived (often < 20 μs), as shown in the *121*, *1212* and *12121* traces. This can result in this blockage state being overlooked by our fitting algorithm at the 100 kHz bandwidth used. As such, when attempting to distinguish P_{12} molecules, we consider both *1212* and *12121* event types as a positive "tags" for identification. We have found allows for the distinction of P_{12} molecules from those with a single protrusion with > 99 % confidence, as calculated by Morin *et al.*[83](Section 3.3.5). The normalized fraction of tagged events for each type of molecule is shown in Figure 3.3b. While the majority of translocation events for P_{12} molecules do not exhibit these event types, 84% of all positively tagged current signatures for a given nanopore were the result of a P_{12} translocation. Conversely, the relative fractions of P_1 and P_2 molecules exhibiting these event types are 7 % and 8 %, respectively. As expected, bare scaffold molecules exhibit almost no translocation events of the specified event types. While we do not expect to see these event signatures for P_1 and P_2 molecules, such false positives are a result of the tight parameters used in analysis in order to capture substructure in translocation events containing short blockage states (Section 3.3.4). The data in Figure

3.3b was obtained by first calculating the fraction of *1212* and *12121* events for a given molecule (Section 3.3.5). In order to account for variability in nanopore sensitivity (some nanopores were more sensitive for the detection of protrusions than others), the fraction of tagged events for a given molecule was then normalized to the sum of the fractions of such events for all molecules on a given nanopore. Error bars represent the standard deviation for 4 different nanopores in which each sample provided sufficient translocation events for molecular identification (> 2000 total events).

Similar to other studies recently published investigating the translocation of short biomolecules through solid-state nanopores,[92,101] we have found that the geometry of a nanopore plays a critical role in its ability to resolve molecules with differing number of protrusions. In this study, nanopore thickness (8 ± 2 nm) was calculated using the blockage depth of bare dsDNA, which was then used to determine nanopore diameter, as described in Section 3.3.1. While experiments using pores with diameters < 3 nm were possible, it was necessary to operate at higher electric fields generated from voltages > 300 mV in order to observe translocation events. In such cases, significant interaction of the scaffold with the nanopore resulted in broad translocation dwell times for all molecules, with significant overlap between species. We observed that with such small nanopores, ΔI_1 corresponding to the translocation of bare dsDNA resulted in > 70 % blockage of the ionic current. As such, ΔI_2 corresponding to the scaffold and protrusion was less than double that of the scaffold alone, as the secondary structure of the protrusion was disrupted in order for the complex to fully translocate. This secondary blockage was often difficult to resolve from ΔI_1 if the nanopore diameter was too small. Conversely, pores > 4 nm in diameter did not offer sufficient interaction with translocating molecules,

resulting in rapid translocation of all species and insufficient resolution to detect one or two protrusions only 15bp (~ 5 nm) long. We found that nanopore diameters of 3.5 ± 0.5 nm, which was readily achieved using our nanopore size tuning protocol,[44,45] offered the optimal balance of molecular interaction and change in signal amplitude to resolve the presence of the short dsDNA protrusions.

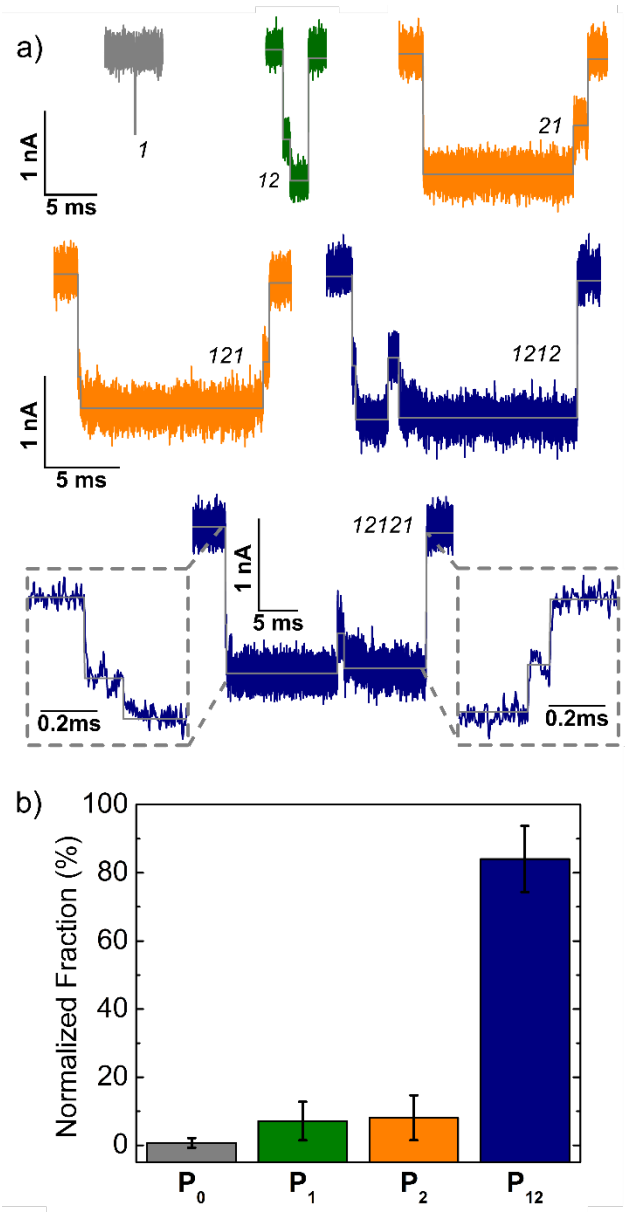

Figure 3.3. Event type analysis.

(a) Ionic current traces of representative event types assigned based on fitted current levels within each event (grey). Minimal interaction of bare scaffold with the nanopore results in relatively short ΔI_1 dwell times, with the majority of translocation time occurring in the ΔI_2 blockage state. Zooms of the short ΔI_1 levels are shown for the type 12121 event. Open pore ionic current levels were ~1.8 nA at a driving voltage of 100 mV. While trace color indicates which species produced each translocation signature, comparable event type distributions were observed for P_1 and P_2 molecules. (b) Normalized fractions of 1212 and 12121 event types for each molecule.

The ability of solid-state nanopores to differentiate molecules containing a dsDNA protrusion was leveraged to detect a specific molecule of interest which would otherwise be too small to be directly sensed using a solid-state nanopore. As a model system, we designed an aptamer-based sensing scheme[102,103] in which the presence of ATP (molecular weight of 0.551 kDa) initiated a DNA displacement reaction[104] which led to the formation of a dsDNA protrusion along a scaffold. A schematic overview of the expected displacement reaction is shown in Figure 3.4a. The scaffold molecule is first assembled by annealing a set of complementary 30-50 base oligonucleotides. For the purposes of this scheme, the scaffold molecule was extended to 255 bp in length and contained a free 20 base ssDNA overhang at the 105th base position. An aptamer sequence with high specificity for ATP,[105] initially completely hybridized in a hairpin structure and with a blocking strand, was then incubated with and without ATP. In the presence of ATP, the aptamer configuration is altered to expose a 5 base toehold region complementary to the ssDNA overhang of the scaffold. When incubated with the scaffold, the overhang then displaces the blocking strand and forms a protrusion on the scaffold consisting of 20 bases of dsDNA as well as the 26-base aptamer. Without ATP, the ssDNA overhang does not anneal to its complementary region of the aptamer molecule, as it is already fully hybridized with the hairpin structure of the aptamer and the blocking strand. Characterization of the reaction by gel electrophoresis in Figure 3.3b confirms that when ATP is present in the reaction mixture, a new band emerges as the bulkier (less mobile) aptamer-scaffold complex is formed. Without ATP, the addition of the blocked molecule has almost no effect on the band populations in lane II as compared to the scaffold alone (lane I).

We demonstrate the ability of solid-state nanopores to indirectly detect the small ATP molecule by performing translocation experiments using the reaction mixtures described above. Biomolecular translocation events through a pore 3.2 nm in diameter in 3.6 M LiCl were analyzed as described above. Density scatter plots of the maximum ionic current blockade versus the log-dwell time of scaffold molecules containing the ssDNA overhang, with and without ATP present in the reaction mixture, are shown in Figure 3.4. When ATP was not present in this experiment, 93 % of events exhibited maximum blockage depth consistent with dsDNA and lasted on the order of tens of microseconds, as shown in Figure 3.4c. While 7 % of molecules are present at deeper blockage levels (> 1700 pA) and longer dwell times (τ > 1 ms), this population is significantly more pronounced (38 % of events that met our criteria for successful translocation as described in Section 3.3.4) when ATP was added to initiate the displacement reaction (Figure 3.4d). Representative ionic current traces of translocation events in each population are shown in the insets of Figure 3.4c and 3.4d. In this experiment, observing substructure within events was more challenging than with molecules containing short 15 bp protrusions, as in Figure 3.3. Large nanopores again resulted in translocation events which were too fast to accurately identify ionic current sublevels. Conversely, smaller nanopores interacted very strongly with the bulkier molecule and provided almost exclusively deep blockage states during long events, presumably due to the increased size of the protrusion and scaffold. Nevertheless, statistical analysis of ΔI_{max} and log(τ) show that the presence of the protrusion (and thus ATP) was detected with 7 different nanopores with > 99 % confidence (Section 3.3.5). In addition, representative histograms of ΔI_{max} and log(τ) are shown in Section 3.3.6.

In addition to the data shown in Figure 3.4, we observed the translocation of linear 250 bp dsDNA fragments as well as the 255 bp assembled scaffold with and without the ssDNA overhang (Section 3.3.6). Such experiments provided a benchmark with which to compare the translocation properties of the more complex reaction mixtures, as well as allow for precise characterization of nanopore geometry (Section 3.3.1). We found that the assembled scaffold without a ssDNA overhang exhibited similar blockage depths and dwell times to the 250 bp control and did not show a significant increase in folded events. This result, as well as a complementary measurement of mobility by agarose gel electrophoresis, indicate that there is not a significant difference in persistent length between these species due to the presence of nicks in the assembled scaffold. Interestingly, an additional blockage level was present for some scaffold molecules containing the ssDNA overhang in the absence of the aptamer in some experiments. However, the ability to detect this particular sublevel was not consistent between nanopores, likely because the overhang was too flexible to significantly impede translocation, and its size compared to the nanopore sensing volume was too small to produce a significant signal relative to noise using the setup employed in these experiments.

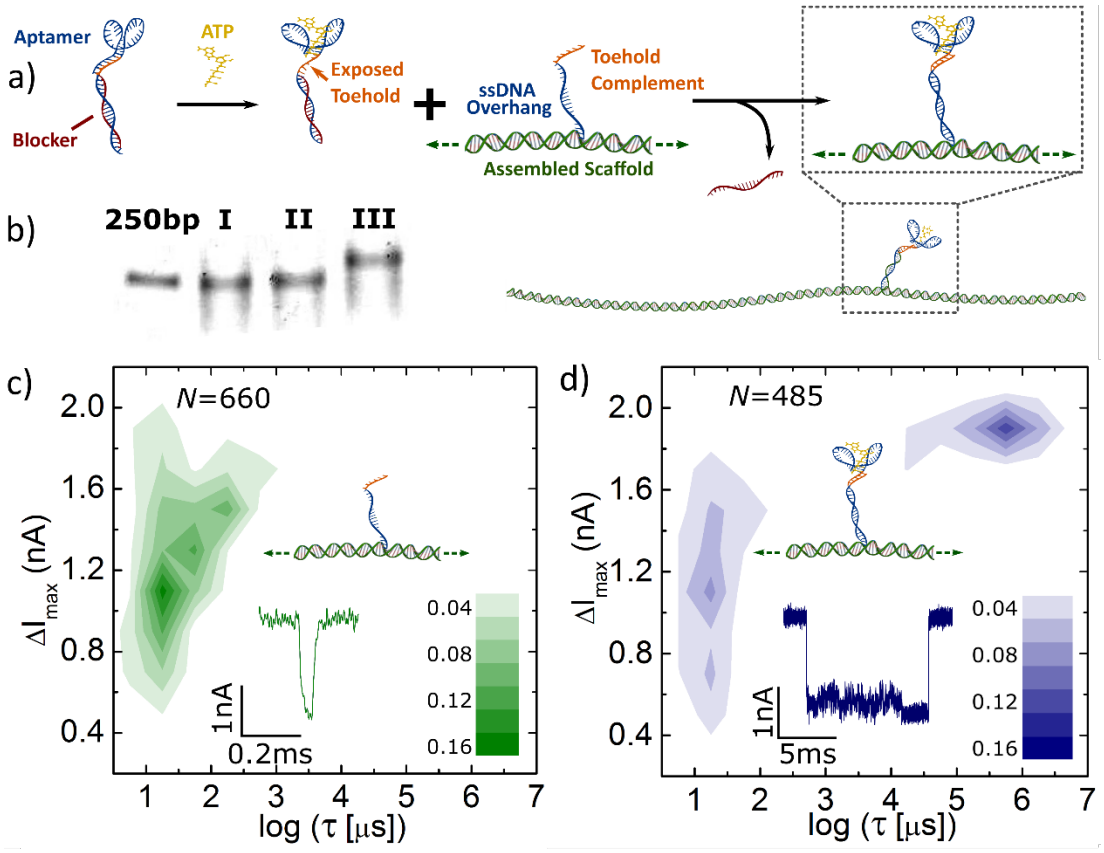

Figure 3.4. Nanopore sensing of ATP via the formation of a protrusion.

(a) Schematic representation of molecular complex assembly from short (30-50 bases) oligonucleotides via a DNA displacement reaction. In the presence of ATP, the aptamer is reconfigured to expose the toehold region. This allows the aptamer to bind to the ssDNA overhang of the scaffold, displacing a blocking strand and forming a dsDNA protrusion on the assembled scaffold. Without ATP, the aptamer sequence remains blocked and does not anneal with the scaffold. (b) The reaction is characterized by 2 % agarose gel electrophoresis, where the assembled scaffold alone (I) and the scaffold in the presence of the aptamer sequence (II) exhibit comparable mobility to 250 bp dsDNA. In the presence of ATP, the aptamer-scaffold complex is formed and is shifted relative to the other molecules (III). Density scatter plots of the maximum current blockage versus the log-dwell time of each translocation event through a pore 3.2 nm in diameter show that in the presence of ATP (d), 38 % of translocation events are deep and long, whereas only 8 % are so when ATP was not included in the reaction (c). Scales are normalized to the number of translocation events observed for each molecule and representative ionic current traces of translocation events for each species are shown. The applied potential was 150 mV and the open pore ionic current was ~2.3 nA.

3.1.3 Conclusions

The ability to discern molecular structure using solid-state nanopores has tremendous potential in disease biomarker detection, small molecule sensing and DNA sequence recognition. In this work, we demonstrate that nanopores fabricated in thin solid-state membranes can be used to differentiate short DNA origami structures containing a varying number of small, closely spaced protrusions. This approach was put in practice by identifying the presence of ATP, which initiated a DNA displacement reaction to form a protrusion on a molecular scaffold. This molecular assembly and detection method in which the target is replaced by a DNA label that remains bound to a scaffold under optimized nanopore conditions can be readily applied to a wide range of biomolecular targets for which aptamers have been selected to have high affinity. Additionally, recent demonstrations of nanopore integration within microfluidic networks[94,95] show promise for on-chip sample pre-processing and buffer exchange, which would allow for automated sensing of complex biological samples. With the advent of high-bandwidth amplifiers[42,106] and low-noise nanopore substrates,[107] we also envision that our flexible assembly approach could be expanded for multiplexing ability in molecular barcoding schemes and in the design of novel biomolecular assays.

3.2 Experimental Methods

3.2.1 Nanopore fabrication

Solid-state nanopores were fabricated in 10 nm thick (50 μm by 50 μm) SiN membrane windows (Norcada, part number NT005Z) using the CBD method.[24] Briefly,

the intact membrane windows were mounted in custom-built Teflon cells whereby the membrane electrically and fluidically isolated two 500 μL reservoirs containing ionic solution buffered at pH 8 using HEPES. Nanopore formation was initiated by applying an 8 V bias between the reservoirs containing 1 M KCl using Ag/AgCl electrodes while the leakage current was monitored through the membrane using custom-written LabVIEW software. When an abrupt increase of leakage current exceeding a threshold of 5 nA was observed, the applied bias was automatically removed. Under these conditions, the resulting nanopore size was typically < 3 nm in diameter. The nanopore size was then tuned using alternating pulses of ± 3 V until the desired conductance was achieved.[44,45] The ionic solution was then exchanged for 3.6 M LiCl and allowed to equilibrate for a minimum of 1 hour to allow the nanopore conductance to stabilize. Conductance measurements, as determined by sweeping an applied bias from -200 to 200 mV and measuring the resulting ionic current, are performed at each fabrication step and prior to the introduction of biomolecules to infer nanopore size (Section 3.3.1).

3.2.2. Sample preparation

All dsDNA scaffolds were formed by annealing short (30-50 bases) oligonucleotide sequences purchased from Integrated DNA Technologies (sequences in Section 3.3.2). Oligonucleotide sequences were diluted upon receipt to 100 μM in Duplex Buffer (Integrated DNA Technologies, catalogue number 11-05-01-12). Each sequence was added as required in equal molar ratios, with $MgCl_2$ added for a final concentration of 5 mM to stabilize annealed products. Each mixture was heated to 90 °C in a thermocycler and cooled to 4 °C at a rate of -3 °C per minute. For aptamer-based displacement reactions, the ATP-aptamer sequence (with the blocking strand already

annealed) was incubated with and without excess ATP (~ 2 mM) for 1 hour at 37 °C. The resulting complexes were added to the dsDNA scaffold containing a ssDNA overhang (1:2 molar ratio of scaffold to aptamer, assuming 100 % hybridization of oligonucleotides to form the scaffold), as previously described.[104] Molecular complexes from the displacement reaction were all used in nanopore experiments within 24 hours of formation, as repeated freeze/thaw cycles were found to encourage protrusion formation in the absence of ATP. Prior to introduction to the nanopore, all samples were characterized by electrophoresis in 2% agarose gels pre-stained with SYBR Green I (ThermoFisher Scientific S7563). All samples were added directly to the *cis* side of the nanopore without additional filtering. Fluidic reservoirs were flushed with fresh solution between samples until no translocation events were observed over the course of 1 minute to ensure that there were no residual molecules remaining from previous experiments.

3.2.3 Data acquisition and analysis

All I-V curves and ionic current signals were acquired with an Axopatch 200B (Molecular Devices) interfaced with custom-written LabVIEW software. Molecular translocation experiments were performed at a sampling rate of 500 kHz and low-pass filtered at 100 kHz. Translocation events were analyzed using an adapted version of the CUSUM+ algorithm[87,88] written in C. Briefly, ionic current traces were scanned without additional filtering to identify translocation events as abrupt changes in the magnitude of the ionic current exceeding 20-40 % of the mean ionic current. The CUSUM+ algorithm was then applied to identify different states in the ionic current blockade (sublevels) corresponding to different molecular segments passing through the nanopore. Further detail regarding data analysis can be found in Section 3.3.4.

3.3 Supporting Information

3.3.1 Nanopore fabrication and characterisation

Nanopore fabrication was performed by controlled breakdown (CBD), as described by Kwok, *et al*.[24] Briefly, an 8 V electric potential is applied across a 10-nm thick SiN_x membrane sealed between two aqueous reservoirs containing 1 M KCl pH 8. Leakage current through the membrane is monitored until an abrupt increase in current past a pre-set threshold is detected (typically 5-20 nA above the moving average of the previous 5 s of measured current), signifying the formation of a nanopore (Figure 3.5a). Brief alternating pulses of ±3 V were then employed to condition the nanopore to the desired conductance (size),[44] at which point the aqueous solution was exchanged for 3.6 M LiCl pH8 and to equilibrate for at least 1 hour. This equilibration step typically results in an increase of 0.2-0.5 nm in pore diameter.

Immediately prior to adding molecular samples, open nanopore conductance G_0 was obtained by monitoring the ionic current through the nanopore as a function of applied voltage (swept between ±200 mV), as shown in Figure 3.5b. The diameter of the nanopore d_p was then calculated using Equation 3.1 which accounts for access resistance of the nanopore, where σ is the conductivity of the electrolyte solution (16.6 Sm^{-1} for 3.6 M LiCl pH 8) and l_{eff} is the effective thickness of the nanopore, assuming a cylindrical geometry.[34] To determine l_{eff}, translocation experiments with 250 bp dsDNA fragments (ThermoFisher Scientific Cat. No. SM1451) were performed with the same nanopores as those used in experiments containing the biomolecular species of interest (Figure 3.5d). The effective thickness of the nanopore was then extracted using Equation 3.2, where ΔG

is the change in conductance of the nanopore upon translocation of the linear dsDNA fragments with a diameter d_{DNA} of 2.2 nm.

$$d_p = \frac{G_0 + \sqrt{{G_0}^2 - \frac{16\sigma G_0 \, l_{eff}}{\pi}}}{2\sigma} \qquad (3.1)$$

$$l_{eff} = \frac{\sigma \pi d_{DNA}^2}{4\Delta G} \qquad (3.2)$$

In addition to determining nanopore size prior to the addition of biomolecules, nanopore electrical noise properties were evaluated by obtaining power spectral density (PSD) and I_{RMS} plots of the ionic current as a function of frequency (Figure 3.5c). Nanopores exhibiting I_{RMS} values >20 pA at a bandwidth of 5 kHz were deemed too noisy and not used in biomolecular experiments. All nanopores formed using CBD and conditioned as described above exhibited low-noise properties, and only failed to be useful after they had become clogged in a previous sensing experiment.

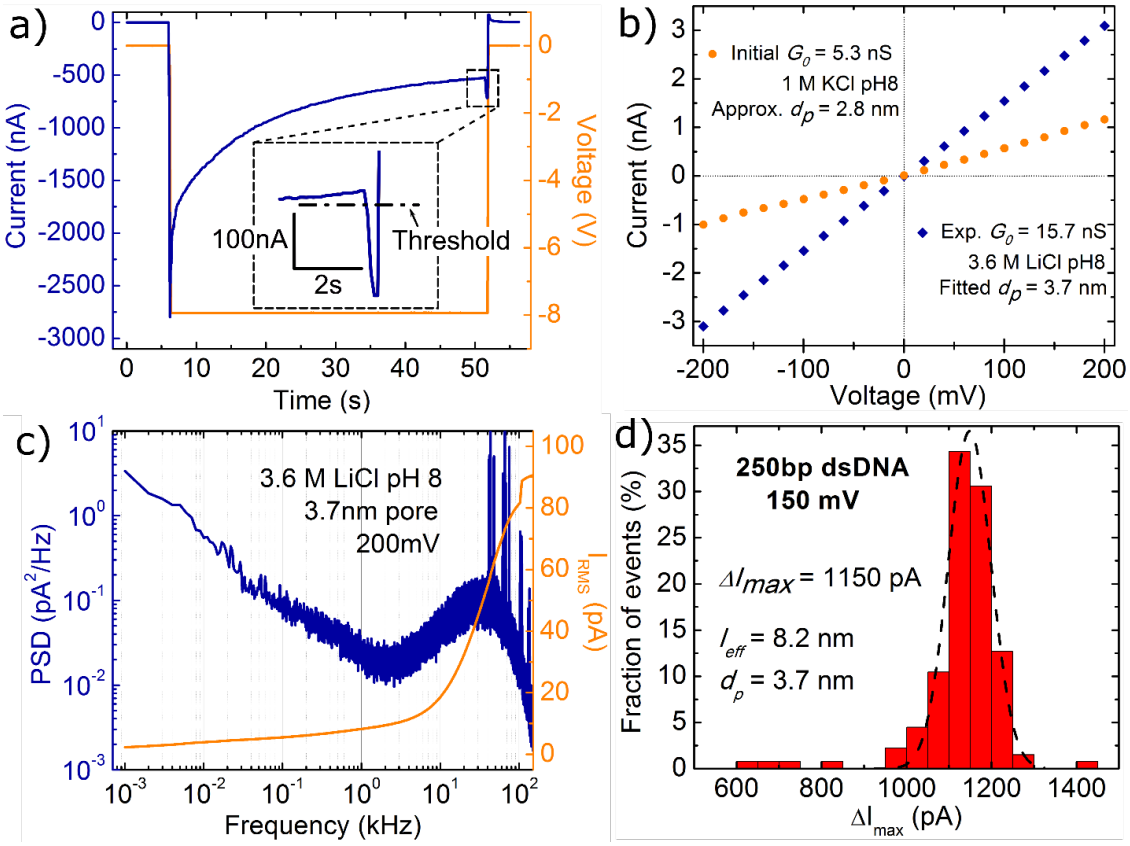

Figure 3.5. Nanopore fabrication and characterization.

(a) A typical nanopore fabrication curve. A sudden increase in the measured current past a threshold cutoff value at an applied bias of -8 V indicates the formation of a nanopore (inset). (b) I-V curve of the nanopore immediately after formation in 1 M KCl pH8 (orange). Its conductance indicates an approximate nanopore diameter of 2.8 nm, assuming a cylindrical geometry with a length of 10 nm (the nominal thickness of the nanopore membrane). After conditioning the nanopore with ±3 V pulses and equilibrating overnight in 3.6 M LiCl pH 8, the nanopore conductance is stable and has increased to 15.7 nS, indicating an increase in diameter (blue). (c) Power spectral density (PSD) and root-mean-square current plots of the ionic current noise as a function of frequency taken immediately prior to biomolecular sample introduction. (d) A histogram of the maximum ionic current blockage produced by the translocation of 250 bp dsDNA molecules. The peak at 1150 ± 50 pA is used to experimentally determine l_{eff}, which can be used in conjunction with the conductance obtained in (b) to calculate the diameter of the nanopore d_p. All data in this figure are from the same nanopore.

3.3.2 Molecular synthesis

All molecular assembly procedures were performed as described in Section 3.2. For the data presented in Figures 3.1 and 3.2, 165 bp scaffold molecules (P_0) were formed using the oligo sequences in Table 3.1.

Table 3.1 Oligonucleotide sequences used in 165 bp scaffold assembly.

Oligo ID	Sequence (5'-3')	Length
SCAF-A	CGACACTTAGTTCGTCCAGTCCTCTCACTGATGGCTGTACGCACT	45
SCAF-B	CCGTACTCTCACTACTGACTGATTATCCTC	30
SCAF-C	TAGCAGTCTCCATCCGCAATCAGAGGACCT	30
SCAF-D	GACGAAGTACCTTAGGAGACTGACTGATAC	30
SCAF-E	CCATCTCATACCAGCGTCCTACTGTTGAAG	30
COMP-A	CAGTGAGAGGACTGGACGAACTAAGTGTCG	30
LINK-BA	GTAGTGAGAGTACGGAGTGCGTACAGCCAT	30
LINK-CB	GGATGGAGACTGCTAGAGGATAATCAGTCA	30
LINK-DC	CTAAGGTACTTCGTCAGGTCCTCTGATTGC	30
LINK-ED	CTTCAACAGTAGGACGCTGGTATGAGATGGGTATCAGTCAGTCTC	45

P_1 molecules were formed by substituting LINK-BA and LINK-CB with PROT-BA and PROT-CB, while P_2 molecules were formed by substituting LINK-ED with PROT-ED and PROT-E. P_{12} samples were formed by making both substitutions. Protrusions are shown in Table 3.2 in orange and green.

Table 3.2 Oligonucleotide sequences used to form protrusions along scaffolds.

Oligo ID	Sequence (5'-3')	Length
PROT-BA	GTACGTCAAGCAGTCGTAGTGAGAGTACGGAGTGCGTACAGCCAT	45
PROT-CB	GGATGGAGACTGCTAGAGGATAATCAGTCAGACTGCTTGACGTAC	45
PROT-ED	CGGTCTCTCTGGTGAGCTGGTATGAGATGGGTATCAGTCAGTCTC	45
PROT-E	CTTCAACAGTAGGACTCACCAGAGAGACCG	30

For the data presented in Figure 3.3, 255 bp scaffold molecules containing an ssDNA overhang were formed by extending the scaffold S with the following oligos. To allow for extension and form the ssDNA overhang, LINK-ED was replaced with PROT-ED-comp. The ssDNA overhang is shown in green in Table 3.3, where the toehold portion of the overhang is shown in orange.

The dsDNA protrusion was formed in a displacement reaction in which the toehold region of ATP-aptamer becomes exposed upon aptamer reconfiguration. The aptamer sequence is shown in blue, while sequences complementary to PROT-ED-apt are shown in orange and green. The blocking strand (red) is initially annealed to the green sequence of the ATP-aptamer oligo.

Table 3.3 Oligonucleotide sequences used to detect ATP.

Oligo ID	Sequence (5'-3')	Length
PROT-ED-comp	AAGGTAGTGAGTCATCGTCAGCTGGTATGAGATGGGTATCAGTCAGTCTC	50
SCAF-F	CGTTGACTGTAGGCGACTGATCTACGACCT	30
SCAF-G	ATCGTAACGGCTTATCAGGTCTAGCGACTG	30
SCAF-H	AGCCCTATTGACTTGCTCATGCCATACTCG	30
LINK-FE	CGCCTACAGTCAACGCTTCAACAGTAGGAC	30
LINK-GF	ATAAGCCGTTACGATAGGTCGTAGATCAGT	30
LINK-HG	CGAGTATGGCATGAGCAAGTCAATAGGGCTCAGTCGCTAGACCTG	45
ATP-aptamer	TGACGATGACTCACTACCTTCCTGGGGGAGTATTGCGGAGGAAGGT	46
Blocker	AGTGAGTCATCGTCA	15

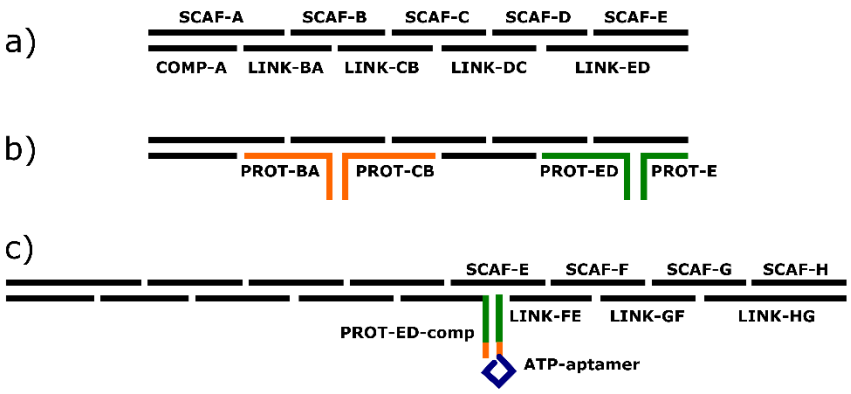

Figure 3.6. Schematic representations of the molecules used in translocation experiments.

(a) Bare scaffold molecules 165 bp in length are assembled using 10 unique oligonucleotide sequences either 30 or 45 bases in length. (b) By making the appropriate oligo substitutions, P_1 (orange) and P_2 (green) protrusions can be added to the scaffold. (c) 255 bp scaffold with a ssDNA overhang are formed by extending the scaffold used in (a). A dsDNA protrusion is formed in the presence of ATP through the addition of the ATP-aptamer oligo via DNA displacement, as shown in in Figure 3.4a of Section 3.1.

3.3.3 Translocation velocity with varying applied potential

In order to confirm that full molecular translocation through the nanopores (rather than collisions with the nanopore), experiments were performed over a range of applied potential biases. As the mean translocation time decreases with applied voltage (translocation speed increases with electrophoretic force), as shown in Figure 3.7, we conclude that molecules are indeed translocating through the nanopore.

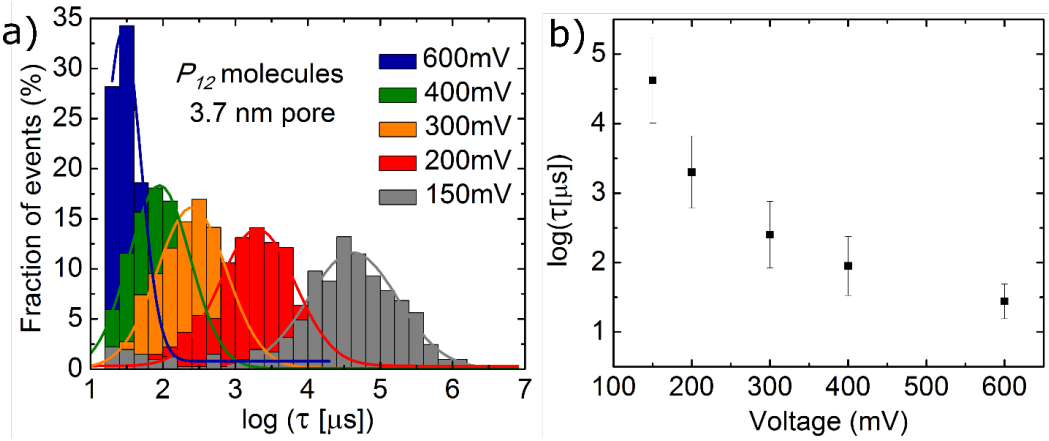

Figure 3.7. Mean translocation time of P_{12} molecules as a function of applied voltage.
a) Histograms of the log-dwell time of P_{12} molecules translocating through a 3.7 nm pore at varying applied voltages with superimposed Gaussian fits. b) The mean log-dwell times extracted from the fits in (a) as a function of voltage. Error bars are the standard deviation.

3.3.4 Translocation analysis

Raw ionic current traces for all experiments were analyzed using custom written analysis software[88,89] based on a CUSUM algorithm.[87] Translocation events were detected as deviations of 20-40 % (depending on nanopore size) of the mean baseline current lasting at least 20 μs. Translocation events of 20-40 μs were treated as single-level events, while those longer than 40 μs were scanned for sublevels. Ionic current levels were calculated as the average current within a sublevel, excluding the first 10 μs of each event. Blockades lasting longer than 10 s were discarded as clogging events.

Transitions between sublevels were established by defining expected blockage parameter of 500-1000 pA and variable detection threshold, as defined elsewhere.[108] Sublevel current values were defined as the average ionic current between states relative to that of the open nanopore, excluding the first 10 μs of each sublevel.

A scatter plot of the maximum ionic current blockage ΔI_{max} versus the total dwell time τ produced by the translocation of all molecules through a 3.8 nm pore at 100 mV is shown in Figure 3.8. This is a 2D representation of the histograms in Figure 3.2. In order to extract event types, as in Figure 3.2d, histograms of the blockage levels within all events for a given molecule were plotted as in Figure 3.9 to identify blockage states as ΔI_1 or ΔI_2. Event types were then assigned based on the sequence of blockage states present within each event. In order to identify P_{12} molecules containing two protrusions, events types *1212* and *12121* for each sample were counted and compared for each molecule studied (Table S1).

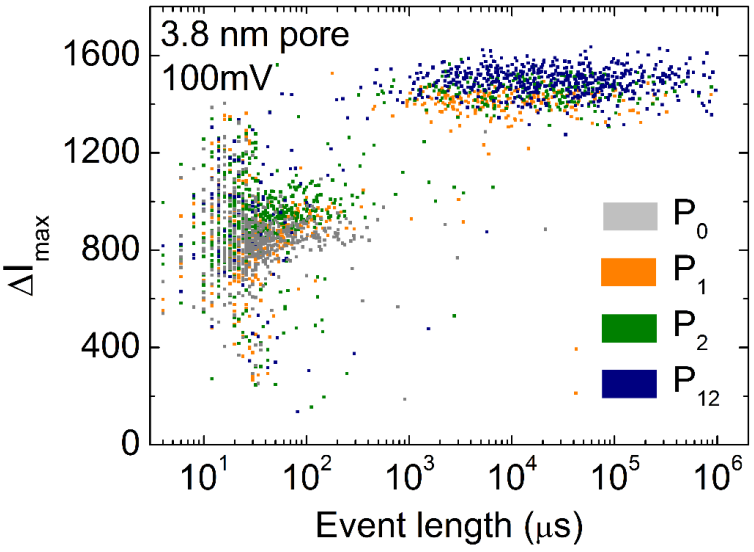

Figure 3.8. Scatter plot of ΔI_{max} versus τ for each molecule translocating through a 3.8 nm pore at 100mV.

Data was obtained using pore P-03 from Table S1 and is used in the generation of histograms in Figure 3.2.

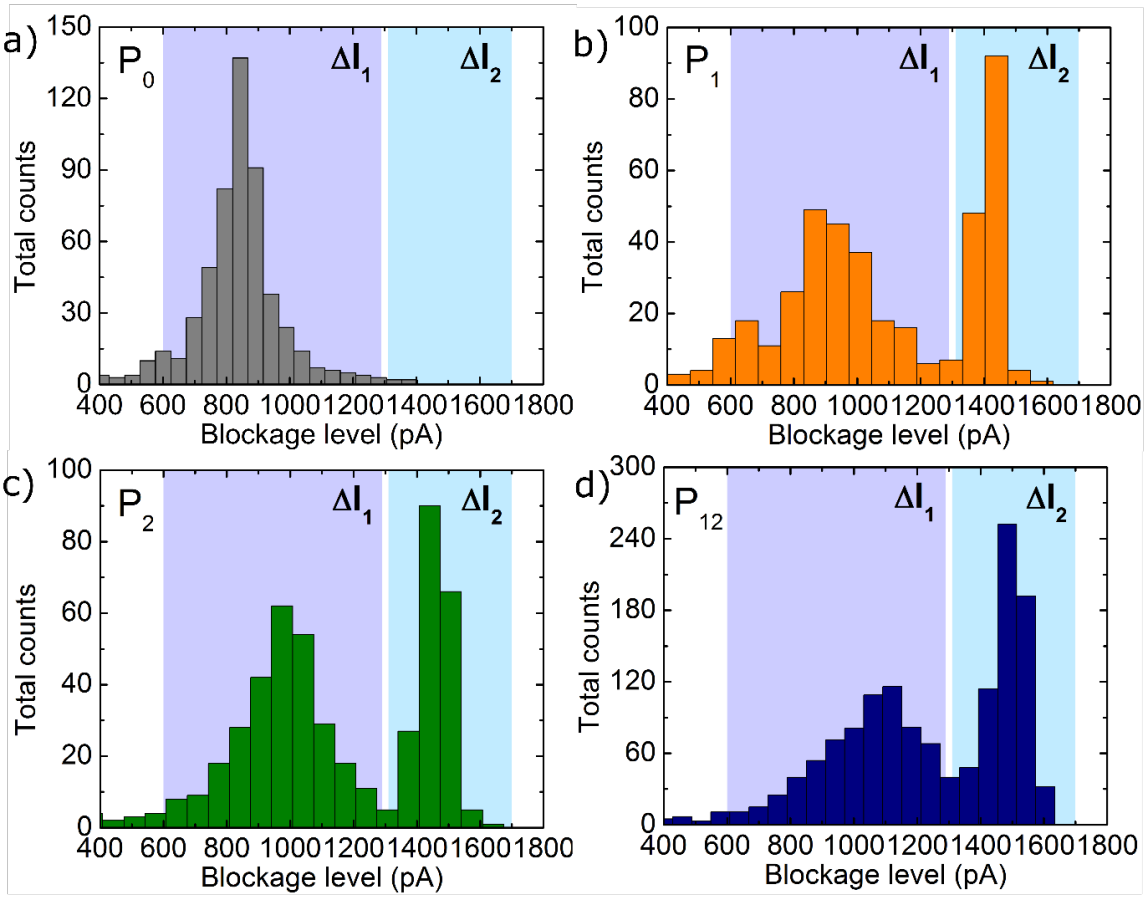

Figure 3.9. Histograms of blockage levels.

Blockage level histograms for 165 bp scaffold P_0 molecules (a), P_1 (b) and P_2 (c) molecules containing a single protrusion and P_{12} molecules (d) containing two protrusions. Example windows used to identify blockage levels as dsDNA (ΔI_1) and dsDNA plus a protrusion (ΔI_2) are highlighted by lilac and cyan backgrounds, respectively. The sequence of such blockage states is used to identify event type.

3.3.5 Experimental translocation data

Table 3.4 contains statistics on the translocation of molecules containing different numbers of protrusions. Table 3.5 provides statistics on experiments performed to detect the presence of ATP in sample mixtures with and without ATP as described in Figure 3.4. In all cases, molecules were tested in a randomized order with a given nanopore to ensure that trends were not an artifact of nanopore age (use). Nanopore were flushed

extensively between molecular sensing experiments with >10 mL of fresh ionic solution until no translocation events were observed over the course of one minute.

Table 3.4. Statistics on translocation events for molecules containing zero, one or two protrusions.

Nanopore diameter d_p is calculated as described in Section 3.3.1. Valid events are those as described in Section 3.3.4, while type 1212+ events include both 1212 and 12121 event types. A confidence interval of 99% is calculated as described elsewhere,[83] where the presence of P_{12} sample is detected within a 99% confidence interval if $Q_{12} - Q^* > Q_i$, where i can refer to any of the other control molecules tested. Data shown in Figure 3.1 were obtained using pore P-02, while that in Figures 3.2 and 3.3 were obtained using pore P-03.

Pore ID	d_p (nm)	Voltage (mV)	Sample	Valid events	Type *1212*+ events	% tagged *Q*	99% confidence interval *Q** (%)
P-01	3.7	200	P_0	258	0	0.0	--
			P_1	1006	2	0.2	--
			P_2	632	2	0.3	--
			P_{12}	498	133	26.7	5.1
P-02	3.6	150	P_0	797	7	0.9	--
			P_1	953	41	4.3	--
			P_2	449	5	1.1	--
			P_{12}	308	75	24.4	6.3
P-03	3.8	100	P_0	508	0	0.0	--
			P_1	485	1	0.2	--
			P_2	640	4	0.6	--
			P_{12}	514	20	3.9	2.2
P-04	3.1	150	P_0	643	0	0.0	--
			P_1	536	5	0.9	--
			P_2	946	7	0.7	--
			P_{12}	595	32	5.4	2.4

Table 3.5. Statistics on translocation events used in the detection of ATP.

Nanopore diameter d_p is calculated as described in Section 3.3.1 and sample types are as indicated in Figure 3.4 (sample type II contains a mixture of scaffold and blocked aptamer, while sample type III also contains ATP). Valid events are those as described in Section 3.3.4, while Q is the percentage of events with maximum blockage levels and log-dwell times exceeding a threshold value. Threshold values for ΔI_{max} and $\log(\tau)$ varied with pore size, ranging from 40-70 % of the baseline ionic current and 0.3-10 ms, respectively. A confidence interval of 99% is calculated as described elsewhere,[83] where the presence of a dsDNA protrusion (and thus ATP) is detected within a 99% confidence interval if $Q_{III} - Q^* > Q_{II}$, where Q_{II} is determined in a control experiment that does not contain ATP. The data shown in Figure 3.4 was obtained using pore ATP-02.

Pore ID	d_p (nm)	Voltage (mV)	Sample type	Valid events	Tagged events	% tagged Q	99% confidence interval Q^* (%)
ATP-01	3.4	200	II	1342	309	23.0	--
			III	918	471	51.3	4.2
ATP-02	3.2	150	II	660	35	5.3	--
			III	485	170	35.1	5.6
ATP-03	4.4	100	II	2639	384	14.6	--
			III	1686	538	31.9	2.9
ATP-04	3.6	300	II	3375	778	23.1	--
			III	3155	1197	37.9	2.2
ATP-05	6.0	100	II	475	17	3.6	--
			III	492	177	36.0	5.6
ATP-06	3.1	500	II	546	14	2.6	--
			III	1049	303	28.9	3.6
ATP-07	5.4	100	II	215	26	12.1	--
			III	373	174	46.6	6.7

3.3.6 Translocation properties of mixtures for the detection of ATP

The 2D histograms shown in Figure 3.4 were decomposed into 1D histograms of the maximum blockage level and log-dwell times of translocating molecules in order to assess the presence of ATP in the sample mixture. As a benchmark to characterize molecular formation, 255 bp scaffolds were assembled from 30-45 base oligos such that there were no protrusions (red in Figure 3.10). These scaffolds exhibited similar blockage depths and translocation times to the 250 bp dsDNA fragments used for nanopore size

characterization (Figure 3.5). Histograms of the maximum blockage depth for molecules containing a ssDNA overhang (green in Figure 3.10a) revealed a peak in between those corresponding to dsDNA and dsDNA with a protrusion, presumably indicating the presence of the overhang. However, this peak was only observed in two of the seven nanopores presented in Section 3.3.5.

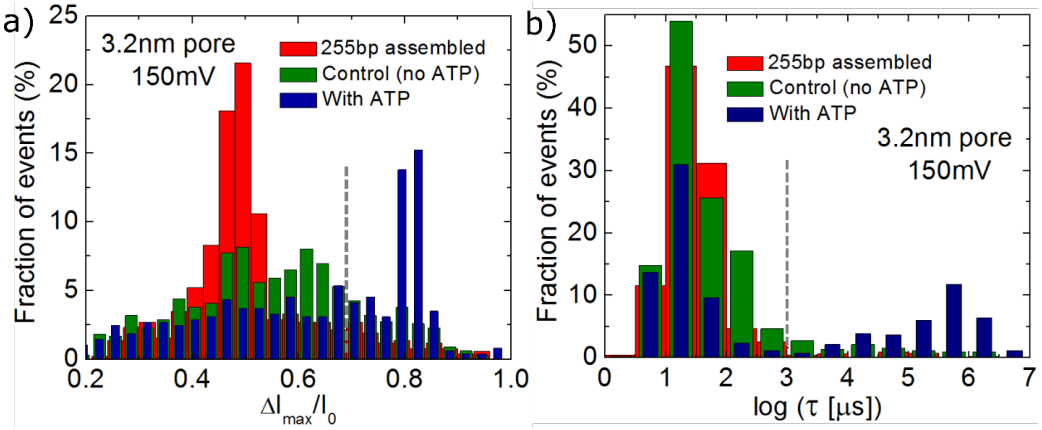

Figure 3.10 Histograms for ATP detection.

Histograms of (a) the relative maximum blockage and (b) log-dwell times of molecules used in detecting the presence of ATP. 255 bp assembled scaffolds (red) do not contain any protrusion (neither the ssDNA overhang nor that corresponding to the molecule complexed with the ATP aptamer sequence). The control molecule (green) contains a ssDNA overhang (sample II from Figure 3.3) while the aptamer sequence is present in reaction mixture. Sample III from Figure 3.4 contains excess ATP (blue). Grey dashed lines represent the threshold values used in assessing the presence of the protrusion (and thus ATP) described in Section 3.3.5 and varied with nanopore size.

3.4 Acknowledgements

This work was supported by funding from NSERC, the Ontario Ministry of Research and Innovation, and CFI. The authors would also like to thank Drs. David Juncker and Andy Ng of McGill University for valuable discussions regarding aptamer-based DNA displacement assays and Dr. Kyle Briggs for his contributions in developing nanopore translocation analysis software.

Chapter IV.

Digital counting of microRNA using solid-state nanopores

4.0 Abstract

This Chapter represents the culmination the insights learned from our previous work. Here we combine the ability to identify with a high degree of certainty the presence of a biomolecular target on a per-event basis with the inherent advantages of short scaffolds. Rather than attempting to detect relatively small features along individual scaffolds, this investigation relied on the conjugation of two separate DNA structures via a target molecule of interest in a probe-based assay. In these experiments, three sets of molecular probes were designed, each consisting of two structurally equivalent molecules to simplify analysis. Each probe set contained binding sites complementary to one half of a specific sequence of circulating microRNA (miRNA), a biomarker that has been associated with various cancers, to provide a highly specific identifier for the presence of a target molecule. By examining the relative counts of bound and unbound probes, we are able to distinguish six different concentrations of miRNA within a single order of magnitude in minutes by sensing only hundreds of individual molecules.

4.1 Main

4.1.1 Introduction

The detection and quantification of small molecules such as microRNA (miRNA) show great promise for monitoring the initiation and progression of various cancers.[109] However, the development of a simple, robust assay, and subsequent biomolecular sensing platform, remains a challenge. For instance, reverse transcription quantitative polymerase chain reaction (qRT-PCR) is a highly sensitive method for detecting low levels of circulating miRNA. However, it has proven difficult to develop high-throughput qRT-PCR assays and to successfully integrate operable systems within lab-on-a-chip (LOC) devices.[110] Microarrays, on the other hand, while providing high throughput, often suffer the drawbacks of lower sensitivity or reduced specificity.[109,110] Solid-state nanopores provide an attractive alternative as a detection platform in that individual molecules can be digitally counted for high sensitivity, and can be readily integrated within LOC devices for a potentially high throughput.[78,95]

Nanopore sensors have recently attracted a great deal of attention as single-molecule detectors showing promise for enhanced diagnostics and point-of-care technologies.[10,11,111,112] Nanopores fabricated in solid-state membranes,[12,13] in particular, offer the ability to tune sensor dimensions to the particular molecular targets or the products of a bioassay that are to be detected. Disease diagnostics using solid-state nanopore sensors, however, have thus far been limited to binding targets on long (1000 - 50 000 bp) polynucleotide scaffolds,[59,61,113] processing membranes prior to sensing using

ion beam milling,[114] or relying on multi-step biochemistry and purification for specific detection.[114,115]

Despite the importance of miRNA as a biomarker for diseases such as prostate, lung and colon cancers,[116–118] to date, very few successful reports of its detection using solid-state nanopore platforms have been reported. Wanunu *et al.* highlighted the ability of small nanopores formed in membranes thinned from ion beam lithography to distinguish miRNA from purified rat liver, with a sensitivity rivalling that of PCR-based methods.[114] Zahid *et al.* have also presented work in which miRNA could be specifically detected from a mixture of potential targets by binding a ssDNA probe tethered to a monovalent streptavidin protein, leveraging the selectivity of a solid-state nanopore to detect bulky molecules.[96] While a capture rate enhancement was measured when the RNA target hybridized to the appropriate probe in the latter example, this method was not conducive to concentration quantification due to a high number of missed events, and was therefore not ideally suited to an assay targeting miRNA for diagnostic purposes. Adding to the challenge of both approaches, circulating miRNA indicative of disease progression exhibit a high degree of sequence similarity, which can result in non-specific binding of probes to competing nucleic acid sequences.[109,119]

There is therefore a need for an assay with a high degree of specificity for a particular miRNA sequence of interest that can also provide a measurement of concentration, despite the very low copy numbers that are present in patient samples.[110,120,121] In order to realize the potential of solid-state nanopores to achieve such readouts robustly and in only hundreds of individual molecules, an assay must not only provide unambiguous measurements on a per-molecule basis, but also be relatively

insensitive to nanopore geometry. Ideally, solid-state membranes would also require little preparation, such as thinning using high energy electron microscopes,[114] for eventual integration within handheld LOC devices.

Our recent work has shown that solid-state nanopore sensors can achieve a high degree of specificity and sensitivity to provide signals with a strong SNR that are easily distinguishable from background by inducing a change in molecular properties.[81,82] Specifically, we have shown that short dsDNA fragments can serve as scaffolds to which molecular features can be bound and detected to provide a yes-or-no response to the presence of a target of interest upon analysis of population statistics.[81] Here, we provide an assay in which short, highly customisable DNA probes specifically bind to miRNA molecules, forming larger molecular complexes that are highly differentiable in solid-state nanopore recordings. This allows for a high degree of specific detection of target molecules on a per-molecule basis due to low ambiguity in ionic current signature identification. Moreover, through careful design of probe structure,[122] our assay design enables the quantification of miRNA concentrations with a high degree of accuracy, without amplification, over a tuneable concentration range within a diagnostically relevant time-to-response (TTR). We also demonstrate the potential for this approach to be used in multiplexed target detection, where different targets are simultaneously specifically detected amid a background of different probes and targets.

4.1.2 Results and Discussion

The principle behind our assay is shown in Figure 4.1a, where small double-stranded DNA (dsDNA) probes are assembled from short complementary single-stranded DNA (ssDNA) oligomers that are easily designed and inexpensively synthesized. Rather

than using a single probe for target binding, our assay involves sets of two probes containing ssDNA overhangs that are complementary to unique portions of the target sequence of interest. Upon binding of the appropriate target sequence, both probes within a set become conjugated to form DNA-based structures with multiple branches. Absent the appropriate target sequence, probe molecules do not form multiple branched structures in solution. However, the similar structure of probes within a set structure serves to minimize the amount of unique ionic current signatures that would be detected by our analysis algorithm upon nanopore sensing, thus reducing the number false positive signals that might appear in the presence of the target molecule.

We compare three probe sets of various sizes and configurations for miRNA detection and quantification, each with a unique binding site for a specific miRNA target of interest (Figure 4.1). The target miRNA sequences (miRNA-155, -141 and -122) were initially substituted with their ssDNA equivalents (ssDNA-155, -141 and -122, respectively) due to the reduced cost and sensitivity to environmental conditions of DNA compared to RNA for preliminary testing assay performance. Schematically shown Figure 4.1a, the first probe set (PS-155) consisted of 98-base dsDNA structures with binding sites complementary to ssDNA-155 that forked from the approximate mid-points of the molecules. Upon target binding, the assembled complex (AC-155) contained both probes tethered by a 23 bp dsDNA segment (or a mixed DNA-RNA 23 bp structure in later miRNA experiments). Figure 4.1b shows a second probe set PS-141 with similar 98 bp linear segment dsDNA but containing branches 40 bp in length at the junction of the ssDNA-141 binding site. The resulting assembled complex AC-141 effectively contained 6 separate branches of dsDNA. Figure 4.1c shows the smallest probe structure tested,

consisting of a 50 bp segment with a 14 bp branch that extended directly into a binding site complementary to ssDNA-122 (PS-122). The corresponding assembled complex AC-122 essentially consisted of an H-shaped structure where every linear segment was 50 bp in length.

In order to compare different complexed molecular structures between experiments with different nanopores, blockage depth is characterized throughout this work as ΔI_{dsDNA}, defined as the maximum deviation in ionic current from baseline within an event ΔI_{max} (insets in Figure 4.1) relative to the ΔI_{max} observed for the translocation of 100 bp dsDNA fragments using the same nanopore (Section 4.3.3). For example, a ΔI_{dsDNA} value of 2 signifies that a branched structure blocked twice the amount of ionic current as a 100 bp dsDNA molecule translating through the same nanopore. As shown in Figure 4.1, nanopore sensing experiments show that a single population arose from each geometrically identical probe set in the absence of target molecules in density contour plots of ΔI_{dsDNA} versus translocation time, τ. Assembled complexes containing the ssDNA target produced a second population of deeper, longer blockages distinct from those corresponding to unbound probes. As expected for a linear structure of similar length to the 100 bp fragment but containing a short ssDNA overhang, PS-155 exhibited ΔI_{dsDNA} only slightly greater than 1 ($\Delta I_{dsDNA} = 1.1 \pm 0.2$ in Figure 4.1a). PS-141, on the other hand, exhibited ΔI_{dsDNA} 1.7 ± 0.5 in Figure 1b. Upon conjugation with the appropriate target sequences, populations at $\Delta I_{dsDNA} = 2.5 \pm 0.4$ and 4.0 ± 1.2 were observed for AC-155 and AC-141, respectively, with uniquely located peaks. In the case of AC-155, a secondary blockage state is observed following entry of a single arm of the structure (inset of Figure 4.1a) that is approximately 2.5 times greater than the blockage

state of PS-155, in good agreement with previous nanopore measurements of Holliday junctions of similar size and structure.[82,92,123] While the smallest probe set PS-122 produced a statistically significant difference in dwell times upon binding ssDNA-122 in Figure 4.1c, comparable ΔI_{dsDNA} values obtained between probe sets and assembled complexes for the range of nanopore sizes used (7-10 nm in diameter) ultimately resulted in more difficult molecular identification in mixed samples. This was further challenged by the presence of incompletely assembled molecules that were present in all prepared mixtures (Section 4.3.2).

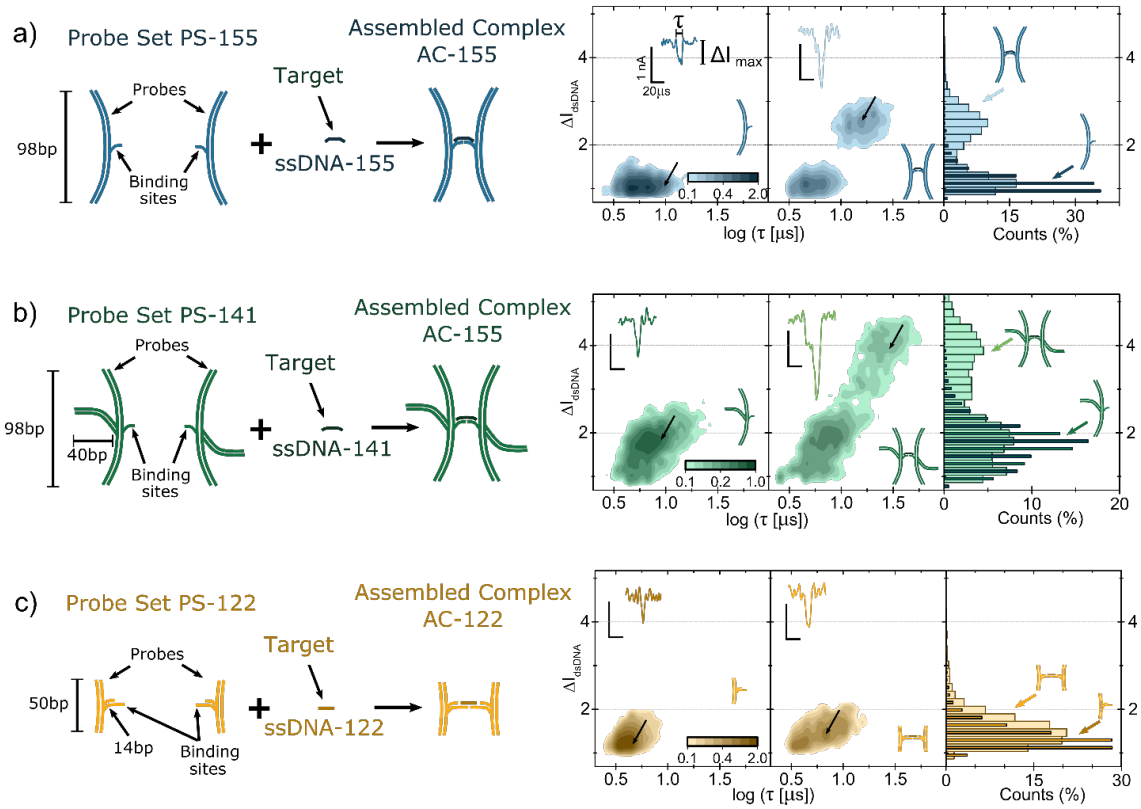

Figure 4.1. Schematic representation of three probe sets of various sizes and structures, with their associated assembled complexes formed in the presence of specific targets.

a) ssDNA-155, b) ssDNA-141 or c) ssDNA-122 serve as proxy sequences for their miRNA equivalents during preliminary testing. Density contours of smoothed scatterplots of ΔI_{dsDNA} versus τ for each probe set show a single population of shorter, shallower ionic current blockades than the population corresponding to the assembled complex in the presence of each respective target. Representative ionic current traces are shown as insets with a common scale bar, with each event shown in its corresponding contour plot with a black arrow.

The encouraging results obtained in distinguishing probe sets and their corresponding complex independently led to experiments in which mixtures of targets ssDNA-155 and -141 were detected simultaneously. Figure 4.2 shows histograms in which samples containing (a) neither target, (b) ssDNA-155, (c) ssDNA-141, and (d) both targets were incubated in equimolar ratios (55 nM) with PS-155 and PS-141 from

Figures 4.1a and 4.1b. As expected for the control sample lacking either target in Figure 4.2a, only two distinct blockages were present at ΔI_{dsDNA} = 1.1 and 1.8 corresponding to PS-155 and PS-141, respectively, as expected from the characterization data from Figure 4.1. In the mixture containing ssDNA-155 (Figure 4.2b), a population was present at a blockage depth of 2.6 with a corresponding drop in the peak associated with PS-155. Similarly, when ssDNA-141 is added in Figure 4.2c, a statistically significant number of events with $\Delta I_{dsDNA} > 2.6$ with a reduction in events identified as PS-141. When both targets were present (Figure 4.2d), counts associated with both probe sets were reduced, with peaks associated with both complexes appearing at the corresponding deeper blockage states.

Due to the relatively rapid translocation of PS-122 and AC-122 in Figure 4.1, the minor differences in ΔI_{dsDNA} and τ, as well as the near overlap of these parameters with those of the ssDNA-155 and -141 structures, higher order multiplexing of target identification was not realized with the nanopore sizes and electrical bandwidth used in this study. While the presence of incompletely formed and unreacted probes in the presence of equimolar targets complicated experimental results, preliminary attempts at simultaneous 3-plex target detection experiments are shown in Section 4.3.4, where histograms of ΔI_{max} from the translocation of all species could provide an ideal system for machine learning analysis algorithms.[124] The results presented in Figure 4.2 also provide an important proof-of-concept for the proposed use of assembled DNA structures as labels for multiplexed target detection using solid-state nanopores.[82,122] Importantly, the selectivity shown in probe sets forming complexed structures with only the appropriate sequence, even in the presence of competing targets and binding sites,

highlights the specificity of the assay. With further optimization of probe geometries for specific pore sizes and sample purification for removing incompletely formed probes, these results show potential for increased multiplexing ability with more narrowly defined distributions in blockage states at experimentally accessible bandwidths (~ 1 MHz).

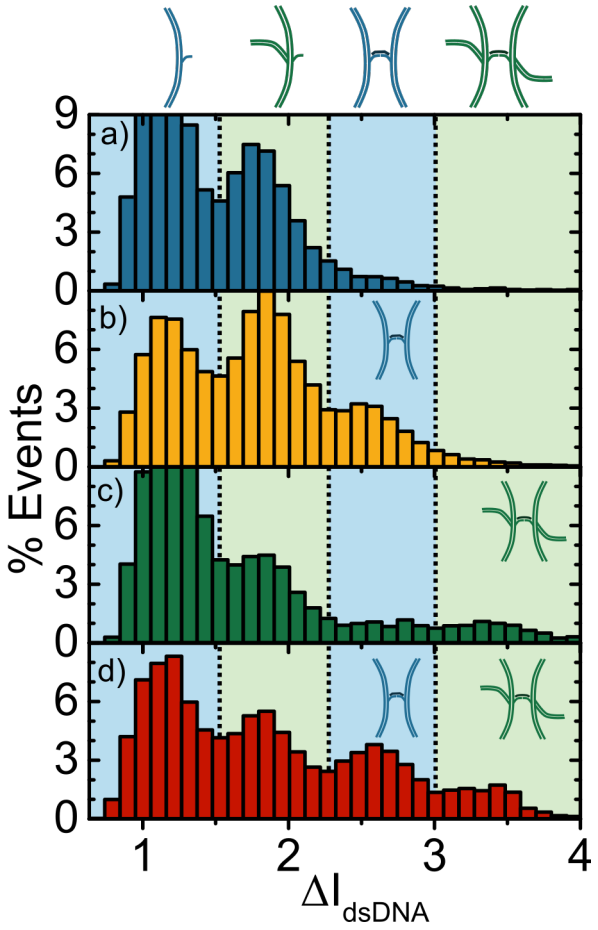

Figure 4.2. Simultaneous detection of ssDNA-155 and ssDNA-141 targets using probe sets PS-155 and PS-141, respectively.

Histograms of ΔI_{dsDNA} during translocation exhibit peaks corresponding to each unique species (top) in samples containing a) neither target (only probe sets), b) ssDNA-155, c) ssDNA-141, and d) both ssDNA targets. The high narrow peaks corresponding to linear probe sets are not entirely visible on this scale in (a) and (c), where ssDNA-155 was not present to consume probes.

While many nanopore-based methods of sample quantification rely on determining the capture rate of a particular species, this parameter can be highly variable between experiments even with nanopores of the same nominal geometry.[125] On the other hand, the ability to accurately account for probe molecules provides a benchmark with which to compare the relative number of branched structures upon conjugation with a target, allowing for a digital counting approach for accurate target quantification that is independent of individual nanopore properties that can affect capture rate.[126] Of the three structures examined, the linear PS-155 (Figure 4.1a) best served as an internal calibration reference for the relative number of branched molecules. Moreover, the translocation of these probes through the nanopore led to sufficiently long dwell times (> 2.5 μs for the response time of the Chimera current amplifier with 4.17 MHz sampling low-pass filtered at 900 kHz – Section 4.3.3), a key aspect for accurate digital counting experiments in which every molecule can be referenced for concentration determination. As such, these probes were selected for miRNA quantification experiments. Validation tests comparing ssDNA-155 with miRNA-155 in Section 4.3.2 show a similar performance of linear probes for detecting both targets. While the equivalent ssDNA sequence resulted in a slightly higher fraction of total complex formation than with miRNA, this is likely due to the relatively weaker binding of RNA compared to DNA for the sequences used.[127]

Digital counting experiments were performed in which miRNA-155, a diagnostic biomarker for lung cancer,[128] was added in increasing molar ratios relative to a fixed concentration of probe molecules (55 nM). Relative molar ratios were increased in increments of 0.2 from 0 (a control sample containing only PS-155) to 1 (equimolar concentration of miRNA-155 and each probe of the set). Figure 4.3a shows histograms

ΔI_{dsDNA} for three representative samples containing target molar ratios of 0, 0.6, and 1, where $\Delta I_{dsDNA} < 2.1$ corresponds to single-file translocation signatures due to probes (the number of counts of which is denoted by N_{PS}). $\Delta I_{dsDNA} > 2.1$ indicates the translocation of assembled complexes AC-155 containing the miRNA-155 target (N_{AC}). A zoom of $\Delta I_{dsDNA} > 1.9$ is shown in Figure 4.3b for all ratios sensed using a single nanopore. While Gaussian fits of both peaks allow for an accurate estimation of the number of events in each population, this did not provide a significant difference from simply counting the ratio of N_{AC} to the total number of events N in Figure 4.3a, where N_{AC} was defined as the number of events with ΔI_{dsDNA} exceeding that of PS-155 plus 4.5 times the standard deviation, σ, of the PS-155 peak. Furthermore, while there is a slight deviation in the mean of the peaks associated with AC-155 in Figure 4.3b due to minor variations in pore conductance or ionic solution conductivity between experiments, determination of reaction yield was invariant between metrics.

In our assay, each miRNA target in a sample mixture consumed two probe molecules, resulting in a 2-fold reduction of probes detected by the nanopore. The yield of assembled complexes was therefore estimated as $N_{AC}/(N_{AC}+\frac{1}{2}N_{PS})$. This detected yield is shown as a function of the target molar ratio, given as the ratio of target molecules to each individual probe in a set, in Figure 4.3c. Upon linear increase of miRNA-155 for a fixed probe set concentration, we found that the formation of assembled complexes also rose approximately linearly, reaching a maximum of 40-60 % of the total potential amount of branched product depending on the method of quantification (nanopore ionic current recordings or agarose gel characterization). Above a molar ratio of 1, we found

that the yield of assembled complexes actually decreases as excess miRNA saturated binding sites (Section 4.3.2).

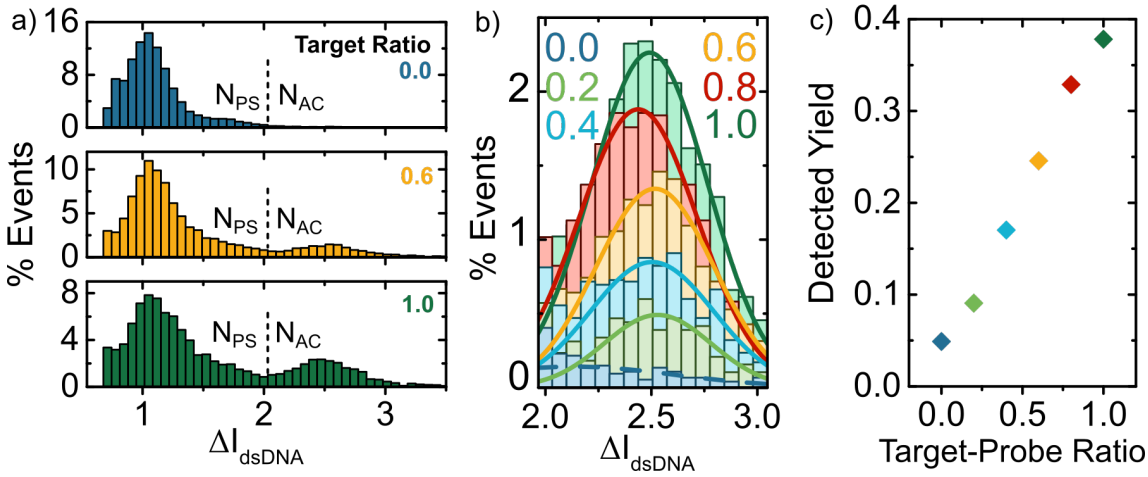

Figure 4.3. Nanopore characterization of assembled complex AC-155 formation for increasing miRNA-155 concentration.

a) Histograms of ΔI_{dsDNA} for three molar ratios of miRNA relative to PS-155 show an increasing number of translocation events with deep blockage levels N_{AC}. *Dashed lines in (a) are a guide to the eye showing the approximate location of $\Delta I_{PS\text{-}155} + 4.5\sigma$. b) A zoom of $\Delta I_{dsDNA} > 2$ from (a) for all ratios examined between 0 and 1 with overlaid Gaussian fits show an increase in* N_{AC} *with miRNA-155 concentration.* N_{AC} *values were used to compute the detected reaction yield (c), where counts in the peak corresponding to complexes are weighted as twice that of shallow linear blockades due to the stoichiometry of the assay components (two probes per assembled complex).*

We were able to differentiate at least six different relative concentrations of miRNA-155 for a fixed probe concentration before saturation of the reaction. While this linear dose response demonstrates a high degree of precision over a target concentration range spanning a single order of magnitude, the nature of the digital relative counts-based assay enables miRNA quantification over a much broader range with high sensitivity through tuning of the probe concentration. For instance, to measure diagnostically

relevant miRNA-155 concentrations, one could perform this assay with PS-155 concentrations in the pM range. In the absence of parallelization, amplification, enrichment, or capture rate enhancement schemes, this would result in a corresponding increase in experimental time to acquire sufficient statistics. To shed some light on the TTR for such an assay, we explored the number of events required to accurately identify the concentration of miRNA-155 in each sample from Figure 4.3. Figure 4.4 shows the fraction of total events with $\Delta I_{dsDNA} > 2.1$, N_{AC}, as a function of the cumulative number of events detected N. Coloured bands indicate the bounds corresponding to a 95 % confidence interval around each mean N_{AC}/N as each new event is acquired.[83] In this case, distinguishing samples with increments of 0.2 in relative target concentration with 95% confidence required a maximum total count of ~ 1300 single-molecule events, indicated by vertical lines with a single asterisk in Figure 4.4. Discerning samples with 99% confidence required ~ 3000 events, as indicated by the double asterisks (further detail in Section 4.3.5).

At the minimum observed capture rate of ~0.1 Hz per nM (i.e. ~10 Hz capture rate for 55 nM probes) for these probe molecules under these specific operating conditions (nanopores 7 - 10 nm in diameter, applied voltage biases of 100 mV – 200 mV and 2.0 M LiCl buffered to pH 8.0), counting the requisite 3000 translocation events for 99 % confidence required ~ 5 minutes. If less precision is required, the TTR is significantly reduced. For instance, resolving 40 % change in miRNA-155 concentration relative to that of probes (e.g. distinguishing the 0.2 from the 0.6 molar ratio samples) required < 500 events for the experiments shown in Figure 4.4, or < 1 minute. A simple qualitative determination of the presence of a target using the appropriate probe

concentration, on the other hand, can be obtained in just a few seconds with tens of molecules. This single-molecule sensing platform thus presents an attractive alternative to conventional gel electrophoresis assays which typically rely on the presence of at least nanograms of genetic material.[129,130]

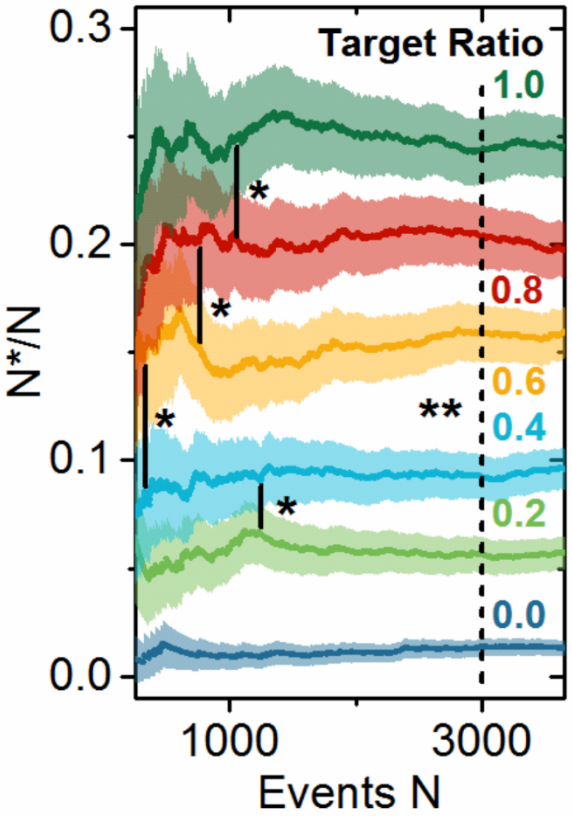

Figure 4.4. Fraction of events exhibiting ΔI_{dsDNA} > 2.1 as a function of the total number of events detected for each target ratio studied.

Dark lines show the mean of each sample, while the colored bands represent a 95 % confidence interval. Once bands do not overlap, samples are considered resolved. Lines with single asterisks show the event number after which samples were resolved with 95 % confidence, while the dashed line with two asterisks at N = *3000 indicates resolution of bands with 99 % confidence (Section 4.3.5).*

4.1.3 Conclusions and Outlook

Nanopore sensing configurations using asymmetric salt gradients,[31] and control of electro-osmotic[84] and fluid flow in confined device geometries[85] could offer a combined ~100-fold capture rate enhancement, suggesting that this assay could provide accurate miRNA quantification from ~ 10 pM – 10 μM in less than 1 hr of nanopore recording time. While this is reasonable considering the typical experimental lifetime and performance of solid-state nanopores, depending on the precision required and permissible experiment time for a particular assay, this concentration range could be further extended. Exploring such a broad range of unknown target concentrations could be practically realized by sensing solutions containing probe molecules spanning several orders of magnitude of concentration in parallel using an array of nanopores[78] (or sensed sequentially using the same nanopore), yielding a quantifiable amount of probes complexed with miRNA in the appropriate sample. Refinement of miRNA quantification could then be performed using a probe concentration in the appropriate range following the procedure outlined in Figure 3.

In addition to the assembled molecules presented in this work, other possibilities exist for forming DNA nanostructures[131] which could allow for a higher degree of multiplexing and be suitable for different nanopore sizes and geometries, such as those formed in 2D materials[25] or glass nanopipettes.[22] In addition to the high degree of precision achieved with the digital relative counts-based method for miRNA quantification, the similarities in results observed for ssDNA and miRNA targets also shows promise for the development of novel target detection assays and rapid screening

of potentially viable miRNA targets for diagnostic purposes using inexpensive, readily available ssDNA proxies.

4.2 Experimental Methods

4.2.1 Nanopore fabrication

Following 30 s of air plasma treatment at 50 W, 13±2 nm thick SiN membranes (Norcada NBPX5004Z-100O) were painted with 10:1 polydimethylsiloxane to reduce electrical noise in high-bandwidth recordings.[132] Nanopores were fabricated in 3D-printed flow cells (~20 uL reservoir volumes)[133] using the CBD method[24], followed by enlargement and conditioning[44] in 1 M KCl before equilibration in 3.6 M LiCl for at least 1 hr (all solutions were HEPES-buffered to pH 8.0 ± 0.1). Open pore conductance recordings as well as control experiments with 500 bp dsDNA were used to infer experimental pore sizes as previously described.[81] Nanopores used in this study were 7–10 nm in diameter with effective thicknesses of 9-12 nm.

4.2.2 Sample preparation

All DNA and RNA sequences were purchased from Integrated DNA Technologies (sequences in Section 4.3.1). Scaffold sequences were inspired by the work of David Lilley[134] with the goal of minimizing undesirable base mismatching and branch migration at DNA origami junctions. All samples were prepared in Mg-TAE pH 8.0 (12.5 mM magnesium acetate, 40 mM Tris, 20 mM acetic acid, 2 mM EDTA), with primary and secondary probe molecules assembled separately by heating the appropriate

oligomers (5 μM each) to 70 °C, followed by cooling at -1 °C per minute in a thermocycler. Branched complexes were formed by incubating target miRNA or ssDNA molecules at the indicated relative molar ratio with 100 nM aliquots of probes for at least 1 hr at room temperature. Complex formation was characterized by 2 % agarose gel electrophoresis in 1X TAE run at 70 V for ~ 2 hrs in an ice bath. Samples were stored at 4 °C until nanopore sensing experiments at 55 nM probe concentrations in 3.6 M LiCl buffered to pH 8.0, where 11 μL of each sample in TAE-Mg was added to 9 μL of 8 M LiCl to match the *trans* reservoir solution condition of 3.6 M LiCl buffered to pH 8.0.

4.2.3 Data acquisition and analysis

Ionic current recordings were acquired in MATLAB R2013a using a Chimera VC100 current amplifier sampling at 4.167 MHz with a 1 MHz 2-pole low-pass hardware Bessel filter. Event data was analysed at 900 kHz or 750 kHz following low-pass filtering at 900 kHz or 750 kHz, respectively, using the CUSUM+ algorithm.[89] Analysis parameters were otherwise chosen as described in Chapters 2 and 3.

4.3 Supporting Information

4.3.1 Molecular assembly

Sketches of the structures used in this this work are shown in Figure 4.5, roughly to scale with respect to one another. The corresponding sequences are shown in Table 4.1, which is roughly grouped by assembled complex structure. **Scaffold**, **3'-CompA** and **CompB-33mer** oligos are used in both PS- and AC-155, and PS- and AC-141.

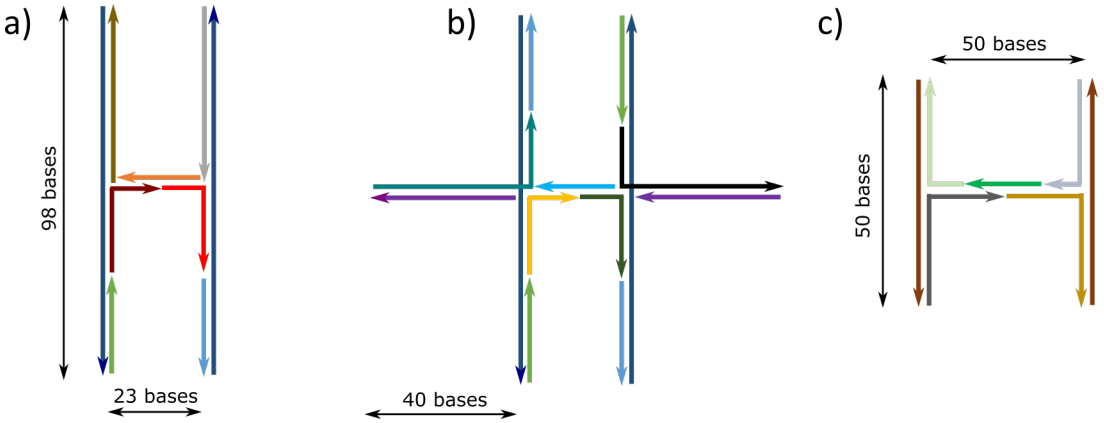

Figure 4.5. Schematic representations of assembled probe-target complexes.

Sketches correspond to targets miRNA-155 or ssDNA-155 (a), ssDNA-141 (b) and ssDNA-122 (c). Arrows representing the oligonucleotides point in the 3' to 5' direction, with the associated sequences in Table 4.1.

Table 4.1. Oligonucleotide sequences used to detect miRNA and ssDNA targets.

Sequences are grouped probe structure and corresponding target, colour-coded to match Figure 4.1.1. Where appropriate, some sequences were shared between structures in Figure 4.5a and 4.5b. RNA is denoted with lowercase 'r' before each base.

Name	Sequence (5'-3')	Length
miRNA-155	rUrUrArArUrGrCrUrArArUrCrGrUrGrArUrArGrGrGrGrU	40
ssDNA-155	TTAATGCTAATCGTGATAGGGGT	23
Scaffold	GGTGTGACTTGAATTTGCGGTCCTAAGTTGGTTCGTAATTGTGGTCATC GTGGCGTACCATATACCGCTTGTTGTATTCTAACACTGCATCTCATACG	98
5'-compA	ACAATTACGAACCAACTTAGGACCGCAAATTCAAGTCACACC	42
3'-compA	CGTATGAGATGCAGTGTTAGAATACAACAAGC	32
Overhang-A-155	GGTATATGGTACGCCACGATGACCTACCCCTATCAC	36
Comp-B-33mer	AACCAACTTAGGACCGCAAATTCAAGTCACACC	33
Overhang-B-155	GATTAGCATTAATCCACGATGACCACAATTACG	33
Comp-B-45mer	CGTATGAGATGCAGTGTTAGAATACAACAAGCGGTATATGGTACG	45
ssDNA-141	TAACACTGTCTGGTAAAGATGG	22
Overhang-A-141	GGTATATGGTACGCCATCCATCTTTACC	28
Overhang-B-141	AGACAGTGTTATCGATGACCACAATTACG	29
Branch-comp	CGTGCACATCGTCAGCATACGTACGCTACCTCGACCTGCG	40
A-branch	CGCAGGTCGAGGTAGCGTACGTATGCTGACGATGTGCACGTCGATGAC CACAATTACG	58
B-branch	GGTATATGGTACGCCATCGCAGGTCGAGGTAGCGTACGTATGCTGACG ATGTGCACG	57
ssDNA-122	TGGAGTGTGACAATGGTGTTTG	22
3-A-5'	AAGGACCAGGGAACGTATTTGCCTTGTCTGGGAAATCGT	39
3-AB	ACGATTTCCCAGACAAGGCAAATACCCAACTGGTTGTGGCCTATCGAA AA	50
3-A-3'	TTTTCGATAGGCCACAACCAGTTGGGTTCCCTGGTCCTTCAAACACCATT	50
3-B-5'	GTCACACTCCAAAGGACCAGGGAACGTATTTGCCTTGTCTGGGAAATC GT	50
3-B-3'	TTTTCGATAGGCCACAACCAGTTGGGTTCCCTGGTCCTT	39

4.3.2 Gel characterization of probe sets, assembled complexes and reaction mixtures.

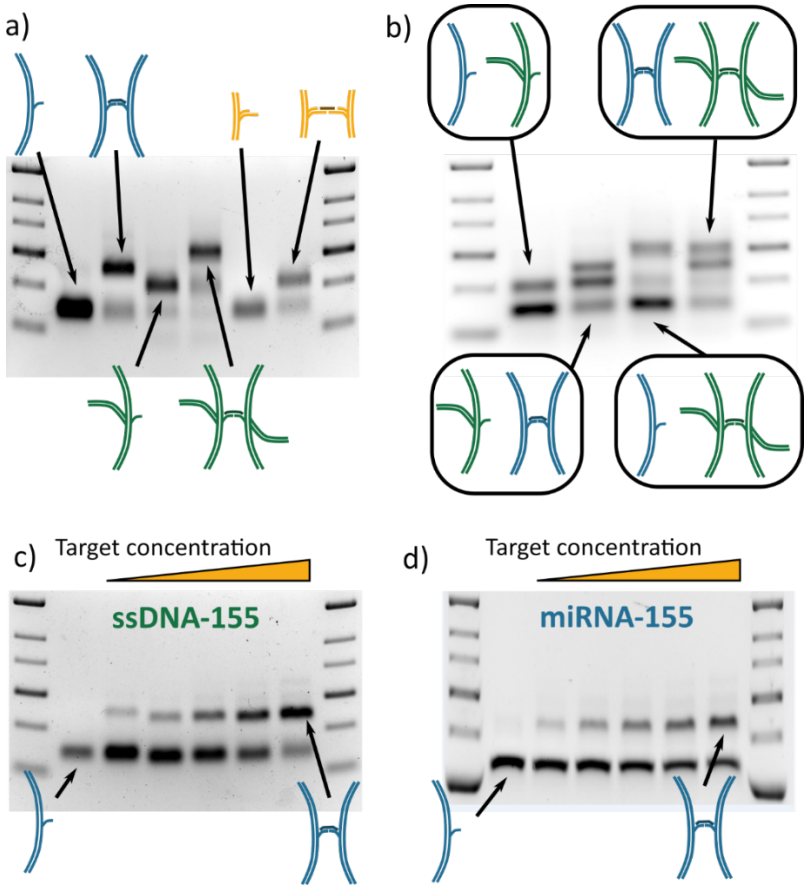

Figure 4.6. Gel characterisation of assembled molecules.

a) Probe sets and assembled molecules for the experiments shown in Figure 4.1. b) Sample mixtures for 2-plex detection shown in Figure 4.2. Dose response assays in which increasing concentrations of ssDNA-155 (c) and miRNA-155 hybridise to the same probe set. Figures 4.3 and 4.4 use the sample mixtures in (d). All assembled molecules were characterised by 2 % agarose gel electrophoresis with outer lanes containing a 1 kbp ladder. Relative intensities within each lane were quantified using GelBandFitter[86] as described in Section 2.2.3.

In addition to the gels shown in Figure 4.6, the dose response of miRNA-155 hybridization to linear probe sets was tested over different concentration ranges. Figure 4.7a shows an example reaction where molar excesses of target were added to a fixed

concentration of each probe. After reaching a maximum reaction yield of ~50%, a decline in assembled complexes is observed, as conjugation is prevented when binding sites become saturated with the miRNA target.

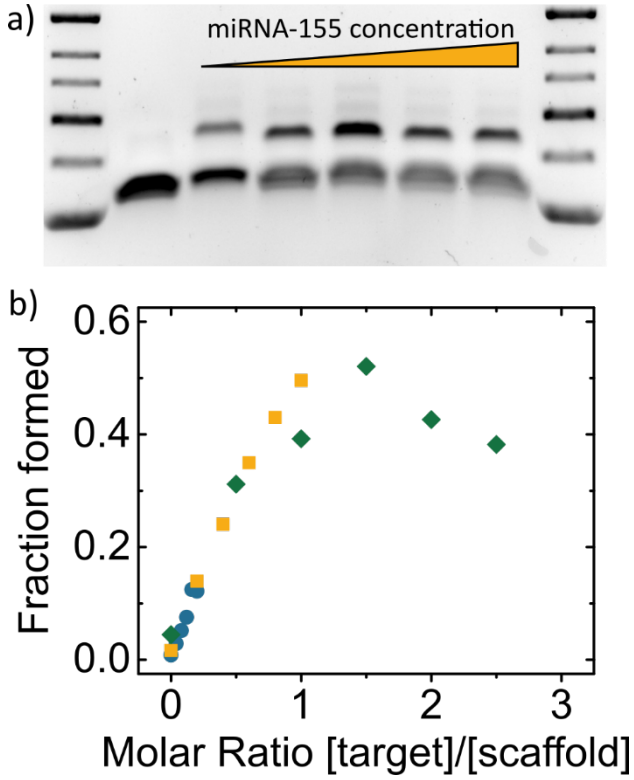

Figure 4.7. Effects of high miRNA concentration.

a) Agarose gel characterisation of a reaction in which target concentrations exceeded those of probe sets. The reaction yield of each mixture in (a) is shown as green diamonds in (b), where two other concentration ranges were also characterised. Yellow squares correspond to the gel shown in Figure 4.6d and the nanopore translocation data discussed in Figures 4.3 and 4.4.

4.3.3 Translocation characteristics assay components

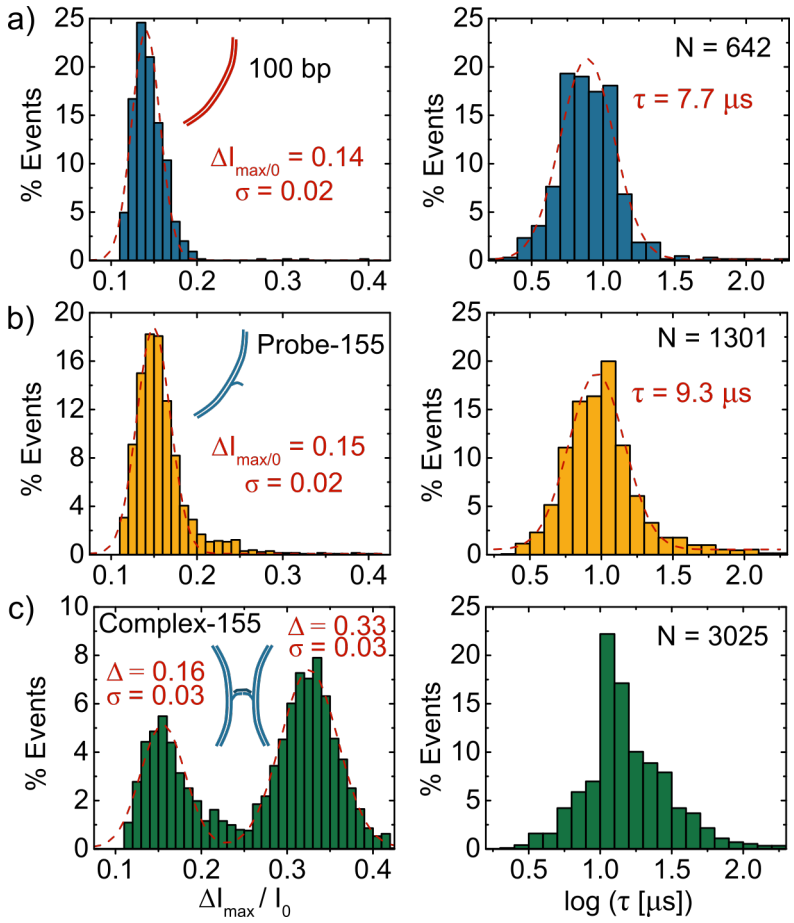

Figure 4.8. Histograms of ΔI_{max} relative to the open pore current I_0 and log(τ).

Histograms of ΔI_{max} relative to the open pore current I_0 and log(τ) for a) 100 bp fragments, b) PS-155, and AC-155 hybridized with ssDNA-155. Dashed red lines are Gaussian fits with indicated peak locations and standard deviations. The log(τ) histogram for the assembled complex was not fit due to the bimodal distribution of translocation events, as seen in Figure 4.1.

4.3.4 Preliminary 3-plex target detection

While Figure 4.2 shows the successful simultaneous detection of two different ssDNA targets, we also performed experiments in which all three probe sets were sensed simultaneously with the same nanopore. In this case, all samples from Figure 4.1 were prepared separately and mixed in equimolar ratios (assuming that the assembled complex of each corresponding probe set would be formed with 100 % yield, whether or not that target was actually in the sample mixture) immediately prior to addition to the sensing reservoir. Figure 4.9 shows histograms of the maximum blockage depth observed for three 3-plex experiments. Schematic insets show which species were added in each example, with arrows indicating the corresponding peaks (or lack of corresponding peaks) that can be used to identify which samples were present. Given the amount of unreacted probe sets, distinguishing the small 50-base branched scaffold was not possible in these reaction mixtures. However, the two larger assembled complexes could be identified by the presence or absence of peaks at deeper blockage depths.

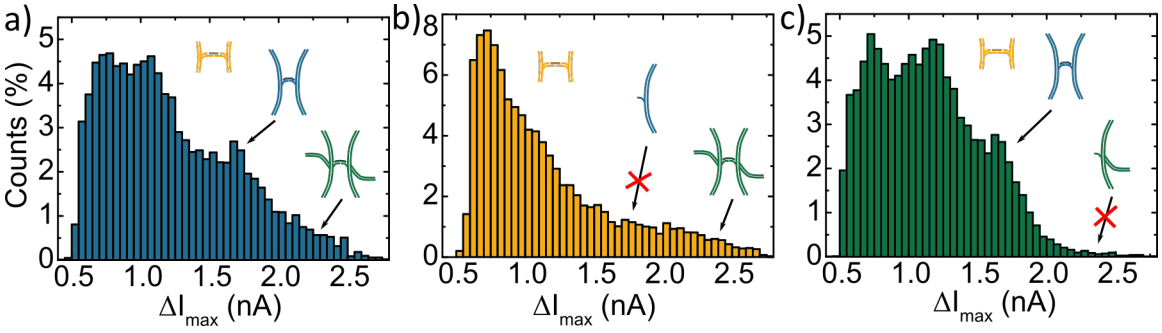

Figure 4.9. Preliminary 3-plex target detection experiments.

a) The assembled complex of each target yields a peak at deeper blockage depths to identify ssDNA-155 and ssDNA-141. The presence or absence of these peaks is also resolvable in samples where only one of those targets is in the sample mixture (b-c).

4.3.5 Statistical confidence of miRNA quantification

While Figure 4.4 shows 95 % confidence intervals around the mean for differentiating samples of increasing miRNA concentration, we also performed similar analysis using a 99 % confidence interval. Figure 4.10 shows a plot similar to Figure 4.4, but with lightly shaded regions around each mean corresponding to this stricter criterion. The number of events required to differentiate neighbouring concentrations is shown as dashed lines with two asterisks. As shown in Figure 4.4, all samples are distinguishable in fewer than 3000 events, except for the target ratios of 1.5 and 1.0.

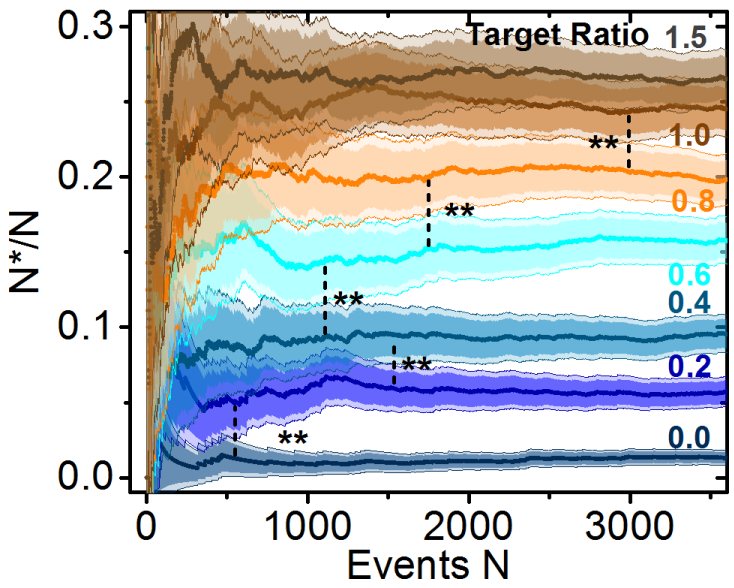

Figure 4.10. Statistical analysis of complex detection with two confidence intervals.

Similar to Figure 4.4, the mean number of assembled complexes detected as a function of the cumulative number of events is shown with dark shaded regions representing a 95% confidence interval. Lightly shaded regions correspond to a 99% confidence interval, with dashed lines indicating where samples containing similar miRNA to probe ratios were resolved with this stricter criterion.

Chapter V.

Outlook

For a field whose mere conceptualisation has existed for only three decades, the length and number of strides that have been taken in nanopore-based single-molecule sensing have been extraordinary. While the initial aim of DNA sequencing has all but been solved for biological pores, there are still great distances yet to cover. Perhaps lagging their biological counterparts in nucleic acid sequencing, solid-state nanopores offer an attractive alternate long-term solution as a sequencing platform, with the ability to address many other open questions in physics and medical diagnostics. However, to be truly useful in a clinical setting, several issues still need to be resolved, particularly where reliability and miniaturisation are concerned.

5.1 Open Challenges

5.1.1 Reliability

To be practically useful in a clinical setting, solid-state nanopores must display repeatable, consistent performance. Despite the success of the fabrication method used for experiments in this thesis, nanopores fabricated by CBD, as well as those produced by other methods discussed in Chapter 1, can still suffer from the drawbacks of inconsistency and instability. Inherent in their ability to detect individual molecules is the sensitivity to single-atom or -charge differences in nanopore surfaces that can introduce

variability in behaviour. Despite relatively low dissolution rates of the solid-state materials used to form nanopores, even the slightest hint of this effect can produce significant changes in performance.[135]

Further complicating reliable point-of-care testing is the fact that small changes in surface charge or geometry can result in drastically different capture rates, making it challenging to determine molecular concentrations. Practically speaking, this results in a high degree of pore-to-pore variability, meaning that experiments performed using different hand-held devices or disposable cartridges by a patient's bedside could yield inconsistent results. Furthermore, such variations in translocation properties can be observed with the same nanopore over the course of its lifetime. The approaches discussed in Chapters 2-4, as well as recent work in the Tabard-Cossa lab at the University of Ottawa,[126] present one approach to on-the-fly calibration that uses an internal concentration standard for improved analyte concentration determination. While this could theoretically be used to bypass the need for separate calibration experiments which run the risk of exhausting the usable lifespan of a nanopore and involve more complicated sample introduction and manipulation, further characterisation of such assays using diagnostically relevant samples need to be experimentally demonstrated before this promise can be delivered upon.

One of the main drawbacks of solid-state nanopores when compared to the biological variety is the presence of relatively high noise. This particular platform typically exhibits greater noise over the entire frequency spectrum, the sources of which are discussed in Chapter 1. While the rise in electrical noise as the square of frequency at high bandwidths is relatively well understood, achieving the SNR necessary for

applications such as DNA or protein sequencing, which require a high degree of temporal resolution, is still an open problem. Unfortunately, the phenomenon of low frequency $\frac{1}{f}$ noise is much less understood. Despite the success of treatment with high electric fields, a non-trivial fraction of nanopores continue to be discarded when exhibiting high $\frac{1}{f}$ noise, as they are practically unusable in sensing experiments. Figure 5.1, adapted from the thesis of Dr. Kyle Briggs, reiterates the amount of variability in noise between nanopores, which at present hinders the robustness and reliability of the platform for commercial diagnostic devices.

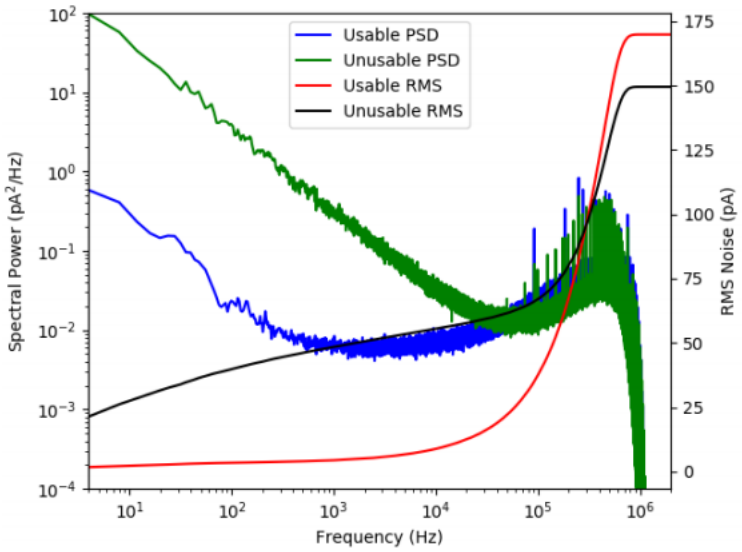

Figure 5.1. Power spectra of two different nanopores with dramatically different noise properties.

Similarly prepared nanopores show drastically different low frequency noise properties, with the high-noise pore (green and black) being unusable for experiment, despite lower RMS noise at high bandwidths than an example of a functional nanopore (blue and red). Green and blue curves correspond to the power spectrum (left axis), while black and red curves correspond to the RMS noise (right axis). Image reproduced with permission from the University of Ottawa.[136]

Despite these challenges, the future does indeed look bright for solid-state nanopores, as solutions to many of these issues either already exist or are the subject of promising ongoing research. For instance, the variability in noise between nanopores can all but be avoided by generating arrays of sensors. With access to hundreds of nanopores within a single device, the presence of a minority of nanopores with a high degree of noise is practically a non-issue, as those with desirable noise properties can be used for sensing without sacrificing valuable sample or time on poorly performing nanopores. Figure 5.2 shows an example in which both CBD and conditioning with high electric fields were performed by a prominent group in the nanopore field to produce an array of over a hundred nanopores in a single device.[137] In addition to providing a plethora of nanopores, the use of a micropipette to highly localise electrolyte contact with the membrane shows promise for mitigating electrical noise during high-bandwidth sensing. The parallelised sensing of samples using such arrays could also provide statistical power for reducing the effects of individual nanopore geometries and surface properties discussed above.

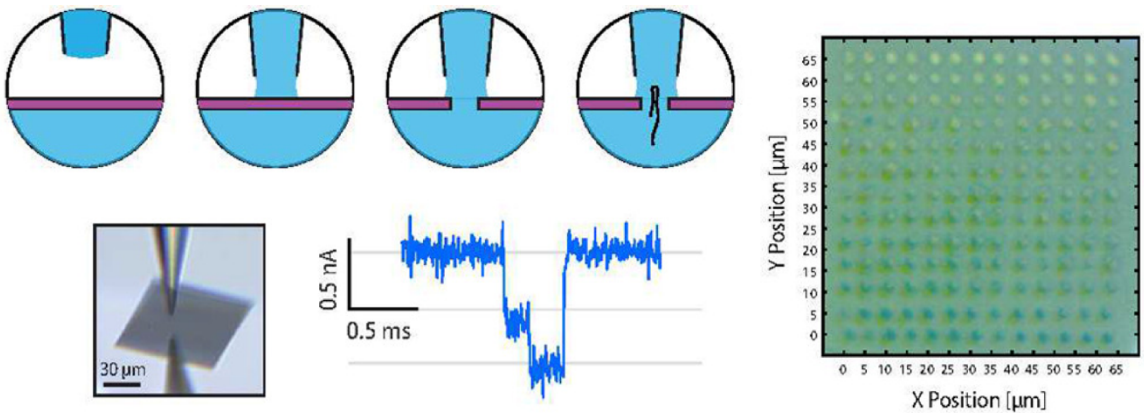

Figure 5.2. Nanopore array fabrication with CBD using micropipettes.

(Left) Schematic overview and microscope image depicting a micropipette with its tip forming a liquid contact to a SiN_x membrane. A nanopore is formed within the meniscus area and used for single-molecule experiments. (Right) An image of membrane and remaining contact residues after completing 169 automated sequential experiments, of which an example ionic current trace is shown (bottom-centre). Figure reproduced with permission from ACS Nano.[137]

5.1.2 Ease-of-use

It is perhaps naïve to assume that, despite the relative ease with which nanopores were fabricated for the experiments presented in this thesis compared to those generated by TEM, the expertise acquired in developing CBD protocol and the subsequent treatment with high electric fields translates directly to the fabrication of well-performing nanopores in industrial and clinical settings. There is still a need to develop these techniques to the point that they are sufficiently simple and straightforward for a non-expert in the field to fabricate nanopores and perform the necessary sensing and analysis to obtain results in an automated fashion. Ongoing research at the University of Ottawa has this goal in mind with the development of a platform with which, following the mounting of a thin solid-state membrane, functional nanopores could be fabricated with a single click of a mouse button. Figure 5.3 shows an example of relatively-state-of-the-

art fabrication workflow, whereby multiple TEM membrane windows can be mounted in custom 3D-printed flow cells containing microlitre-sized channels for electrolyte and sample addition.[133] Once a cell is added to the Fabrication and Sensing unit in Figure 5.3b, simply closing the appropriate one of two lids, each of which contains electrodes for electrical contact with the appropriate reservoirs, allows for either procedure to be performed in an automated fashion. While Figure 5.3 shows a prototype cell that is reusable for new membrane windows after nanopore lifetimes expire, there is currently some very exciting research in the Tabard-Cossa lab aimed towards the development of disposable cartridges that almost eliminate the need for user interference. Accompanying software is also under development that hides most if not all the back-end fabrication and sensing detail for optimal nanopore performance with little-to-no user intervention, ultimately promising to be useful in clinical settings.

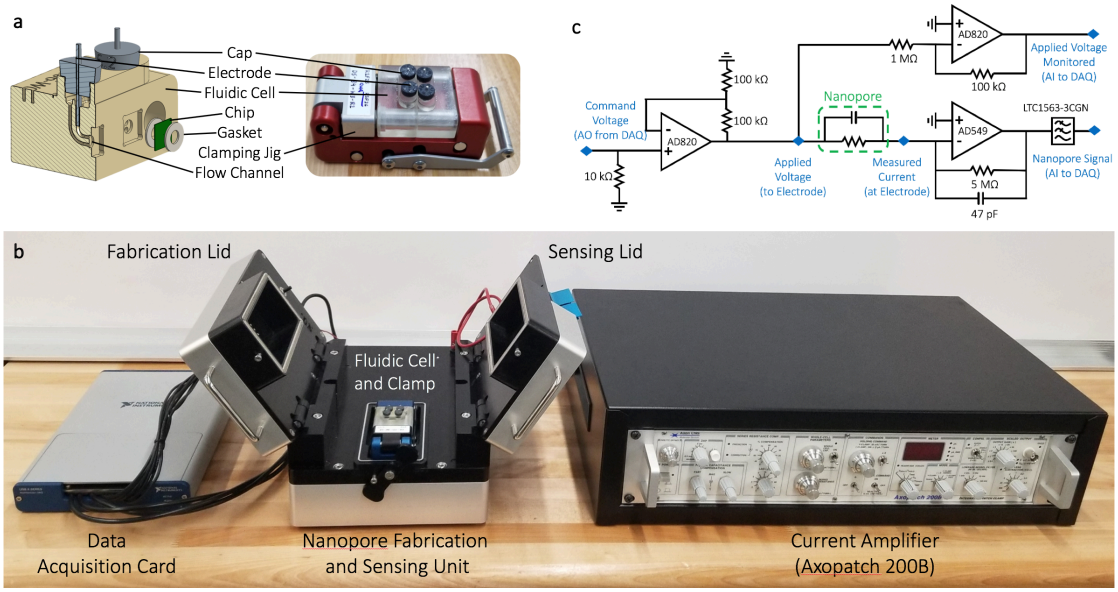

Figure 5.3. Overview of hardware for single-click multiple nanopore fabrication

(a) A schematic and real-world view of a flow cell design with ~20 µL volumes showing the flow channels and interface points for two-pore fabrication by CBD. (b) A custom Faraday cage with associated electronics (centre) interface with a commercially available DAQ card (left) and Axopatch 200B (right) for fabrication control and biomolecular sensing. c) Schematic diagram of the circuitry used for nanopore fabrication. A full diagram will be available in an upcoming article.[133]

5.2 Miniaturisation

Primary among the goals of nanopore research for use in clinical settings is the development of portable hand-held devices that could be operated by a non-expert, such as a doctor, nurse or technician. While the automation of nanopore fabrication discussed in the previous section will go a long way towards this goal, practical applications will inevitably require sample manipulation and preparation in addition to sensor calibration.

To this end, a great deal of focus has been dedicated in recent years to the development of lab-on-a-chip platforms for biomolecular sensing. While realisation of Star Trek's tricorder may still be decades away, nanopore-based hand-held devices have

recently experienced a surge in popularity. Perhaps the most commercially successful to date is Oxford Nanopore's MinION device, which among other accolades, brands itself at the time of this writing as the only portable real-time device for DNA and RNA sequencing. With hundreds of biological nanopores within a single hand-held device, this technology has effectively solved the challenge of long-genome sequencing, with quite literally out-of-this-world demonstrations of its functionality being performed on board the International Space Station.[10] On the solid-state side of commercial nanopore systems, devices by Ontera have also proven capable of protein detection and quantification using a hand-held device that incorporated nanopores within disposable strips.[115]

Availing themselves of the unique physics that take place at small scales, such microfluidic devices show not only great promise minimising precious sample volumes required for analysis, but also offer sample manipulation capabilities for purification and sample processing prior to actual nanopore sensing.[138] As an example, Figure 5.4 shows a device in which the product of a polymerase chain reaction was purified from reaction mixtures for subsequent analysis with a solid-state nanopore fabricated using an electron beam. While this study showed a high degre of on-chip functionality, our lab has been working in parallel on the development of similar devices for purification and pre-concentration of dilute analytes for subsequent nanopore sensing in a more streamlined fashion.

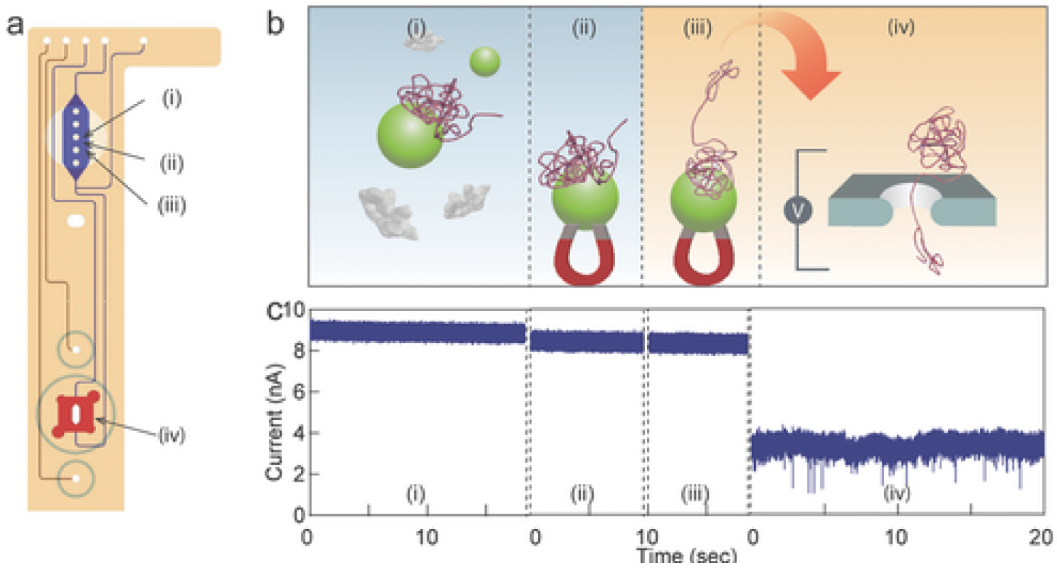

Figure 5.4. On-chip PCR product purification and sensing with TEM-drilled nanopores

a) Diagram of a nanopore–microfluidic chip. b) Schematic representation of on-chip magnetic-bead-based purification of a PCR amplicon. c) Representative electrical current measured during each step of purification in (b), including nanopore sensing of the purified product. Image adapted with permission from Advanced Functional Materials.[138]

With the emergence of CBD as a method of generating highly functional nanopores, our lab has also focused in recent years on the incorporation of solid-state nanopores within microfluidic devices formed from polydimethylsiloxane (PDMS).[78] While the integration of TEM-drilled nanopores within microfluidic channels has proved challenging in the past due to low yields and the difficulty associated with properly aligning pre-drilled nanopores within microscale channels, the CBD method provides the advantage of post-device assembly nanopore fabrication in an aqueous environment for immediate biomolecular sensing. Figure 5.5. shows an example of a device that contains five channels, each of which is independently addressable both fluidically and electrically.[95] Each microchannel spans a single membrane window, the upshot of which

is the ability to fabricate five different nanopores that can be used in a variety of different assay configurations. Particularly useful in this example is the multilayer nature of the device, whereby the addition of microvalves provides the ability to isolate regions of the membrane for either or serial or parallel sensing. This also allows for the sequestering of samples for pre-processing applications or independent biomolecular sensing experiments. In addition to providing a high degree of nanopore localisation on the SiN_x membrane, the use of microscale *vias* shown in Figure 5.5b limits membrane exposure to electrolyte to reduce electrical noise for improved nanopore performance.

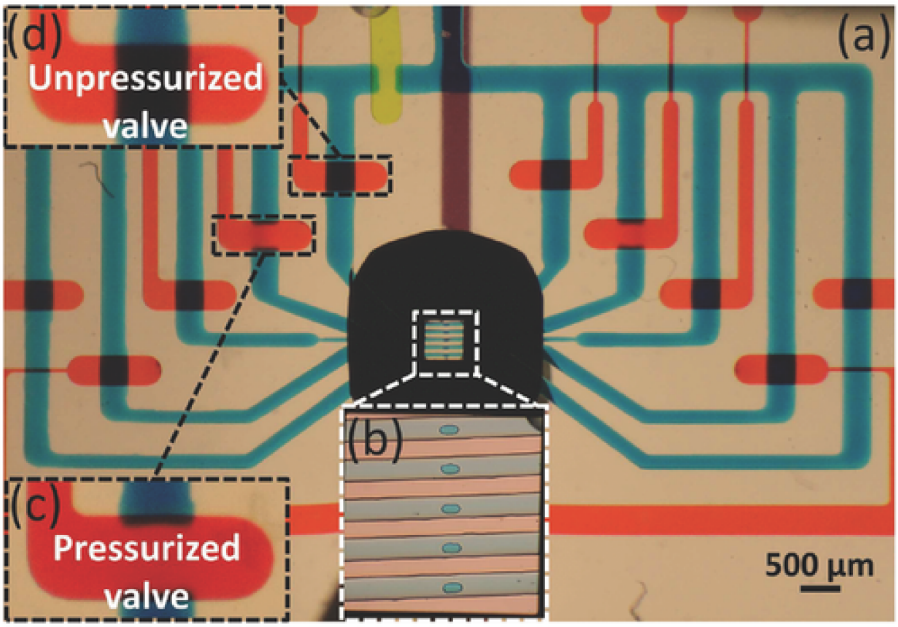

Figure 5.5 Microfluidic device containing five nanopores formed by CBD.

(a) A microscope image of a device containing five microchannels that cross a single SiN_x membrane window. (b) Microvias provide the only point of contact between electrolyte and the membrane window for highly localised nanopore formation and noise reduction. Microvalves can be pressurised (c) or depressurised (d) to manipulate electrical and fluidic access to each nanopore. Image reproduced with permission from Small.[95]

Despite the impressive results obtained by integrating nanopores within lab-on-a-chip devices, there is still a lot to be learned about how these sensors behave in microfluidic environments. For instance, fabrication by CBD initially proved to be much more challenging in PDMS channels than in macroscopic flow cells. Quite fortuitously, it was only through the addition of microvias (microscale conduits connecting nanopores and microfluidic channels) such as those shown in Figure 5.5b that biomolecules were first reliably sensed. Further investigation revealed that the symmetry of the electric field produced in these structures may play a crucial role in determining device functionality, an observation so cryptic that it led to a patent protecting the idea.[139] More recently, our lab has also discovered that the ubiquitous flow in microfluidic channels can not only have an effect on translocation properties, but that capture rates can be tuned to achieve almost an order of magnitude increase for more rapid data acquisition and biomolecular characterisation through the competitive effects of electrophoresis, diffusion and convection.[85]

5.3 Outlook: Advanced biomarker detection assays

The astonishing pace with which the nanopore sensing field has grown in recent years has certainly raised the expectations of the scientific community for novel discoveries made with this platform. Emerging from the awe surrounding the sensing individual molecules are now almost routine reports of genetic disease biomarker detection[83] and protein characterization.[140] Despite this, the challenges associated with solid-state nanopore sensing remain speed bumps in our path that we continue to navigate.

Very much in line with the themes presented in this work is some very exciting ongoing research in the laboratory of Dr. Tabard-Cossa at the University of Ottawa. Schematically shown in Figure 5.6, a disease biomarker detection assay is being developed that, while not overly resembling the Plan that we set out to achieve, effectively bypasses many of the challenges that we encountered over the years in trying to realise it. Particularly elegant is the solution to translating a potentially problematic analyte, such as a protein or antibody, to a purely DNA-based signal for nanopore sensing. Similar to the work presented in Chapter 4, two separate binding events occur in the presence of an analyte molecule. Using a magnetic bead, the analyte bound to a nanoparticle containing a DNA labels is removed from a complex sample mixture that may otherwise foul a nanopore. Following a cleavage step, DNA labels are released for subsequent nanopore detection. Built into this assay is a natural amplification step, where up to thousands of DNA labels could be sensed for every analyte molecule, ultimately allowing for the detection of extremely low concentrations of diagnostically relevant biomarkers in a patient sample. Utilising the ability of nanopores to detect molecules containing features along even very short DNA scaffolds, as shown in Chapter 3, unique label structures could be designed to ensure accurate counting for quantification, or even to enable multiplexed assays.

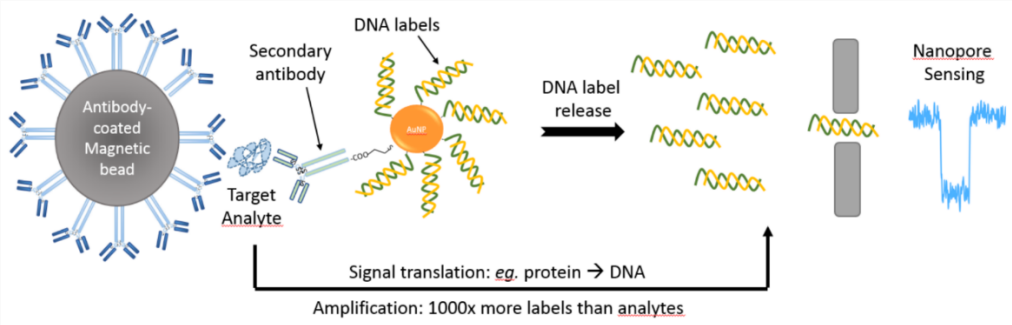

Figure 5.6. Disease biomarker detection assay with signal translation and amplification.

A sandwich assay in which a target analyte of interest is bound to a magnetic bead and nanoparticle coated with DNA labels allows for sample purification. Release of labels following purification provides a purely DNA-based signal for nanopore detection. In this example, a 6x amplification would be observed, as six labels are released for each analyte in the sample. Careful design of label structures could allow for analyte quantification with 1000s of times signal amplification. This figure was adapted from an original image by post-doctoral fellow Dr. Dan Tessier of the laboratory of Dr. Tabard-Cossa at the University of Ottawa.

As the field of nanopore sensing rapidly advances into its fourth decade, with reports of exciting new applications and miniaturised platforms appearing to arise on a weekly basis,[141] the opportunities truly appear limitless. While it may seem at first glance that the challenges facing our platform are engineering in nature, our recent investigations also hint at the existence of important physical discoveries on the horizon. And so, while the completion of this thesis represents the closing of one particular chapter of nanopore research, it is with great enthusiasm and optimism that the torch is passed on in the hope that the knowledge gained and the discoveries still to be made can, one day, help to realise the promise of the Plan.

References

(1) Deamer, D.; Akeson, M.; Branton, D. Three Decades of Nanopore Sequencing. *Nature Biotechnology* **2016**, *34* (5), 518–524. https://doi.org/10.1038/nbt.3423.

(2) Wanunu, M. Nanopores: A Journey towards DNA Sequencing. *Physics of Life Reviews* **2012**, *9* (2), 125–158. https://doi.org/10.1016/j.plrev.2012.05.010.

(3) Bezrukov, S. M.; Vodyanoy, I.; Parsegian, V. A. Counting Polymers Moving through a Single Ion Channel. *Nature* **1994**, *370* (6487), 279–281. https://doi.org/10.1038/370279a0.

(4) Kasianowicz, J. J.; Brandin, E.; Branton, D.; Deamer, D. W. Characterization of Individual Polynucleotide Molecules Using a Membrane Channel. *Proc. Natl. Acad. Sci. U.S.A.* **1996**, *93* (24), 13770–13773. https://doi.org/10.1073/pnas.93.24.13770.

(5) Akeson, M.; Branton, D.; Kasianowicz, J. J.; Brandin, E.; Deamer, D. W. Microsecond Time-Scale Discrimination among Polycytidylic Acid, Polyadenylic Acid, and Polyuridylic Acid as Homopolymers or as Segments within Single RNA Molecules. *Biophys. J.* **1999**, *77* (6), 3227–3233. https://doi.org/10.1016/S0006-3495(99)77153-5.

(6) Meller, A.; Nivon, L.; Brandin, E.; Golovchenko, J.; Branton, D. Rapid Nanopore Discrimination between Single Polynucleotide Molecules. *Proc Natl Acad Sci U S A* **2000**, *97* (3), 1079–1084.

(7) Meller, A.; Nivon, L.; Branton, D. Voltage-Driven DNA Translocations through a Nanopore. *Phys. Rev. Lett.* **2001**, *86* (15), 3435–3438. https://doi.org/10.1103/PhysRevLett.86.3435.

(8) Burton, B.; Dubnau, D. Membrane-Associated DNA Transport Machines. *Cold Spring Harb Perspect Biol* **2010**, *2* (7), a000406. https://doi.org/10.1101/cshperspect.a000406.

(9) Cherf, G. M.; Lieberman, K. R.; Rashid, H.; Lam, C. E.; Karplus, K.; Akeson, M. Automated Forward and Reverse Ratcheting of DNA in a Nanopore at Five Angstrom Precision. *Nat Biotechnol* **2012**, *30* (4), 344–348. https://doi.org/10.1038/nbt.2147.

(10) Castro-Wallace, S. L.; Chiu, C. Y.; John, K. K.; Stahl, S. E.; Rubins, K. H.; McIntyre, A. B. R.; Dworkin, J. P.; Lupisella, M. L.; Smith, D. J.; Botkin, D. J.; et al. Nanopore DNA Sequencing and Genome Assembly on the International Space Station. *Scientific Reports* **2017**, *7* (1), 18022. https://doi.org/10.1038/s41598-017-18364-0.

(11) Shi, W.; Friedman, A. K.; Baker, L. A. Nanopore Sensing. *Anal. Chem.* **2017**, *89* (1), 157–188. https://doi.org/10.1021/acs.analchem.6b04260.

(12) Li, J.; Stein, D.; McMullan, C.; Branton, D.; Aziz, M. J.; Golovchenko, J. A. Ion-Beam Sculpting at Nanometre Length Scales. *Nature* **2001**, *412* (6843), 166–169. https://doi.org/10.1038/35084037.

(13) Li, J.; Gershow, M.; Stein, D.; Brandin, E.; Golovchenko, J. A. DNA Molecules and Configurations in a Solid-State Nanopore Microscope. *Nature Materials* **2003**, *2* (9), 611–615. https://doi.org/10.1038/nmat965.
(14) Beamish, E. Precise Size Control and Noise Reduction of Solid-State Nanopores for the Detection of DNA-Protein Complexes. Thesis, Université d'Ottawa / University of Ottawa, 2012. http://dx.doi.org/10.20381/ruor-6246.
(15) Karhanek, M.; Kemp, J. T.; Pourmand, N.; Davis, R. W.; Webb, C. D. Single DNA Molecule Detection Using Nanopipettes and Nanoparticles. *Nano Lett.* **2005**, *5* (2), 403–407. https://doi.org/10.1021/nl0480464.
(16) Wei, C.; Bard, A. J.; Feldberg, S. W. Current Rectification at Quartz Nanopipet Electrodes. *Anal. Chem.* **1997**, *69* (22), 4627–4633. https://doi.org/10.1021/ac970551g.
(17) Steinbock, L. J.; Bulushev, R. D.; Krishnan, S.; Raillon, C.; Radenovic, A. DNA Translocation through Low-Noise Glass Nanopores. *ACS Nano* **2013**, *7* (12), 11255–11262. https://doi.org/10.1021/nn405029j.
(18) Controllable Shrinking and Shaping of Glass Nanocapillaries under Electron Irradiation - Nano Letters (ACS Publications) https://pubs.acs.org/doi/10.1021/nl400304y (accessed May 22, 2019).
(19) Freedman, K. J.; Otto, L. M.; Ivanov, A. P.; Barik, A.; Oh, S.-H.; Edel, J. B. Nanopore Sensing at Ultra-Low Concentrations Using Single-Molecule Dielectrophoretic Trapping. *Nature Communications* **2016**, *7*, 10217. https://doi.org/10.1038/ncomms10217.
(20) Umehara, S.; Karhanek, M.; Davis, R. W.; Pourmand, N. Label-Free Biosensing with Functionalized Nanopipette Probes. *PNAS* **2009**, *106* (12), 4611–4616. https://doi.org/10.1073/pnas.0900306106.
(21) Gornall, J. L.; Mahendran, K. R.; Pambos, O. J.; Steinbock, L. J.; Otto, O.; Chimerel, C.; Winterhalter, M.; Keyser, U. F. Simple Reconstitution of Protein Pores in Nano Lipid Bilayers. *Nano Lett.* **2011**, *11* (8), 3334–3340. https://doi.org/10.1021/nl201707d.
(22) Bell, N. A. W.; Thacker, V. V.; Hernández-Ainsa, S.; Fuentes-Perez, M. E.; Moreno-Herrero, F.; Liedl, T.; Keyser, U. F. Multiplexed Ionic Current Sensing with Glass Nanopores. *Lab Chip* **2013**, *13* (10), 1859–1862. https://doi.org/10.1039/C3LC50069A.
(23) Lombardo, S.; Stathis, J. H.; Linder, B. P.; Pey, K. L.; Palumbo, F.; Tung, C. H. Dielectric Breakdown Mechanisms in Gate Oxides. *Journal of Applied Physics* **2005**, *98* (12), 121301. https://doi.org/10.1063/1.2147714.
(24) Kwok, H.; Briggs, K.; Tabard-Cossa, V. Nanopore Fabrication by Controlled Dielectric Breakdown. *PLOS ONE* **2014**, *9* (3), e92880. https://doi.org/10.1371/journal.pone.0092880.
(25) Kuan, A. T.; Lu, B.; Xie, P.; Szalay, T.; Golovchenko, J. A. Electrical Pulse Fabrication of Graphene Nanopores in Electrolyte Solution. *Appl. Phys. Lett.* **2015**, *106* (20), 203109. https://doi.org/10.1063/1.4921620.
(26) Carlsen, A.; Tabard-Cossa, V. Enhanced Stability of 2-Nm Nanopores Fabricated by Controlled Breakdown. *1st Annual Meeting, Biophysical Society of Canada* **2015**.

(27) Kwok, H.; Waugh, M.; Bustamante, J.; Briggs, K.; Tabard-Cossa, V. Long Passage Times of Short SsDNA Molecules through Metallized Nanopores Fabricated by Controlled Breakdown. *Advanced Functional Materials* **2014**, *24* (48), 7745–7753. https://doi.org/10.1002/adfm.201402468.
(28) Briggs, K.; Charron, M.; Kwok, H.; Le, T.; Chahal, S.; Bustamante, J.; Waugh, M.; Tabard-Cossa, V. Kinetics of Nanopore Fabrication during Controlled Breakdown of Dielectric Membranes in Solution. *Nanotechnology* **2015**, *26* (8), 084004. https://doi.org/10.1088/0957-4484/26/8/084004.
(29) Briggs, K.; Kwok, H.; Tabard-Cossa, V. Automated Fabrication of 2-Nm Solid-State Nanopores for Nucleic Acid Analysis. *Small* **2014**, *10* (10), 2077–2086. https://doi.org/10.1002/smll.201303602.
(30) Kowalczyk, S. W.; Wells, D. B.; Aksimentiev, A.; Dekker, C. Slowing down DNA Translocation through a Nanopore in Lithium Chloride. *Nano Letters* **2012**, *12* (2), 1038–1044. https://doi.org/10.1021/nl204273h.
(31) Wanunu, M.; Morrison, W.; Rabin, Y.; Grosberg, A. Y.; Meller, A. Electrostatic Focusing of Unlabelled DNA into Nanoscale Pores Using a Salt Gradient. *Nature Nanotechnology* **2010**, *5* (2), 160–165. https://doi.org/10.1038/nnano.2009.379.
(32) Kim, M. J.; Wanunu, M.; Bell, D. C.; Meller, A. Rapid Fabrication of Uniformly Sized Nanopores and Nanopore Arrays for Parallel DNA Analysis. *Advanced Materials* **2006**, *18* (23), 3149–3153. https://doi.org/10.1002/adma.200601191.
(33) Kim, M. J.; McNally, B.; Murata, K.; Meller, A. Characteristics of Solid-State Nanometre Pores Fabricated Using a Transmission Electron Microscope. *Nanotechnology* **2007**, *18* (20), 205302. https://doi.org/10.1088/0957-4484/18/20/205302.
(34) Kowalczyk, S. W.; Grosberg, A. Y.; Rabin, Y.; Dekker, C. Modeling the Conductance and DNA Blockade of Solid-State Nanopores. *Nanotechnology* **2011**, *22* (31), 315101. https://doi.org/10.1088/0957-4484/22/31/315101.
(35) Yanagi, I.; Akahori, R.; Hatano, T.; Takeda, K. Fabricating Nanopores with Diameters of Sub-1 Nm to 3 Nm Using Multilevel Pulse-Voltage Injection. *Sci Rep* **2014**, *4*, 5000. https://doi.org/10.1038/srep05000.
(36) Hall, J. E. Access Resistance of a Small Circular Pore. *The Journal of General Physiology* **1975**, *66* (4), 531–532. https://doi.org/10.1085/jgp.66.4.531.
(37) Carlsen, A. T.; Briggs, K.; Hall, A. R.; Tabard-Cossa, V. Solid-State Nanopore Localization by Controlled Breakdown of Selectively Thinned Membranes. *Nanotechnology* **2017**, *28* (8), 085304–085304. https://doi.org/10.1088/1361-6528/aa564d.
(38) Tabard-Cossa, V.; Trivedi, D.; Wiggin, M.; Jetha, N. N.; Marziali, A. Noise Analysis and Reduction in Solid-State Nanopores. *Nanotechnology* **2007**, *18*, 305505.
(39) Smeets, R.; Dekker, N.; Dekker, C. Low-Frequency Noise in Solid-State Nanopores. *Nanotechnology* **2009**, *20*, 095501.
(40) Smeets, R. M. M.; Keyser, U. F.; Dekker, N. H.; Dekker, C. Noise in Solid-State Nanopores. *PNAS* **2008**, *105* (2), 417–421. https://doi.org/10.1073/pnas.0705349105.

(41) Johnson, J. B. Thermal Agitation of Electricity in Conductors. *Phys. Rev.* **1928**, *32* (1), 97–109. https://doi.org/10.1103/PhysRev.32.97.
(42) Rosenstein, J. K.; Wanunu, M.; Merchant, C. A.; Drndic, M.; Shepard, K. L. Integrated Nanopore Sensing Platform with Sub-Microsecond Temporal Resolution. *Nature Methods* **2012**, *9* (5), 487–492. https://doi.org/10.1038/nmeth.1932.
(43) Bible Gateway passage: Genesis 1:3 - New International Version https://www.biblegateway.com/passage/?search=Genesis+1%3A3&version=NIV (accessed May 30, 2019).
(44) Beamish, E.; Kwok, H.; Tabard-Cossa, V.; Godin, M. Precise Control of the Size and Noise of Solid-State Nanopores Using High Electric Fields. *Nanotechnology* **2012**, *23* (40), 405301. https://doi.org/10.1088/0957-4484/23/40/405301.
(45) Beamish, E.; Kwok, H.; Tabard-Cossa, V.; Godin, M. Fine-Tuning the Size and Minimizing the Noise of Solid-State Nanopores. *Journal of Visualized Experiments* **2013**, No. 80. https://doi.org/10.3791/51081.
(46) Storm, A. J.; Chen, J. H.; Ling, X. S.; Zandbergen, H. W.; Dekker, C. Fabrication of Solid-State Nanopores with Single-Nanometre Precision. *Nat Mater* **2003**, *2* (8), 537–540. https://doi.org/10.1038/nmat941.
(47) Prabhu, A. S.; Freedman, K. J.; Robertson, J. W. F.; Nikolov, Z.; Kasianowicz, J. J.; Kim, M. J. SEM-Induced Shrinking of Solid-State Nanopores for Single Molecule Detection. *Nanotechnology* **2011**, *22*, 425302.
(48) Hout, M. van den; Hall, A. R.; Wu, M. Y.; Zandbergen, H. W.; Dekker, C.; Dekker, N. H. Controlling Nanopore Size, Shape and Stability. *Nanotechnology* **2010**, *21* (11), 115304. https://doi.org/10.1088/0957-4484/21/11/115304.
(49) Firnkes, M.; Pedone, D.; Knezevic, J.; Döblinger, M.; Rant, U. Electrically Facilitated Translocations of Proteins through Silicon Nitride Nanopores: Conjoint and Competitive Action of Diffusion, Electrophoresis, and Electroosmosis. *Nano Lett.* **2010**, *10* (6), 2162–2167. https://doi.org/10.1021/nl100861c.
(50) Plesa, C.; Kowalczyk, S. W.; Zinsmeester, R.; Grosberg, A. Y.; Rabin, Y.; Dekker, C. Fast Translocation of Proteins through Solid State Nanopores. *Nano Lett.* **2013**, *13* (2), 658–663. https://doi.org/10.1021/nl3042678.
(51) Freedman, K. J.; Bastian, A. R.; Chaiken, I.; Kim, M. J. Solid-State Nanopore Detection of Protein Complexes: Applications in Healthcare and Protein Kinetics. *Small* **2013**, *9* (5), 750–759. https://doi.org/10.1002/smll.201201423.
(52) Siwy, Z.; Trofin, L.; Kohli, P.; Baker, L. A.; Trautmann, C.; Martin, C. R. Protein Biosensors Based on Biofunctionalized Conical Gold Nanotubes. *J. Am. Chem. Soc.* **2005**, *127* (14), 5000–5001. https://doi.org/10.1021/ja043910f.
(53) Larkin, J.; Henley, R. Y.; Muthukumar, M.; Rosenstein, J. K.; Wanunu, M. High-Bandwidth Protein Analysis Using Solid-State Nanopores. *Biophysical Journal* **2014**, *106* (3), 696–704. https://doi.org/10.1016/j.bpj.2013.12.025.
(54) Wanunu, M.; Meller, A. Chemically Modified Solid-State Nanopores. *Nano Lett.* **2007**, *7* (6), 1580–1585. https://doi.org/10.1021/nl070462b.
(55) Yusko, E. C.; Johnson, J. M.; Majd, S.; Prangkio, P.; Rollings, R. C.; Li, J.; Yang, J.; Mayer, M. Controlling Protein Translocation through Nanopores with

Bio-Inspired Fluid Walls. *Nature Nanotechnology* **2011**, *6* (4), 253–260. https://doi.org/10.1038/nnano.2011.12.
(56) Skinner, G. M.; van den Hout, M.; Broekmans, O.; Dekker, C.; Dekker, N. H. Distinguishing Single- and Double-Stranded Nucleic Acid Molecules Using Solid-State Nanopores. *Nano Lett.* **2009**, *9* (8), 2953–2960. https://doi.org/10.1021/nl901370w.
(57) Kowalczyk, S. W.; Tuijtel, M. W.; Donkers, S. P.; Dekker, C. Unraveling Single-Stranded DNA in a Solid-State Nanopore. *Nano letters* **2010**, *10* (4), 1414–1420.
(58) Bell, N. A. W.; Keyser, U. F. Specific Protein Detection Using Designed DNA Carriers and Nanopores. *J. Am. Chem. Soc.* **2015**, *137* (5), 2035–2041. https://doi.org/10.1021/ja512521w.
(59) Bell, N. A. W.; Keyser, U. F. Digitally Encoded DNA Nanostructures for Multiplexed, Single-Molecule Protein Sensing with Nanopores. *Nature Nanotechnology* **2016**, *11* (7), 645–651. https://doi.org/10.1038/nnano.2016.50.
(60) Rothemund, P. W. K. Folding DNA to Create Nanoscale Shapes and Patterns. *Nature* **2006**, *440* (7082), 297. https://doi.org/10.1038/nature04586.
(61) Kong, J.; Bell, N. A. W.; Keyser, U. F. Quantifying Nanomolar Protein Concentrations Using Designed DNA Carriers and Solid-State Nanopores. *Nano Lett.* **2016**, *16* (6), 3557–3562. https://doi.org/10.1021/acs.nanolett.6b00627.
(62) Kong, J.; Zhu, J.; F. Keyser, U. Single Molecule Based SNP Detection Using Designed DNA Carriers and Solid-State Nanopores. *Chemical Communications* **2017**, *53* (2), 436–439. https://doi.org/10.1039/C6CC08621G.
(63) Chen, K.; Juhasz, M.; Gularek, F.; Weinhold, E.; Tian, Y.; Keyser, U. F.; Bell, N. A. W. Ionic Current-Based Mapping of Short Sequence Motifs in Single DNA Molecules Using Solid-State Nanopores. *Nano Lett.* **2017**, *17* (9), 5199–5205. https://doi.org/10.1021/acs.nanolett.7b01009.
(64) Sze, J. Y. Y.; Ivanov, A. P.; Cass, A. E. G.; Edel, J. B. Single Molecule Multiplexed Nanopore Protein Screening in Human Serum Using Aptamer Modified DNA Carriers. *Nature Communications* **2017**, *8* (1), 1552. https://doi.org/10.1038/s41467-017-01584-3.
(65) Chandrasekaran, A. R.; Anderson, N.; Kizer, M.; Halvorsen, K.; Wang, X. Beyond the Fold: Emerging Biological Applications of DNA Origami. *ChemBioChem* **2016**, *17* (12), 1081–1089. https://doi.org/10.1002/cbic.201600038.
(66) Liu, J.; Geng, Y.; Pound, E.; Gyawali, S.; Ashton, J. R.; Hickey, J.; Woolley, A. T.; Harb, J. N. Metallization of Branched DNA Origami for Nanoelectronic Circuit Fabrication. *ACS Nano* **2011**, *5* (3), 2240–2247. https://doi.org/10.1021/nn1035075.
(67) Douglas, S. M.; Bachelet, I.; Church, G. M. A Logic-Gated Nanorobot for Targeted Transport of Molecular Payloads. *Science* **2012**, *335* (6070), 831–834. https://doi.org/10.1126/science.1214081.
(68) Allentoft, M. E.; Collins, M.; Harker, D.; Haile, J.; Oskam, C. L.; Hale, M. L.; Campos, P. F.; Samaniego, J. A.; Gilbert, M. T. P.; Willerslev, E.; et al. The Half-Life of DNA in Bone: Measuring Decay Kinetics in 158 Dated Fossils.

Proc. Biol. Sci. **2012**, *279* (1748), 4724–4733. https://doi.org/10.1098/rspb.2012.1745.
(69) Bornholt, J.; Lopez, R.; Carmean, D.; Ceze, L.; Seelig, G.; Strauss, K. A DNA-Based Archival Storage System. *Proceedings of the Twenty-First International Conference on Architectural Support for Programming Languages and Operating Systems* **2016**, 637–649.
(70) Chandrasekaran, A. R.; Levchenko, O.; Patel, D. S.; MacIsaac, M.; Halvorsen, K. Addressable Configurations of DNA Nanostructures for Rewritable Memory. *Nucleic Acids Res.* **2017**, *45* (19), 11459–11465. https://doi.org/10.1093/nar/gkx777.
(71) Halvorsen, K.; Wong, W. P. Binary DNA Nanostructures for Data Encryption. *PLOS ONE* **2012**, *7* (9), e44212. https://doi.org/10.1371/journal.pone.0044212.
(72) Koussa, M. A.; Halvorsen, K.; Ward, A.; Wong, W. P. DNA Nanoswitches: A Quantitative Platform for Gel-Based Biomolecular Interaction Analysis. *Nature Methods* **2015**, *12* (2), 123–126. https://doi.org/10.1038/nmeth.3209.
(73) Chandrasekaran, A. R.; MacIsaac, M.; Dey, P.; Levchenko, O.; Zhou, L.; Andres, M.; Dey, B. K.; Halvorsen, K. Detection of Cellular MicroRNAs with Programmable DNA Nanoswitches. *bioRxiv* **2018**, 334631. https://doi.org/10.1101/334631.
(74) Chandrasekaran, A. R. DNA Nanobiosensors: An Outlook on Signal Readout Strategies https://www.hindawi.com/journals/jnm/2017/2820619/abs/ (accessed Mar 26, 2019). https://doi.org/10.1155/2017/2820619.
(75) Chandrasekaran, A. R.; Zavala, J.; Halvorsen, K. Programmable DNA Nanoswitches for Detection of Nucleic Acid Sequences. *ACS Sens.* **2016**, *1* (2), 120–123. https://doi.org/10.1021/acssensors.5b00178.
(76) Plesa, C.; van Loo, N.; Ketterer, P.; Dietz, H.; Dekker, C. Velocity of DNA during Translocation through a Solid-State Nanopore. *Nano Lett.* **2015**, *15* (1), 732–737. https://doi.org/10.1021/nl504375c.
(77) Jain, M.; Olsen, H. E.; Paten, B.; Akeson, M. The Oxford Nanopore MinION: Delivery of Nanopore Sequencing to the Genomics Community. *Genome Biology* **2016**, *17* (1), 239. https://doi.org/10.1186/s13059-016-1103-0.
(78) Tahvildari, R.; Beamish, E.; Tabard-Cossa, V.; Godin, M. Integrating Nanopore Sensors within Microfluidic Channel Arrays Using Controlled Breakdown. *Lab Chip* **2015**, *15* (6), 1407–1411. https://doi.org/10.1039/C4LC01366B.
(79) Restrepo-Pérez, L.; Joo, C.; Dekker, C. Paving the Way to Single-Molecule Protein Sequencing. *Nature Nanotechnology* **2018**, *13* (9), 786. https://doi.org/10.1038/s41565-018-0236-6.
(80) Xu, M.-Y.; Liu, S.-Q.; Deng, C.-L.; Zhang, Q.-Y.; Zhang, B. Detection of Zika Virus by SYBR Green One-Step Real-Time RT-PCR. *Journal of Virological Methods* **2016**, *236*, 93–97. https://doi.org/10.1016/j.jviromet.2016.07.014.
(81) Beamish, E.; Tabard-Cossa, V.; Godin, M. Identifying Structure in Short DNA Scaffolds Using Solid-State Nanopores. *ACS Sens.* **2017**, *2* (12), 1814–1820. https://doi.org/10.1021/acssensors.7b00628.
(82) Karau, P.; Tabard-Cossa, V. Capture and Translocation Characteristics of Short Branched DNA Labels in Solid-State Nanopores. *ACS Sens.* **2018**, *3* (7), 1308–1315. https://doi.org/10.1021/acssensors.8b00165.

(83) Morin, T. J.; Shropshire, T.; Liu, X.; Briggs, K.; Huynh, C.; Tabard-Cossa, V.; Wang, H.; Dunbar, W. B. Nanopore-Based Target Sequence Detection. *PLOS ONE* **2016**, *11* (5), e0154426. https://doi.org/10.1371/journal.pone.0154426.
(84) He, Y.; Tsutsui, M.; Fan, C.; Taniguchi, M.; Kawai, T. Gate Manipulation of DNA Capture into Nanopores. *ACS Nano* **2011**, *5* (10), 8391–8397. https://doi.org/10.1021/nn203186c.
(85) Sohi, A. N.; Beamish, E.; Tabard-Cossa, V.; Godin, M. Effect of Flow on Nanopore Sensor Performance When Confined in a Microchannel. *Small* **2019**, Submitted.
(86) Mitov, M. I.; Greaser, M. L.; Campbell, K. S. GelBandFitter – A Computer Program for Analysis of Closely Spaced Electrophoretic and Immunoblotted Bands. *Electrophoresis* **2009**, *30* (5), 848–851. https://doi.org/10.1002/elps.200800583.
(87) Raillon, C.; Granjon, P.; Graf, M.; J. Steinbock, L.; Radenovic, A. Fast and Automatic Processing of Multi-Level Events in Nanopore Translocation Experiments. *Nanoscale* **2012**, *4* (16), 4916–4924. https://doi.org/10.1039/C2NR30951C.
(88) Forstater, J. H.; Briggs, K.; Robertson, J. W. F.; Ettedgui, J.; Marie-Rose, O.; Vaz, C.; Kasianowicz, J. J.; Tabard-Cossa, V.; Balijepalli, A. MOSAIC: A Modular Single-Molecule Analysis Interface for Decoding Multistate Nanopore Data. *Anal. Chem.* **2016**, *88* (23), 11900–11907. https://doi.org/10.1021/acs.analchem.6b03725.
(89) Briggs, K. CUSUM: Release for DOI Generation by Zenodo. *Zenodo*. https://doi.org/10.5281/zenodo.58763.
(90) Plesa, C.; Verschueren, D.; Pud, S.; van der Torre, J.; Ruitenberg, J. W.; Witteveen, M. J.; Jonsson, M. P.; Grosberg, A. Y.; Rabin, Y.; Dekker, C. Direct Observation of DNA Knots Using a Solid-State Nanopore. *Nat Nano* **2016**, *11* (12), 1093–1097. https://doi.org/10.1038/nnano.2016.153.
(91) Wanunu, M.; Cohen-Karni, D.; Johnson, R. R.; Fields, L.; Benner, J.; Peterman, N.; Zheng, Y.; Klein, M. L.; Drndic, M. Discrimination of Methylcytosine from Hydroxymethylcytosine in DNA Molecules. *Journal of the American Chemical Society* **2011**, *133* (3), 486–492. https://doi.org/10.1021/ja107836t.
(92) Carson, S.; Wick, S. T.; Carr, P. A.; Wanunu, M.; Aguilar, C. A. Direct Analysis of Gene Synthesis Reactions Using Solid-State Nanopores. *ACS Nano* **2015**, *9* (12), 12417–12424. https://doi.org/10.1021/acsnano.5b05782.
(93) Plesa, C.; Ruitenberg, J. W.; Witteveen, M. J.; Dekker, C. Detection of Individual Proteins Bound along DNA Using Solid-State Nanopores. *Nano Lett.* **2015**, *15* (5), 3153–3158. https://doi.org/10.1021/acs.nanolett.5b00249.
(94) Tahvildari, R.; Beamish, E.; Tabard-Cossa, V.; Godin, M. Integrating Nanopore Sensors within Microfluidic Channel Arrays Using Controlled Breakdown. *Lab Chip* **2015**, *15* (6), 1407–1411. https://doi.org/10.1039/C4LC01366B.
(95) Tahvildari, R.; Beamish, E.; Briggs, K.; Chagnon-Lessard, S.; Sohi, A. N.; Han, S.; Watts, B.; Tabard-Cossa, V.; Godin, M. Manipulating Electrical and Fluidic Access in Integrated Nanopore-Microfluidic Arrays Using Microvalves. *Small* **2017**, *13* (10). https://doi.org/10.1002/smll.201602601.

(96) Zahid, O. K.; Wang, F.; Ruzicka, J. A.; Taylor, E. W.; Hall, A. R. Sequence-Specific Recognition of MicroRNAs and Other Short Nucleic Acids with Solid-State Nanopores. *Nano Lett.* **2016**, *16* (3), 2033–2039. https://doi.org/10.1021/acs.nanolett.6b00001.
(97) Singer, A.; Wanunu, M.; Morrison, W.; Kuhn, H.; Frank-Kamenetskii, M.; Meller, A. Nanopore Based Sequence Specific Detection of Duplex DNA for Genomic Profiling. *Nano Lett.* **2010**, *10* (2), 738–742. https://doi.org/10.1021/nl100058y.
(98) Bell, N. A. W.; Keyser, U. F. Digitally Encoded DNA Nanostructures for Multiplexed, Single-Molecule Protein Sensing with Nanopores. *Nat Nano* **2016**, *11* (7), 645–651. https://doi.org/10.1038/nnano.2016.50.
(99) Bell, N. A. W.; Keyser, U. F. Specific Protein Detection Using Designed DNA Carriers and Nanopores. *J. Am. Chem. Soc.* **2015**, *137* (5), 2035–2041. https://doi.org/10.1021/ja512521w.
(100) Kong, J.; Zhu, J.; Keyser, U. F. Single Molecule Based SNP Detection Using Designed DNA Carriers and Solid-State Nanopores. *Chem. Commun.* **2016**. https://doi.org/10.1039/C6CC08621G.
(101) Carson, S.; Wilson, J.; Aksimentiev, A.; Wanunu, M. Smooth DNA Transport through a Narrowed Pore Geometry. *Biophysical Journal* **2014**, *107* (10), 2381–2393. https://doi.org/10.1016/j.bpj.2014.10.017.
(102) Arnaut, V.; Langecker, M.; Simmel, F. C. Nanopore Force Spectroscopy of Aptamer-Ligand Complexes. *Biophys. J.* **2013**, *105* (5), 1199–1207. https://doi.org/10.1016/j.bpj.2013.07.047.
(103) Ding, S.; Gao, C.; Gu, L.-Q. Capturing Single Molecules of Immunoglobulin and Ricin with an Aptamer-Encoded Glass Nanopore. *Anal. Chem.* **2009**, *81* (16), 6649–6655. https://doi.org/10.1021/ac9006705.
(104) Zhu, J.; Zhang, L.; Zhou, Z.; Dong, S.; Wang, E. Molecular Aptamer Beacon Tuned DNA Strand Displacement to Transform Small Molecules into DNA Logic Outputs. *Chem. Commun.* **2014**, *50* (25), 3321–3323. https://doi.org/10.1039/C3CC49833F.
(105) Deng, D.; Xia, N.; Li, S.; Xu, C.; Sun, T.; Pang, H.; Liu, L. Simple, Fast and Selective Detection of Adenosine Triphosphate at Physiological PH Using Unmodified Gold Nanoparticles as Colorimetric Probes and Metal Ions as Cross-Linkers. *Sensors (Basel)* **2012**, *12* (11), 15078–15087. https://doi.org/10.3390/s121115078.
(106) Shekar, S.; Niedzwiecki, D. J.; Chien, C.-C.; Ong, P.; Fleischer, D. A.; Lin, J.; Rosenstein, J. K.; Drndić, M.; Shepard, K. L. Measurement of DNA Translocation Dynamics in a Solid-State Nanopore at 100 Ns Temporal Resolution. *Nano Lett.* **2016**, *16* (7), 4483–4489. https://doi.org/10.1021/acs.nanolett.6b01661.
(107) Balan, A.; Chien, C.-C.; Engelke, R.; Drndić, M. Suspended Solid-State Membranes on Glass Chips with Sub 1-PF Capacitance for Biomolecule Sensing Applications. *Scientific Reports* **2015**, *5*, 17775. https://doi.org/10.1038/srep17775.
(108) *Cumulative Sum Charts and Charting for Quality Improvement | Douglas M. Hawkins | Springer*.

(109) Dong, H.; Lei, J.; Ding, L.; Wen, Y.; Ju, H.; Zhang, X. MicroRNA: Function, Detection, and Bioanalysis. *Chem. Rev.* **2013**, *113* (8), 6207–6233. https://doi.org/10.1021/cr300362f.
(110) Ouyang, T.; Liu, Z.; Han, Z.; Ge, Q. MicroRNA Detection Specificity: Recent Advances and Future Perspective. *Anal. Chem.* **2019**, *91* (5), 3179–3186. https://doi.org/10.1021/acs.analchem.8b05909.
(111) Venkatesan, B. M.; Bashir, R. Nanopore Sensors for Nucleic Acid Analysis. *Nature Nanotechnology* **2011**, *6* (10), 615–624. https://doi.org/10.1038/nnano.2011.129.
(112) Miles, B. N.; Ivanov, A. P.; Wilson, K. A.; Doğan, F.; Japrung, D.; Edel, J. B. Single Molecule Sensing with Solid-State Nanopores: Novel Materials, Methods, and Applications. *Chem. Soc. Rev.* **2012**, *42* (1), 15–28. https://doi.org/10.1039/C2CS35286A.
(113) Sze, J. Y. Y.; Ivanov, A. P.; Cass, A. E. G.; Edel, J. B. Single Molecule Multiplexed Nanopore Protein Screening in Human Serum Using Aptamer Modified DNA Carriers. *Nature Communications* **2017**, *8* (1), 1552. https://doi.org/10.1038/s41467-017-01584-3.
(114) Wanunu, M.; Dadosh, T.; Ray, V.; Jin, J.; McReynolds, L.; Drndić, M. Rapid Electronic Detection of Probe-Specific MicroRNAs Using Thin Nanopore Sensors. *Nat Nano* **2010**, *5* (11), 807–814. https://doi.org/10.1038/nnano.2010.202.
(115) Morin, T. J.; McKenna, W. L.; Shropshire, T. D.; Wride, D. A.; Deschamps, J. D.; Liu, X.; Stamm, R.; Wang, H.; Dunbar, W. B. A Handheld Platform for Target Protein Detection and Quantification Using Disposable Nanopore Strips. *Scientific Reports* **2018**, *8* (1), 14834. https://doi.org/10.1038/s41598-018-33086-7.
(116) Garzon, R.; Calin, G. A.; Croce, C. M. MicroRNAs in Cancer. *Annual Review of Medicine* **2009**, *60* (1), 167–179. https://doi.org/10.1146/annurev.med.59.053006.104707.
(117) Poliseno, L.; Salmena, L.; Zhang, J.; Carver, B.; Haveman, W. J.; Pandolfi, P. P. A Coding-Independent Function of Gene and Pseudogene MRNAs Regulates Tumour Biology. *Nature* **2010**, *465* (7301), 1033–1038. https://doi.org/10.1038/nature09144.
(118) Lu, J.; Getz, G.; Miska, E. A.; Alvarez-Saavedra, E.; Lamb, J.; Peck, D.; Sweet-Cordero, A.; Ebert, B. L.; Mak, R. H.; Ferrando, A. A.; et al. MicroRNA Expression Profiles Classify Human Cancers. *Nature* **2005**, *435* (7043), 834–838. https://doi.org/10.1038/nature03702.
(119) Wang, Y.; Zheng, D.; Tan, Q.; Wang, M.; Gu, L.-Q. Nanopore-Based Detection of Circulating MicroRNAs in Lung Cancer Patients. *Nat Nanotechnol* **2011**, *6* (10), 668–674. https://doi.org/10.1038/nnano.2011.147.
(120) Zhang, X.; Liu, C.; Sun, L.; Duan, X.; Li, Z. Lab on a Single Microbead: An Ultrasensitive Detection Strategy Enabling MicroRNA Analysis at the Single-Molecule Level. *Chem. Sci.* **2015**, *6* (11), 6213–6218. https://doi.org/10.1039/C5SC02641E.

(121) Koo, B.; Yorita, A. M.; Schmidt, J. J.; Monbouquette, H. G. Amplification-Free, Sequence-Specific 16S RRNA Detection at 1 AM. *Lab Chip* **2018**, *18* (15), 2291–2299. https://doi.org/10.1039/C8LC00452H.
(122) He, L.; Karau, P.; Tabard-Cossa, V. Fast Capture and Multiplexed Detection of Short Multi-Arm DNA Stars in Solid-State Nanopores. *Nanoscale* **2019**. https://doi.org/10.1039/C9NR04566J.
(123) Karau, P. DNA Labels for Improved Detection and Capture with Solid-State Nanopores. Thesis, Université d'Ottawa / University of Ottawa, 2018. http://dx.doi.org/10.20381/ruor-21970.
(124) Misiunas, K.; Ermann, N.; Keyser, U. F. QuipuNet: Convolutional Neural Network for Single-Molecule Nanopore Sensing. *Nano Letters* **2018**, *18* (6), 4040–4045. https://doi.org/10.1021/acs.nanolett.8b01709.
(125) Liu, S.; Yuzvinsky, T. D.; Schmidt, H. Effect of Fabrication-Dependent Shape and Composition of Solid-State Nanopores on Single Nanoparticle Detection. *ACS Nano* **2013**, *7* (6), 5621–5627. https://doi.org/10.1021/nn4020642.
(126) Charron, M.; Briggs, K.; King, S.; Waugh, M.; Tabard-Cossa, V. Precise DNA Concentration Measurements with Nanopores by Controlled Counting. *Analytical Chemistry* **2019**, Accepted.
(127) Oligo Analyzer https://www.idtdna.com/calc/analyzer (accessed Jun 10, 2019).
(128) Rabinowits, G.; Gerçel-Taylor, C.; Day, J. M.; Taylor, D. D.; Kloecker, G. H. Exosomal MicroRNA: A Diagnostic Marker for Lung Cancer. *Clin Lung Cancer* **2009**, *10* (1), 42–46. https://doi.org/10.3816/CLC.2009.n.006.
(129) Chandrasekaran, A. R.; Halvorsen, K. Controlled Disassembly of a DNA Tetrahedron Using Strand Displacement. *Nanoscale Adv.* **2019**, *1* (3), 969–972. https://doi.org/10.1039/C8NA00340H.
(130) Chandrasekaran, A. R.; MacIsaac, M.; Dey, P.; Levchenko, O.; Zhou, L.; Andres, M.; Dey, B. K.; Halvorsen, K. Cellular MicroRNA Detection with MiRacles: MicroRNA- Activated Conditional Looping of Engineered Switches. *Science Advances* **2019**, *5* (3), eaau9443. https://doi.org/10.1126/sciadv.aau9443.
(131) Alibakhshi, M. A.; Halman, J. R.; Wilson, J.; Aksimentiev, A.; Afonin, K. A.; Wanunu, M. Picomolar Fingerprinting of Nucleic Acid Nanoparticles Using Solid-State Nanopores. *ACS Nano* **2017**, *11* (10), 9701–9710. https://doi.org/10.1021/acsnano.7b04923.
(132) Tabard-Cossa, V.; Trivedi, D.; Wiggin, M.; Jetha, N. N.; Marziali, A. Noise Analysis and Reduction in Solid-State Nanopores. *Nanotechnology* **2007**, *18* (30), 305505. https://doi.org/10.1088/0957-4484/18/30/305505.
(133) Waugh, M.; Briggs, K.; Gunn, D.; Gibeault, M.; King, S.; Ingram, Q.; Jimenez, A. M.; Berryman, S.; Lomovtsev, D.; Andrzejewski, L.; et al. Solid-State Nanopore Fabrication by Automated Controlled Breakdown. *Nature Protocols* **2019**, Under Review.
(134) Lilley, D. M. J. Analysis of Branched Nucleic Acid Structure Using Comparative Gel Electrophoresis. *Quarterly Reviews of Biophysics* **2008**, *41* (1), 1–39. https://doi.org/10.1017/S0033583508004678.

(135) van den Hout, M.; Hall, A. R.; Wu, M. Y.; Zandbergen, H. W.; Dekker, C.; Dekker, N. H. Controlling Nanopore Size, Shape and Stability. *Nanotechnology* **2010**, *21*, 115304.
(136) Briggs, K. Solid-State Nanopores: Fabrication, Application, and Analysis. Thesis, Université d'Ottawa / University of Ottawa, 2018. http://dx.doi.org/10.20381/ruor-22794.
(137) Arcadia, C. E.; Reyes, C. C.; Rosenstein, J. K. In Situ Nanopore Fabrication and Single-Molecule Sensing with Microscale Liquid Contacts. *ACS Nano* **2017**, *11* (5), 4907–4915. https://doi.org/10.1021/acsnano.7b01519.
(138) Varongchayakul, N.; Hersey, J. S.; Squires, A.; Meller, A.; Grinstaff, M. W. A Solid-State Hard Microfluidic–Nanopore Biosensor with Multilayer Fluidics and On-Chip Bioassay/Purification Chamber. *Advanced Functional Materials* **2018**, *28* (50), 1804182. https://doi.org/10.1002/adfm.201804182.
(139) Tabard-Cossa, V.; Godin, M.; TAHVILDARI, R.; Beamish, E. Integrating Nanopore Sensors within Microfluidic Channel Arrays Using Controlled Breakdown. US20170363609A1, December 21, 2017.
(140) Yusko, E. C.; Bruhn, B. R.; Eggenberger, O. M.; Houghtaling, J.; Rollings, R. C.; Walsh, N. C.; Nandivada, S.; Pindrus, M.; Hall, A. R.; Sept, D.; et al. Real-Time Shape Approximation and Fingerprinting of Single Proteins Using a Nanopore. *Nat Nano* **2016**, *advance online publication*. https://doi.org/10.1038/nnano.2016.267.
(141) Chen, K.; Keyser, U. F. The Nanopore Site https://www.thenanoporesite.com/ (accessed Jun 7, 2019).